ARCHIVES OF ACOUSTICS
**25**, 2, 131–145 (2000)

# BINAURAL PERCEPTION OF AMPLITUDE AND FREQUENCY MODULATED SIGNALS

E. OZIMEK, A. WICHER

Institute of Acoustics,
Adam Mickiewicz University
(61-614 Poznań, Umultowska 85, Poland)

The investigations focused on the binaural perception of amplitude modulated (AM) and frequency modulated (FM) signals. They are comprised of two experiments. In the first experiment binaurally perceived (matched) modulation depth for AM signals was determined under diotic conditions (i.e. for the same values of modulation depth coefficient, $m$, presented to the left ($m_l$) and right ($m_r$) ears) and under dichotic conditions (i.e. for different values of these coefficients $m_l \neq m_r$). The measurements were made for the interaural differences in modulation depth coefficient $\Delta m$, changing from 0 to 100% and a few selected modulating frequencies (4, 64 and 128 Hz) and carrier frequencies (250 and 1000 Hz). In the second experiment binaurally perceived (matched) frequency deviation of FM signals was determined under diotic conditions (i.e. for the same values of frequency deviation, $\Delta f$, presented to the left ($\Delta f_l$) and right ($\Delta f_r$) ear ($\Delta f_l = \Delta f_r$) and under dichotic conditions (i.e. for different values of this deviation ($\Delta f_l \neq \Delta f_r$)). The measurements were made for the interaural differences of frequency deviation changing from 0 to 20 Hz; a few selected modulating frequencies (32, 64 and 128 Hz) and carrier frequencies (500 and 1000 Hz). It was found in Experiment I that for small interaural differences in modulation depth, $\Delta m$, the binaurally perceived modulation depth, $m$, is equal to the arithmetic mean of the depths presented to the left and right ears, whereas for large values of $\Delta m$, the value of $m$ is smaller than the mean. The results of Experiment II revealed that the binaurally perceived frequency deviation is a linear function of interaural differences of this deviation and is equal to the arithmetic mean of deviations presented to the left and right ears.

## 1. Introduction

Binaural hearing is a complex process of sound perception during which an interaction of signals received by each ear takes place. Binaural perception is related to such effects as: directivity and sound localization, lateralization and fusion of sound images, binaural masking level differences, etc. The results of binaural perception are often compared to the results of monaural perception. For example, comparison of binaural and monaural detection thresholds for tones revealed that the binaural detection thresholds are on average 3 dB lower than monaural detection thresholds (Keys [12]; Shaw *et al.* [27]). This result suggests a summation of signals from both ears in the binaural perception process.

However, results of investigations conducted by others (Pollack [23]) did not univocally confirm this summation mechanism. Comparison of results of investigations of loudness evaluated binaurally and monaurally also indicates the mechanism of nearly perfect binaural summation of loudness (Hellman and Zwislocki [7]; Marks [14]). However, the mechanism of such summation was questioned by the results of experiments conducted by others (Reynolds and Stevens [24]; Scharf and Fishken [26]) indicating that it is not fully univocal.

Investigations of difference thresholds of intensity and frequency also revealed that the thresholds are lower for binaural perception compared with monaural perception (Rowland and Tobias [25]; Jesteadt *et al.* [11]). According to Jesteadt [11], in frequency range of 250 – 4000 Hz, the ratio of the monaural to the binaural intensity difference thresholds is of the order of 1.65, whereas for the frequency difference thresholds it is equal to about 1.44.

Binaural perception is exceptionally complex in the case of signals with parameters varying in time, e.g. amplitude modulated (AM) signals and frequency modulated (FM) signals. Binaural investigations into AM signals conducted so far focused on the problems of localization, lateralization, binaural masking level differences and modulation detection interference (Nuetzel and Hafter [17, 18]; McFadden and Pasanen [15]; Henning [8]; Henning and Ashton [9]; Bernstein and Trahiotis [1, 2]; Mendoza *et al.* [16]; Heller and Trahiotis [6]). On the other hand, binaural perception of FM signals is usually connected with different beat effects. The binaural beats occur when a certain frequency tone is heard by one ear whereas the other ear hears another tone with slightly different frequency. The perceived sound fluctuates with a frequency equal to the difference of the frequencies of the two tones (Licklider *et al.* [13]; Perrott and Nelson [21]). The binaural beat effect is most clearly heard in a narrow frequency range, i.e. about 250 – 500 Hz; the range depends on the acoustic pressure level of the tones. The specific character of binaural beats is fairly complex in perception because in addition to beats the so-called rotating tones are sometimes distinguished or the beats are connected with the shifting of the sound image (Perrott and Musicant [22]). Tobias [30] found out binaural beats in case of large interaural differences in acoustic pressure level occurring between tones. According to Groen [4], binaural beats can also occur when the acoustic pressure level of one tone is below the hearing threshold. However, results of the latter investigations indicate that binaural beats are perceived when the pressure level of tone corresponds to the value higher than 0 dB SL (Gu *et al.* [5]). Binaural beats are a proof that in the auditory system there is an interaction between neural discharges from the left and right ears. Furthermore, the structure of these discharges must contain information about instantaneous signal phase as this conditions the generation of subjective loudness fluctuations.

It is interesting from the cognitive point of view to investigate the sensation of modulation in the case of binaural perception of amplitude or frequency modulated signals. The investigations are connected with a number of different problems, which have not been solved to date. One of them is determination of the value of binaurally perceived depth of amplitude modulation when the depths, expressed by $m_l$ and $m_r$, are different in the left and right ears. It is also interesting to determine the relation of the perceived modulation depth to the modulating and carrier frequency of AM signal. Similar problems are encountered in the case of binaural perception of FM signals. In the latter case it is also important to investigate the value of binaurally perceived frequency deviation depending on interaural deviation differences and the modulating and carrier frequency.

The above problem has so far been discussed in literature to a limited extent only. Preliminary results of investigations into the binaural perception of AM and FM signals are reported in Ozimek *et al.* [19]; Wicher and Ozimek [31]. The investigations reported in this paper are a continuation of the investigations mentioned above. They comprise two experiments. The aim of the first experiment was to determine the resultant depth of amplitude modulation perceived by the subject for AM signals presented binaurally, depending on the interaural differences of this depth, for a few modulating and carrier frequencies. The second experiment comprised binaural perception of frequency modulated signals to determine the resultant value of frequency deviation for FM signals depending on the interaural differences of this deviation, for a few selected modulating and carrier frequencies. It should be pointed out that in addition to the cognitive character of the investigations, their results could have some practical significance, mainly as regards binaural perception of real sounds (speech and music), in different hearing conditions, particularly binaural perception of these sounds in different rooms in which large changes in the amplitude and frequency structure are often observed (Ozimek and Sęk [20]); the latter have a significant effect on the intelligibility of speech and perception of music, which are related to the acoustic quality of rooms.

## 2. Experimental set up, signals and methodology

Sinusoidal signals were used in the investigations. In Experiment I they were amplitude modulated and in Experiment II — frequency modulated by a periodic modulating signal. The signals were digitally generated at the sampling rate of 50 kHz and then low-pass filtered at 10 kHz (Tucker-Davis Technology, TDK). The equipment and experiments were computer controlled. Each signal lasted 1000 ms, including the growth and decay times of 20 ms each. The signals were presented to the subjects in pairs (trials), both in Experiment I and Experiment II. Each pair included a standard signal (standard) characterized by equal values of modulation depth in Experiment I or frequency deviation in Experiment II at both ears and the test signal (test) with equal (in the case of diotic conditions) or different (in the case of dichotic conditions) modulation depth or frequency deviations. The set up of Experiments I and II is illustrated in Fig. 1.

The standard and test in the trial were separated by a 500 ms interval and presented in random order. A set of 40 trials constituted one run. The stimuli were presented to the subjects binaurally through HDA200 phones. Measurements for AM signals were made for carrier frequencies of $f_c = 250$ and 1000 Hz and modulating frequencies of $f_m = 4$, 64 and 128 Hz and for changes in the interaural difference of modulation depth ranging from 0 to 100%. Measurements for FM signals were made for carrier frequencies of $f_c = 500$ and 1000 Hz and modulating frequencies of $f_m = 4$, 32, 64 and 128 Hz and changes in

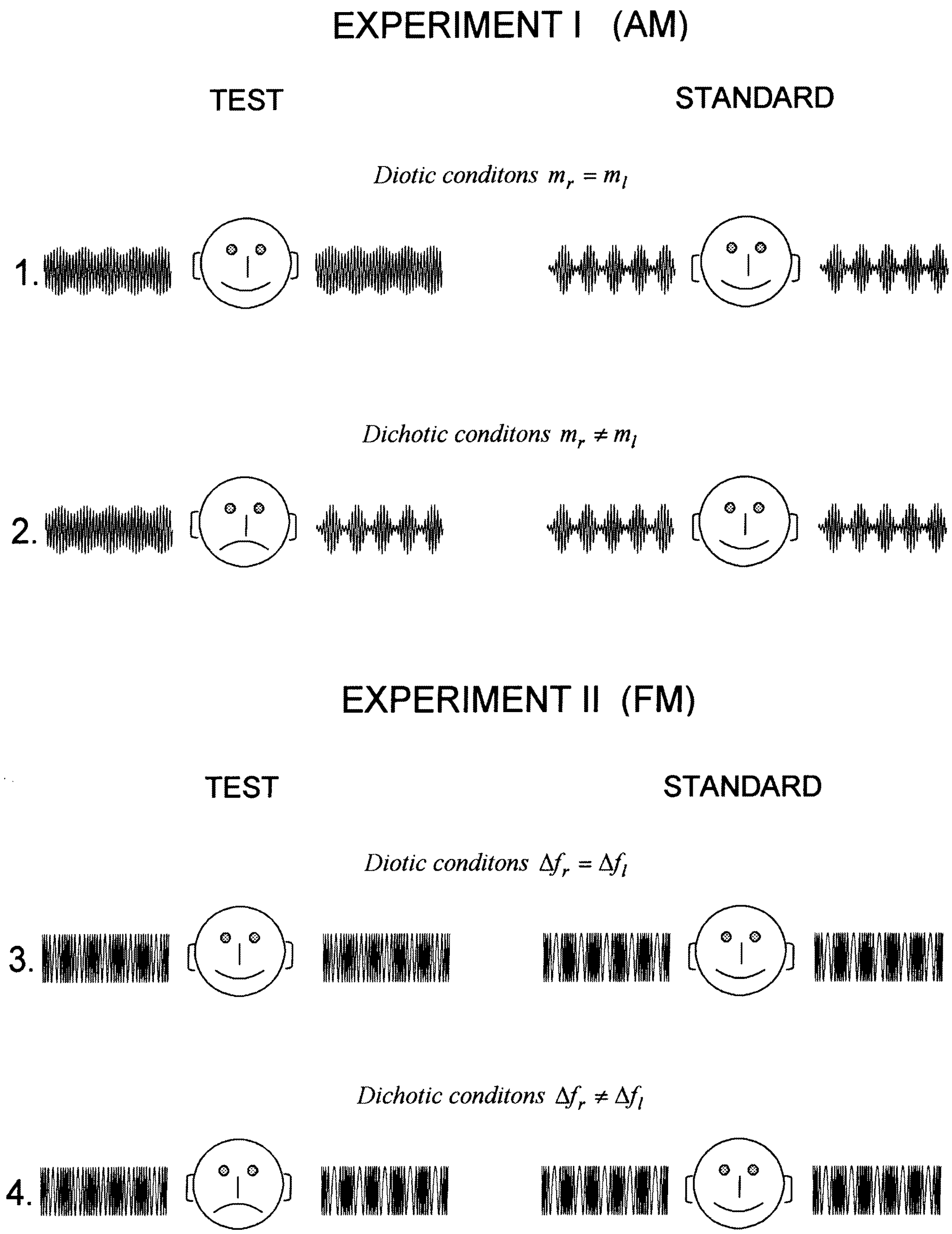


Fig. 1. The set up of Experiments I and II under diotic (1 and 3) and dichotic (2 and 4) conditions.

the interaural difference of frequency deviation ranging from 0 to 20 Hz. The upper limit of the deviation changes was selected so as to achieve the fusion effect of the FM sound image. The acoustic pressure level for all the signals was equal to 70 dB SPL.

Stimuli were presented according to the two alternative forced choice paradigm (2AFC) with the one-up, two-down adaptive procedure. Trials started with the modulation depth (in Experiment I) or frequency deviation (in Experiment II) of the standard well above the anticipated binaurally perceived modulation of the test signal. The subject's task was to match the modulation depth of the standard to that of the test in Experiment I, or the frequency deviation of the standard to that of the test in Experiment II. The modulation depth, or frequency deviation of the standard was tracked during the run by 1 dB until four turnpoints were reached and then by 0.5 dB for the rest of the run. In this way the difference in modulation depth or frequency deviation between the standard and the test was gradually decreased. In this way it was possible to obtain the point of subjective equality between sensations of the modulation depth or frequency deviation for the standard and test signals. Besides the perception of modulation depth or changes in the frequency deviation some lateralization effects also occurred in the experiments. The subjects were instructed to disregard these disturbing effects and focus their attention only on the evaluation of changes in the modulation depth or frequency deviation.

It should be stressed that Experiments I and II could only be conducted for those parameters for which the so-called binaural fusion of the sound images takes place. Lack of this fusion that occurred, for instance, for large frequency deviations of FM signals was manifested by the separation of the sound image in the head, which made binaural perception impossible.

Binaurally perceived modulation depths or frequency deviations were calculated as an arithmetic mean of the last 8 turnpoints. Their final values were counted as an average of at least five single estimates (taken from 5 runs). Three subjects with normal hearing, for whom interaural differences of audibility thresholds did not exceed 6 dB, participated in Experiments I and II.

## 3. Experiment I. Binaural perception of AM signals

At the initial stage of Experiment I we defined the binaural modulation depth of AM sounds under conditions of diotic presentation (cf. Fig. 1.1), i.e. when the modulation depth at the left and right ears were the same. This initial stage aimed at defining the subjects' ability to evaluate the binaurally perceived modulation depth within the range of parameters measured. Figure 2 shows the dependence of the binaurally perceived (matched) modulation depth ($m$), averaged for 3 subjects and expressed in percentages, on the presented modulation depth, at $m_l = m_r$. The frequency of carrier signals equalled 250 and 1000 Hz. The modulating frequency was the parameter of the data.

As can be seen in Fig. 2, the experimental data are distributed along a nearly straight line ($y = x$), presenting the ideal matching of the perceived and presented modulation depths. The straight line expresses an arithmetic mean of the values of modulation depths presented to both ears, i.e. $m = (m_l + m_r)/2$ [19]. As for diotic presentation $m_l = m_r$, hence $m = m_l = m_r$. It also follows from Fig. 2 that the perceived modulation depth is neither the function of carrier frequency nor modulating frequency.

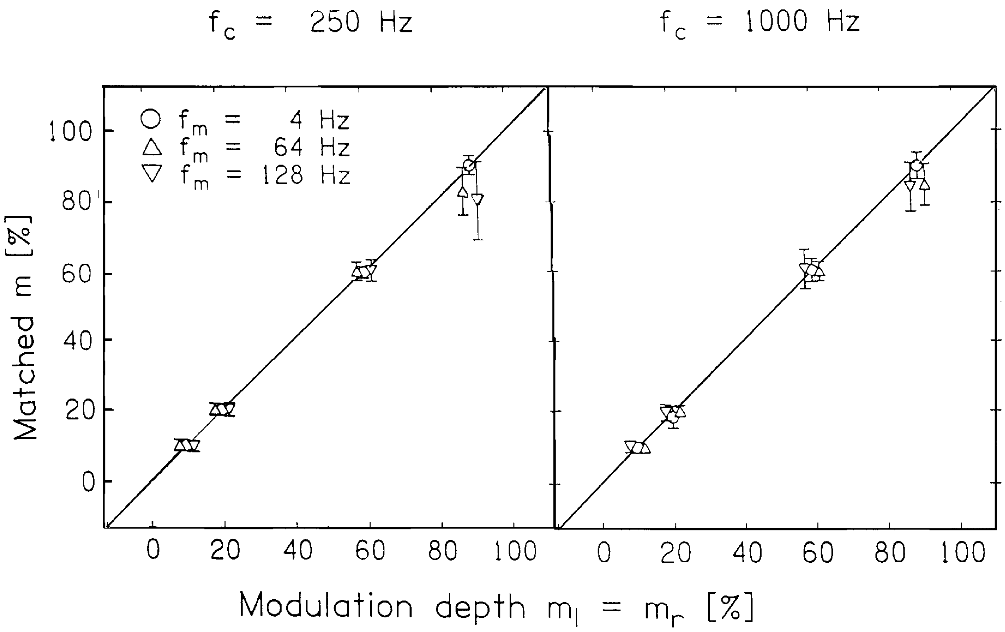


Fig. 2. Dependence of the binaurally matched modulation depth ($m$) on the modulation depth presented to the left ($m_l$) and right ($m_r$) ears, under diotic conditions of perception ($m_l = m_r$). The frequency of carrier signals equalled 250 and 1000 Hz. The modulating frequency was the parameter of the data. Data averaged across three subjects. Vertical lines in all diagrams show the value of standard deviation.

In the case of dichotic presentation ($m_l \neq m_r$), the subject's task was more difficult as the resultant AM sound image was not perfectly fussed. The task was particularly difficult for large interaural differences in the modulation depth, $\Delta m = m_l - m_r$, and especially when $m_r = 0$, with $m_l \rightarrow 100\%$. Figure 3 shows binaurally matched modulation depth, $m$, averaged for three subjects, as a function of the interaural difference in modulation depth $\Delta m$, for the carrier frequency of 1000 Hz, for $m_r$ equal to: 0, 10, 20 and 60% respectively. The value of the modulating frequency is the parameter of the curves.

It follows from Fig. 3 that the binaurally matched modulation depth $m$ grows along with the growth of the interaural difference in modulation depth $\Delta m$. For small $\Delta m$, the binaurally perceived $m$ is almost linearly related to $\Delta m$. For large $\Delta m$, $f(\Delta m)$ is no longer linear and, additionally, depends on $f_m$, particularly for small values of $m_r$. The standard deviations of measured $m$ values grow along with the growth of $\Delta m$.

It was interesting to refer the binaurally determined values of $m$ to the values which would be obtained on assumption that AM modulated signals, presented to the left and right ears, undergo, some linear summation [19]. Let us assume that input AM signals

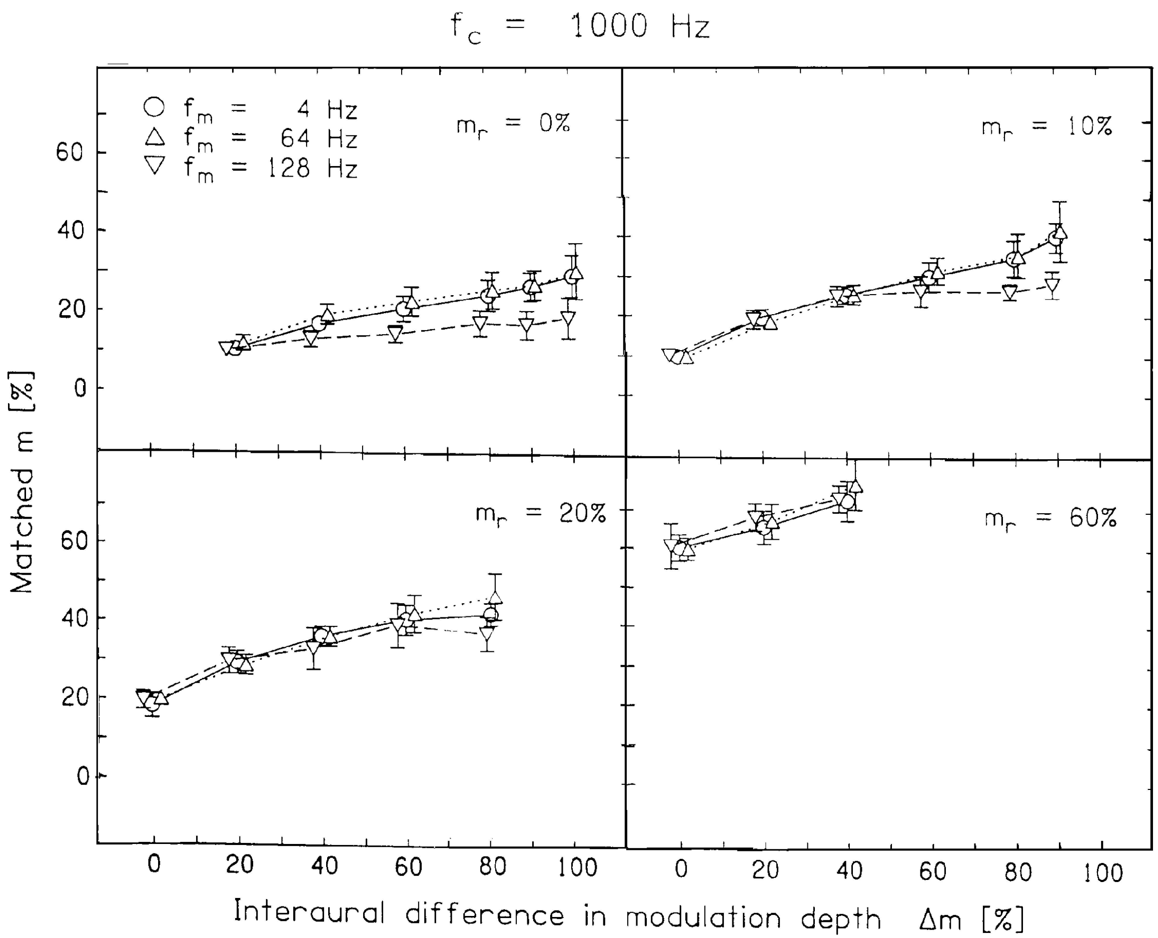


Fig. 3. Dependence of the binaurally perceived modulation depth ($m$) on the interaural difference in modulation depth, $\Delta m = m_l - m_r$, under dichotic conditions of perception ($m_l \neq m_r$). The signal carrier frequency equal 1000 Hz. The modulating frequency is the parameter of the curves. Data averaged across three subjects.

presented to the right and left ears have the following form:

$$x_r(t) = X_r\,[1 + m_r \sin(2\pi f_m t)] \sin(2\pi f_c t), \tag{1}$$

$$x_l(t) = X_l\,[1 + m_l \sin(2\pi f_m t)] \sin(2\pi f_c t), \tag{2}$$

where $X_r$ and $X_l$ are amplitudes of carrier signals, $m_r$ and $m_l$ are coefficients of modulation depth presented to the right and left ears, $f_m$ and $f_c$ are modulating and carrier frequencies of AM signals. Adding (1) and (2) and grouping terms we get

$$x_r(t) + x_l(t) = (X_r + X_l)\left[1 + \frac{X_r m_r + X_l m_l}{X_r + X_m} \sin(2\pi f_m t)\right] \sin(2\pi f_c t). \tag{3}$$

Expression (3) has the form of an equation describing AM modulated signal, for which modulation depth $m$ equals

$$m = \frac{X_r m_r + X_l m_l}{X_r + X_l}\,. \tag{4}$$

For small interaural differences in modulation depth, amplitudes of carrier signals $X_r$ and $X_l$ are nearly equal. In this case expression (4) is simplified to the form

$$m = \frac{m_r + m_l}{2}\,. \tag{5}$$

Hence, for small values of $\Delta m$, binaurally perceived modulation depth $m$ is equal to the arithmetic mean of the value of depth coefficients presented to both ears. For large values of $\Delta m$, amplitudes of carrier signals are not equal ($X_r \neq X_l$). Assuming a constant value of modulation depth in one ear (e.g. $m_r$) and changing the modulation depth in the other ear one can find a set of curves defining $m = f(\Delta m)$. The curves, obtained in accordance with expression (4), are shown in Fig. 4 as continuous lines.

As can be seen in this figure, for small and medium values of $\Delta m$, experimental and theoretical data match quite well. The perceived modulation depth is approximately proportional to $\Delta m$. However, for large $\Delta m$ values, particularly when $\Delta m \to 100\%$, certain differences between the experimental and theoretical data begin to appear. The differences are clearly seen for $f_m = 128$ Hz, i.e. when the evaluation of the modulation depth between the standard and the test does not result from the difference in the intensity (loudness) fluctuation but from the difference in the spectrum of the stimuli i.e. when spectral perception mechanism of the modulation is involved. This fact suggests that for a high rate of modulation and large interaural differences in modulation depth apart from the linear summation of AM signals from both ears an additional process of the binaural mechanism is triggered.

## 4. Experiment II. Binaural perception of FM signals

At the initial stage of Experiment II the perception of the binaurally perceived frequency deviation was tested under diotic conditions, i.e. when set frequency deviations in successive pairs of stimuli were the same (cf. Fig. 1.3). The aim of this initial stage of the experiment was to determine the subjects' ability to evaluate the binaurally perceived

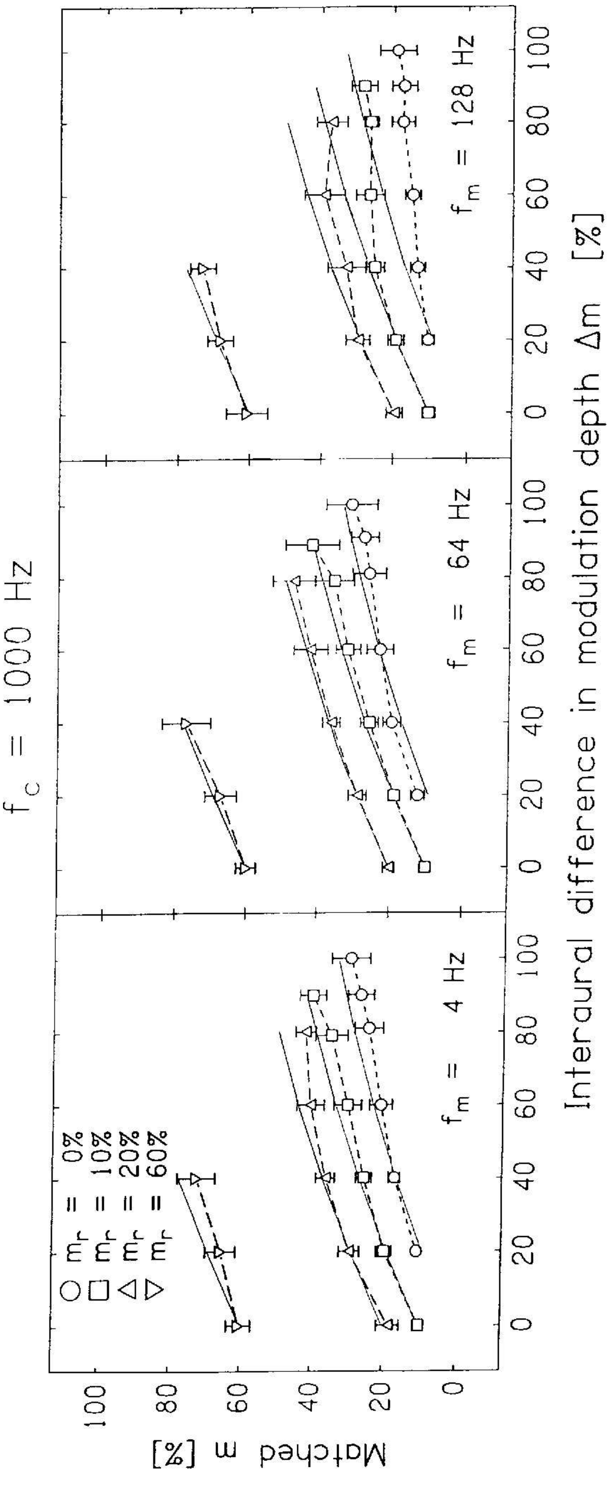


Fig. 4. Comparison of the binaurally perceived modulation depth $m$ determined experimentally (broken curves) with the values calculated (solid curves), under the assumption of linear summation of AM signals, for the carrier frequency of 1000 Hz and three modulating frequencies: 4, 64 and 128 Hz.

frequency deviation for selected modulating and carrier frequencies. Figure 5 shows the dependence of the perceived frequency deviation, averaged for three subjects, on the deviation presented for case $\Delta f_l = \Delta f_r$. The frequency of the carrier signals was $f_c = 500$ and 1000 Hz. Modulating frequencies $f_m = 4$, 32, 64, and 128 Hz were the parameters of the curves.

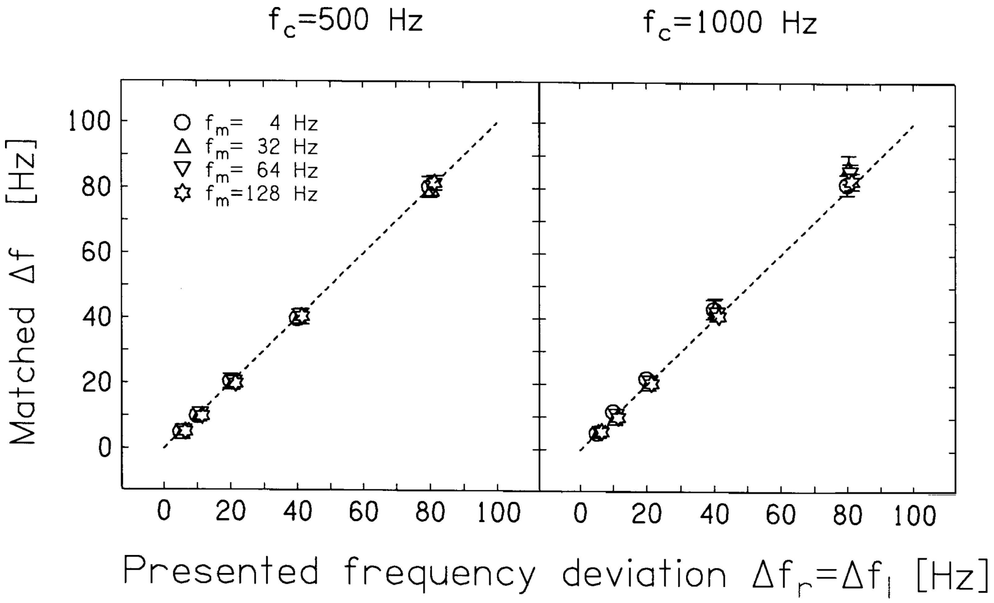


Fig. 5. Dependence of the binaurally perceived frequency deviation ($\Delta f$) on the frequency deviation presented to the left ($\Delta f_l$) and right ($\Delta f_r$) ear, under conditions of diotic presentation ($\Delta f_l = \Delta f_r$). The frequency of carrier signals equal 500 and 1000 Hz. The modulating frequency is the parameter of the data. Data averaged across three subjects.

The diagonal broken lines represent the linear (ideal) dependence of the perceived value of deviation on that presented. As can be seen in Fig. 5 the results of the measurements well match the broken line, which indicates high ability of subjects to evaluate frequency deviation of FM signals. On this basis we can state that in the case of diotic presentation, the perceived frequency deviation is equal (within the measurement error) to the value of the presented deviation, both for small deviation changes, i.e. within the range of loudness changes ($f_m = 4$ Hz), roughness changes ($f_m = 32$ and 64 Hz), and within the range in which deviation changes are perceived as changes in the stimulus timbre ($f_m = 128$ Hz). One can also say that under conditions of diotic presentation the frequency deviation perceived by the subject, $\Delta f$, is equal to the arithmetic mean of the deviation presented to the right, $\Delta f_r$ and left, $\Delta f_l$, ears, i.e. that $\Delta f = (\Delta f_l + \Delta f_r)/2 = \Delta f_l = \Delta f_r$ for ($\Delta f_r = \Delta f_l$). It also follows from Fig. 5 that the diotically presented frequency deviation does not depend on the carrier and modulating frequencies.

The basic stage of the experiment focused on the determination of the binaurally perceived frequency deviation for dichotic presentation, ($\Delta f_r \neq \Delta f_l$) depending on the

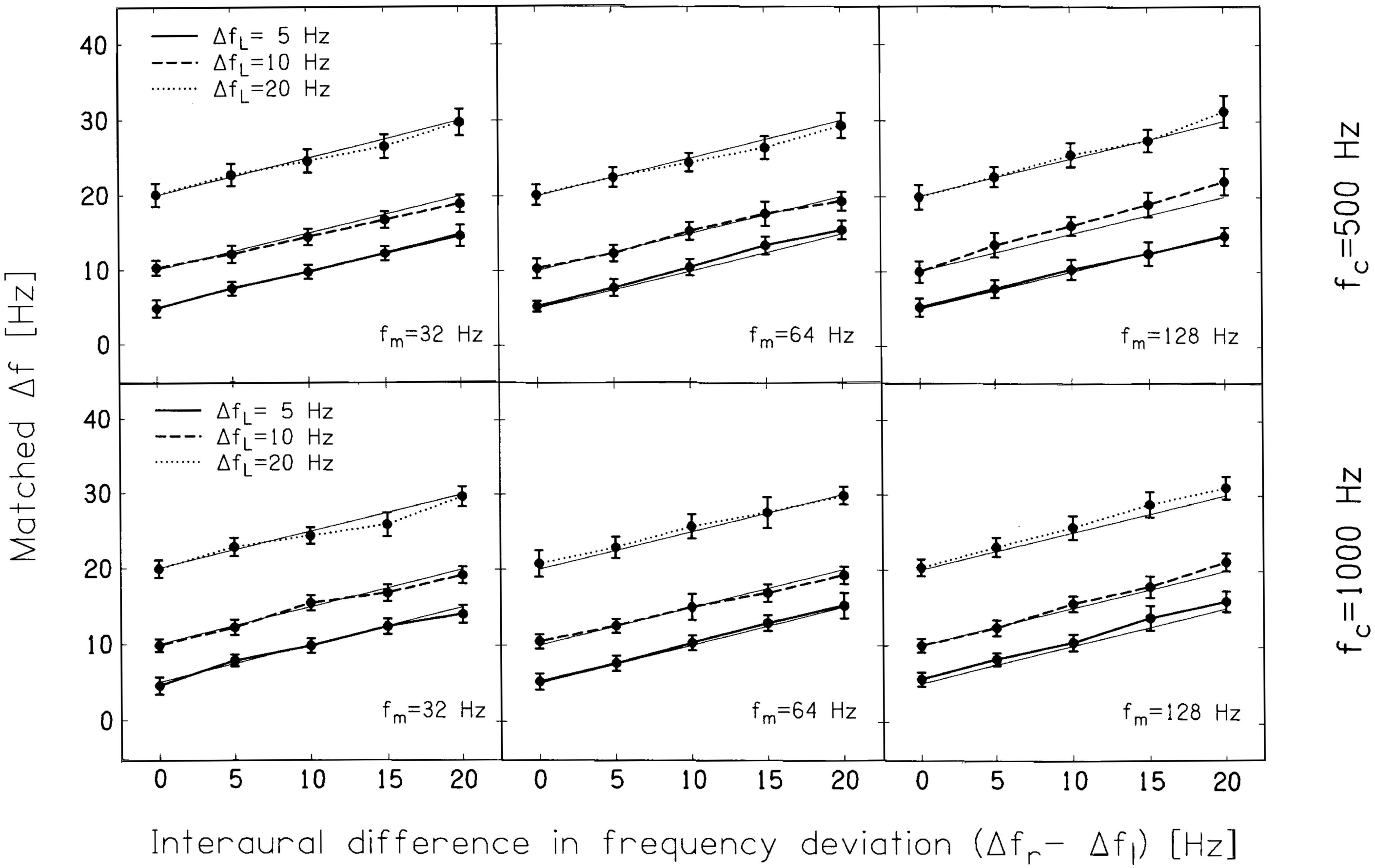


Fig. 6. Dependence of the binaurally perceived frequency deviation ($\Delta f$) on the interaural difference in frequency deviation ($\Delta f_r - \Delta f_l$), under conditions of dichotic presentation ($\Delta f_r \neq \Delta f_l$). The value of frequency deviation presented to the left ear ($\Delta f_l$) is the parameter of the curves. The thin lines represent the arithmetic mean of deviations presented to the left and right ears. Carrier frequencies: 500 and 1000 Hz, modulating frequencies: 32, 64 and 128 Hz. Data averaged across three subjects.

interaural difference in frequency deviation $\delta(\Delta f) = \Delta f_r - \Delta f_l$. It should be stressed that the deviation difference in this experiment had to be selected so that the resultant sound was binaurally fused (integrated). The experiments were conducted for carrier signals with frequencies of $f_c = 500$ and 1000 Hz and modulating signals with frequencies of $f_m = 32$, 64 and 128 Hz.

Figure 6 shows the dependence of the matched frequency deviation, $\Delta f$, averaged for three subjects, on the interaural frequency deviation $\delta(\Delta f)$ for two carrier frequencies 500 and 1000 Hz. Consecutive panels show results for modulating frequencies applied in the experiment. The set value of frequency deviation presented to the left ear, $(\Delta f_l)$, is the parameter of the curves. The solid line indicates experimental data of perceived matched frequency deviation for $\Delta f_l = 5$ Hz, broken line for $\Delta f_l = 10$ Hz and dotted line for $\Delta f_l = 20$ Hz. The results obtained for the dichotic conditions indicate that the dependence of the perceived frequency deviation on the interaural difference of this deviation may be described by a linear function. This function does not depend on the deviation presented to the left ear and has a similar trace for carrier frequencies of 500 and 1000 Hz.

The thin lines in these figures show arithmetically averaged values of deviation presented to the left and right ears, in accordance with $\Delta f = (\Delta f_l + \Delta f_r)/2$. As can be seen, both for carrier frequency of 500 Hz and 1000 Hz and for the modulating frequencies used, the values of the matched frequency deviation for $\Delta f_l = 5$, 10 and 20 Hz, are in agreement with the arithmetic means. This means that within the parameter range tested, frequency deviation is an arithmetic mean of the deviation presented to the left and right ears.

## 5. Discussion

The data obtained in the first part of Experiment I, related to the diotic presentation of AM signals, revealed that the subjects' ability to evaluate modulation depth was very high for all parameters of AM stimuli measured. This was the starting point of the basic part of Experiment I, i.e. the dichotic presentation of modulation depth for AM signals. Results of the experiments showed that for small interaural differences in modulation depth, $\Delta m$, matched $m$ is equal to the arithmetic mean of $m_l$ and $m_r$. However, for large values of $\Delta m$ and high modulation frequencies, the binaurally perceived modulation depth becomes smaller than the arithmetic mean $m_l$ and $m_r$, and $m$ is decreasing when $\Delta m$ approaches 100%. The characteristic features of AM signals are considerable fluctuations of their intensity, which can be expressed as follows:

$$\Delta L = 10 \lg \frac{I_{\max}}{I_{\min}} = 20 \lg \left( \frac{1+m}{1-m} \right), \qquad \text{at} \quad m \neq 1.$$

For large values of modulation depth, these fluctuations can be quite significant. It should be noted that the binaural hearing system is rather sensitive to changes of the interaural intensity difference because the interaural discrimination threshold is about 0.5 dB. On the other hand, an interaural intensity difference of the order 15 – 20 dB determines the limit of the perceived binaural effects such as: lateralization or localization of the sound source. Physiological studies have revealed that single fibres of the auditory nerve are characterized by the growing discharge rate when the sound level increases but only in a limited dynamic range (SUGA [29]). This dynamic range is even smaller for the fibres of the central auditory nerve system, and their neural activity reveals considerable nonlinearity. Therefore, for large differences in the interaural modulation depth, temporal changes in intensity of AM signals may not be linearly projected into the fibre discharge rate. This fact accounts to some extent for nonlinear trends in $m = f(\Delta m)$ functions for large $\Delta m$ seen in Fig. 4.

The calculations presented in this paper, based on the concept of linear summation of AM signals resulting from data on the binaural detection threshold and binaural loudness, do not pretend to be the modelling of the binaural perception of the modulation depth. They do not take into account a number of important functions of the binaural system such as transformation and filtering imposed on the signals by the external and middle ears, coincidence-correlation mechanism of the neural interaction between the left and right ears at higher level of the auditory tract, mechanism of central masking etc., which are taken into account in most binaural models. These calculations have shown that the mechanism of binaural neural interaction based on the linear summation of AM signals produces calculation results, which correspond fairly well to the measurement data. On this basis one can think that this mechanism plays a significant role in the binaural perception of modulation depth of AM signals.

With respect to the binaural perception of FM signals, on the basis of the first part of Experiment II on the diotic presentation of FM signals it was found that the subjects' ability to evaluate the frequency deviation of these signals was very high. The basic part of the experiment on the dichotic presentation of frequency deviation ($\Delta f_l \neq \Delta f_r$) revealed that this deviation is equal to the arithmetic mean of deviations presented to the right and left ears. Consequently, one can say that within the parameter range of AM and FM signals the mechanisms of binaural interaction of these signals are similar. The models of binaural perception (STERN and TRAHIOTIS [28]) generally assume that the discharges occurring in the neurons coming from both ears are compared within the auditory filters having similar characteristic frequencies. Each filter is additionally connected to a delay system and then to the coincidence detector which counts the beats coming synchronically from each ear. Interaural time differences and interaural intensity differences are coded so as to obtain the strongest response of the coincidence detectors. This coincidence, however, occurs in a limited range of frequency deviation changes, up to about 20 Hz. An increase of this range most probably leads to the drop of the coincidence of neuron discharges coming from the left and right ears. The lack of binaural fusion for the presented signals could be the consequence of this.

In conclusion it is worth stressing that the binaural perception of modulated signals whose amplitude and frequency varying in time largely correspond to the perception of real signals with parameters varying in time (speech and music). Binaural perception of this variability and the results obtained could be significant for investigations into the intelligibility of speech and perception of music in a room (BLAUERT [3]; HOUTGAST and STEENEKEN [10]; OZIMEK and SĘK [20]).

## 6. Conclusions

1. Binaurally perceived modulation depth for AM signals, determined under diotic conditions ($m_l = m_r$), is equal to monaurally perceived modulation depth, irrespective of the carrier and modulating frequencies.

2. Binaurally perceived modulation depth for AM signals, determined under dichotic conditions ($m_l \neq m_r$) is equal to the arithmetic mean of modulation depth presented to both ears only in the range of small interaural differences $\Delta m$. For large interaural differences $\Delta m$ perceived modulation depth is smaller than the arithmetic mean of $m_l$ and $m_r$, and function $m = f(\Delta m)$ is nonlinear.

3. Binaurally perceived frequency deviation for FM signals, determined under diotic conditions ($\Delta f_l = \Delta f_r$), is equal to the monaurally perceived frequency deviation, irrespective of the carrier and modulating frequencies.

4. Binaurally perceived frequency deviation for FM signals, determined under dichotic conditions ($\Delta f_l \neq \Delta f_r$), is a linear function of interaural difference of frequency deviation. Under these conditions perceived deviation is equal to the arithmetic mean of deviations presented to both ears. It does not depend on the carrier and modulating frequencies used.

## Acknowledgement

This work was done as part of the research project (promotor grant) 7T07B00814 financed by the Committee of Scientific Research and the research project financed by A. Mickiewicz University.

## References

[1] L.R. Bernstein and C. Trahiotis, *Lateralization of low-frequency, complex waveforms: The use of the envelope-based temporal disparities*, J. Acoust. Soc. Am. 77, 1868-1880 (1985a).

[2] L.R. Bernstein and C. Trahiotis, *Lateralization of sinusoidally amplitude-modulated tones: Effects of spectral locus and temporal variation*, J. Acoust. Soc. Am., **78**, 514–523 (1985b).

[3] J. Blauert, *Spatial hearing*, The MIT Press, Cambridge, Massachusetts 1983.

[4] J.J. Groen, *Super- and subliminal binaural beats*, Acta Otolaryngol., **57**, 224–231 (1964).

[5] X. Gu, B.A. Wright and D.M. Green, *Failure to near binaural beats below threshold*, J. Acoust. Soc. Am., **97**, 701–703 (1995).

[6] L.M. Heller and C. Trahiotis, *Extents of laterality and binaural interference effects*, J. Acoust. Soc. Am., **99**, 3632–3637 (1996).

[7] R.P. Hellman and J.J. Zwislocki, *Monoural loudness function at 1000 cps, and interaural summation*, J. Acoust. Soc. Am., **35**, 856–865 (1963).

[8] G.B. Henning, *Some observations on the lateralization of complex waveforms*, J. Acoust. Soc. Am., **68**, 446–454 (1980).

[9] G.B. Henning and J. Ashton, *The effect of carrier and modulation frequency on lateralization based on interauralphase and interaural group delay*, Hear. Res., **4**, 185–194 (1981).

[10] T. Houtgast and H.J. Steeneken, *Review of the MTF concept in room acoustics and its use for estimating speech intelligibility in auditoria*, J. Acoust. Soc. Am., **77**, 1061–1077 (1985).

[11] W. Jesteadt and C.C. Wier, *Comparison of monaural and binaural discrimination of intensity and frequency*, J. Acoust. Soc. Am., **61**, 1599–1603 (1977).

[12] J. Keys, *Binaural versus monaural hearing*, J. Acoust. Soc. Am., **19**, 629–631 (1947).

[13] J.C.R. Licklider, J.C. Webster and J.M. Hedlun, *On the frequency limits of binaural beats*, J. Acoust. Soc. Am., **22**, 468–473 (1950).

[14] L.E. Marks, *Binaural summation of the loudness of pure tones*, J. Acoust. Soc. Am., **65**, 107–113 (1978).

[15] D.M. McFadden and E. Pasanen, *Lateralization at high frequencies based on interaural time differences*, J. Acoust. Soc. Am., **59**, 634–639 (1976).

[16] L. Mendoza, J.W. Hall and J. Grose, *Within- and across-channel processes in modulation interference*, J. Acoust. Soc. Am., **97**, 3072–3079 (1995).

[17] J.M. Nuetzel and E.R. Hafter, *Lateralization of complex waveforms: effects of fine structure, amplitude, and duration*, J. Acoust. Soc. Am., **60**, 1339–1346 (1976).

[18] J.M. Nuetzel and E.R. Hafter, *Lateralization of complex waveforms: Spectral effects*, J. Acoust. Soc. Am., **69**, 1112–1118 (1981).

[19] E. Ozimek, J. Konieczny and T. Sone, *Dichotic perception of modulation depth of AM signals*, Proceedings of the Acoustical Society of Japan, Honolulu, Hawaii 2-6 December, pp. 629–634 (1996).

[20] E. Ozimek and A. Sęk, *AM and FM difference limens and their reference to amplitude-frequency changes of a sound in a room*, Acta Acustica, **82**, 114–122 (1996).

[21] D.R. Perrott and M.A. Nelson, *Limits for the detection of binaural beats*, J. Acoust. Soc. Am., **46**, 1477–1481 (1969).

[22] D.R. Perrott and A.D. Musicant, *Rotating tones and binaural beats*, J. Acoust. Soc. Am., **61**, 1288–1292 (1977).

[23] I. Pollack, *Monaural and binaural threshold sensitivity for tones and for white noise*, J. Acoust. Soc. Am., **20**, 52–57 (1947).

[24] G.S. Reynolds and S.S. Stevens, *Binaural summation of loudness*, J. Acoust. Soc. Am., **32**, 1337–1344 (1960).

[25] R.C. Rowland and J.V. Tobias, *Interaural intensity difference limens*, J. Speech Hearing Res., **10**, 745–756 (1967).

[26] B. Scharf and D. Fishken, *Binaural summation of loudness: Reconsidered*, J. Exp. Psycho., **37**, 229–242 (1970).

[27] W.A. Shaw, E.B. Newman and I.J. Hirsh, *The difference between monaural and binaural thresholds*, J. Exp. Psycho., **37**, 229–242 (1947).

[28] M.R. Stern and C. Trahiotis, *Models of binaural interaction*, [in:] Hearing, Brian C.J. Moore [Ed.], Academic Press, 347–385 (1995).

[29] N. Suga, *Philosophy and stimulus design for neuroethology of complex-sound processing*, [in:] Processing of Complex Sounds by the Auditory System, R.P. Carlyon, C.J. Darwin and I.J. Russell [Eds.], Clarendon Press Oxford, pp. 105–108 (1992).

[30] J.V. Tobias, *Application of a "relative" procedure to a problem in binaural-beat perception*, J. Acoust. Soc. Am., **35**, 1442–1447 (1963).

[31] A. Wicher and E. Ozimek, *Binaural perception of FM signals* [in Polish], Materiały OSA'98 Poznań – Kiekrz, 657–662 (1998).

ARCHIVES OF ACOUSTICS
**25**, 2, 147–155 (2000)

# NEW TIMBRES OF ST. CATHERINE'S CARILLON

G. BUDZYŃSKI, M. SANKIEWICZ

Technical University of Gdańsk
Department of Sound Engineering
(80-952 Gdańsk, Narutowicza 11/12, Poland)
e-mail: eda@sound.eti.pg.gda.pl

G. SZYCHLIŃSKI

The Museum of History of Gdańsk
(80-831 Gdańsk, Długa 47, Poland)
e-mail: zegary@ns.com.pl

St. Catherine's carillon, the largest instrument of its kind in Poland, deserves special attention due to its particular acoustic properties. They were investigated in detail and relevant results reported earlier. Recently, the acoustic possibilities of the carillon and its sound repertory has been significantly augmented thanks to twelve new bells added to the 37 existing so far, and the newly installed keyboard, enabling the carillonist direct exciting of bell sounds. Thanks to the enlarged carillon sound scale and the direct mechanical coupling of keyboard keys to bells, the carillonist gains an enriched possibility of creating new chords and complex timbres resulting in several bells being struck either together or subsequently. These timbres were actually investigated with the same method and equipment as applied during the former investigations, mentioned above. The selected carillon sounds were recorded and the recorded samples analyzed digitally by means of dedicated computer software programs. The results confirm the high quality of the enlarged part of the carillon, comparable to the very high quality of the instrument existing so far. Conclusions concerning particular properties of the St. Catherine carillon are presented at the end of the paper.

## 1. Introduction

St. Catherine's church, with its monumental belfry-tower, is of important historic value. The tower the construction of which began in 1450 was, for political reasons, not completed until the years 1484 – 1486. In 1634 the gothic roof of the tower was transformed into a beautiful baroque copula, designed by Jacob van den Block [7]. Its exact reconstruction can once more be admired to-day (see Fig. 1).

Much more is to be admired inside the tower. The most spectacular, or rather "auricular", are St. Catherine's bells. Their ringing sounds are well audible over the whole area

Fig. 1. St. Catherine's belfry tower dominating the Old City roofs.

of the Old City of Gdańsk. Not only do they strike hours and sound peals, but also play melodies, thanks to an ingenious facility called the "carillon". The St. Catherine's carillons had a long and interesting history. The one, existing at present, was reconstructed thanks to an initiative of Mr. Hans Eggebrecht, who in 1989 offered the instrument as replacement of the previous one destroyed during the war. The instrument which then consisted of 37 bells was equipped only with an automatic play facility. This instrument, being almost a unique carillon in Poland, underwent extended acoustical investigations. In the meantime, their results were published extensively [1, 4 – 6].

The need to return again to the subject of St. Catherine's carillon arose, however, due to the fundamental improvement of the acoustic qualities of the instrument. In 1998, thanks to financial support of the Gdańsk municipality and individual donators, a further 12 bells were added. A complete mechanical action system was also installed, enabling manual playing on the instrument from a traditional keyboard (Fig. 2). Thus, now, the instrument, with its 49 bells, has become the greatest concert-carillon in Central and

Eastern Europe [7]. Acoustic properties of such carillon deserve to be well known among sound engineers interested in musical instruments. It is the purpose of this paper to supply relevant data and add notices concerning instrument quality.

Fig. 2. St. Catherine's carillon keyboard (the chromatic scale of 49 keys and the transmission rods are well visible, the pedal keys are suspended below).

One more item to be admired inside St. Catherine's tower should be mentioned: the Museum of Tower Clocks [7]. They also enter into the scope of interest of sound engineers, due to their ringing facilities for hour striking, which use clock bells particularly shaped, to produce the sound of a particular clock-timbre. This subject, however, needs separate treatment.

## 2. Results of earlier studies

As mentioned above, the acoustic properties of St. Catherine's carillon sounds were investigated by the present writers, a few years ago, in order to become acquainted with this special type of musical instruments, and, among others, to check the quality of the internal and external tuning of carillon bells. The results presented in part one of Table 1, prove a very good quality of the 37 bells investigated, made by the renowned

**Table 1.** Tuning deviations of the St. Catherine's carillon (in cents).

| | Hum | Prime | Third | Fifth | Octave | Tenth | Twelfth | Upper Oct. |
|---|---|---|---|---|---|---|---|---|
| Part one: | | | | | | | | |
| 1. c′ | 7 | 1 | 3 | −2 | 1 | −10 | 9 | 68 |
| 2. cis′ | −2 | 2 | 4 | 23 | 4 | −21 | 11 | 73 |
| 3. d′ | 14 | 0 | 3 | 50 | 3 | 21 | 12 | 75 |
| 4. dis′ | | 6 | | 29 | 4 | −28 | 9 | 75 |
| 5. e′ | 1 | 5 | 5 | 4 | −9 | −19 | 16 | 80 |
| 6. f′ | | 5 | 0 | 7 | 8 | −60 | 16 | 82 |
| 7. fis′ | 9 | 1 | 4 | −42 | 3 | 6 | 10 | 73 |
| 8. g′ | −1 | 3 | 5 | −63 | 3 | −41 | 18 | 86 |
| 9. gis′ | −3 | −1 | 4 | 17 | 3 | 43 | 14 | 72 |
| 10. a′ | | | 4 | 26 | 3 | 43 | 14 | 78 |
| 11. ais′ | 5 | | 6 | 17 | 5 | 49 | 18 | 86 |
| 12. h′ | | 7 | 4 | 12 | 3 | | 18 | 86 |
| 13. c″ | 4 | 3 | 5 | 13 | 4 | 47 | 12 | 55 |
| 14. cis″ | 3 | 3 | 3 | 19 | 4 | 62 | 9 | 67 |
| 15. d″ | 3 | | 4 | | 4 | 62 | 14 | 77 |
| 16. dis″ | 2 | 4 | 2 | 5 | 5 | −31 | 13 | 75 |
| 17. e″ | 5 | 4 | 5 | −2 | 6 | −58 | 13 | 74 |
| 18. f″ | | 3 | 5 | 13 | 4 | −14 | 10 | 70 |
| 19. fis″ | | 4 | 4 | | 3 | −26 | 7 | 64 |
| 20. g″ | 4 | 7 | 6 | 0 | 6 | | 11 | 67 |
| 21. gis″ | | 3 | 3 | 4 | 5 | −27 | 14 | 77 |
| 22. a″ | 2 | 4 | 5 | 16 | 5 | −36 | 12 | 72 |
| 23. ais″ | | 4 | 6 | | 6 | −29 | 13 | 82 |
| 24. h″ | | | | | | | | |
| 25. c‴ | 2 | 3 | 3 | | 4 | | −1 | 11 |
| 26. cis‴ | 3 | 4 | 9 | 27 | 5 | 15 | 1 | 52 |
| 27. d‴ | 4 | 3 | 4 | | 6 | 27 | 2 | 79 |
| 28. dis‴ | 3 | 4 | 4 | | 6 | −35 | −6 | 40 |
| 29. e‴ | 3 | 6 | 5 | | 6 | 42 | −3 | |
| 30. f‴ | 3 | 4 | 6 | | 4 | −10 | −10 | 32 |
| 31. fis‴ | 3 | 4 | −7 | | 2 | −66 | −26 | |
| 32. g‴ | 5 | 4 | 6 | | 6 | | −14 | 21 |
| 33. gis‴ | 6 | 3 | 11 | | 4 | 44 | −23 | 3 |
| 34. a‴ | 5 | 5 | 6 | | −4 | | −22 | 3 |
| 35. ais‴ | 5 | 6 | 8 | | 4 | | | |
| 36. h‴ | 5 | 4 | 15 | | 4 | 6 | −36 | 76 |
| 37. c⁗ | 3 | 3 | −7 | | −2 | | −36 | −22 |

**Table 1.** [cont.]

| | Hum | Prime | Third | Fifth | Octave | Tenth | Twelfth | Upper Oct. |
|---|---|---|---|---|---|---|---|---|
| Part two: | | | | | | | | |
| 38. cis'''' | | −4 | 7 | | −5 | | −42 | |
| 39. d'''' | −4 | −3 | 6 | | −5 | | −47 | |
| 40. dis'''' | −4 | −4 | −3 | | | | | |
| 41. e'''' | 1 | | 13 | | −2 | 30 | −60 | |
| 42. f'''' | −4 | −7 | 6 | | | | | |
| 43. fis'''' | −2 | −5 | 15 | | −4 | | | |
| 44. g'''' | −2 | −4 | 10 | | | | | |
| 45. gis'''' | 21 | −2 | 7 | | −3 | | | |
| 46. a'''' | | −2 | 8 | | −3 | | | |
| 47. ais'''' | −2 | | 12 | | −1 | | | |
| 48. h'''' | 0 | 2 | 11 | | | | | |
| 49. c''''' | −4 | −2 | 7 | | | | | |

Blank spaces denote lack of a measurement result.

Dutch foundry Koninklijke Klokkengieterij Eijsbouts in Asten, and of their successful installation by this factory, in St. Catherine's belfry.

Recordings of the carillon sounds were then done electroacoustically *in situ* within the belfry. Single sounds were excited using a MIDI keyboard, switched into the instrument control panel, from whence, electromagnetically driven hammers were actuated at every bell. The recording microphone was situated on a gallery, on a level with the bells, and sounds were recorded with a digital recorder MZ 1; only one channel being used for further processing and analysis. Recorded sounds were analyzed in the laboratory using either professional software (Sound Designer II) or specially designed own program. More details on the then used equipment and method applied are contained in the above mentioned own publications. Special questions were also studied on the example of St. Catherine's carillon, in particular those concerning peculiar properties of the sounds of large, swinging bells [6].

## 3. Recent investigation

Basically, the same method was used as before, i.e., sounds of 12 newly installed bells (Fig. 3) were recorded and analyzed, yet, a different sound excitation manner was applied. Instead of the MIDI keyboard the new installed manual keyboard was used. Consequently, the sound intensity obtained may differ slightly for particular notes.

The results obtained are presented in part two of Table 1.

It should be pointed out, however, that the enlarged carillon became an almost new instrument, with new timbres available. Thanks to the installed facilities for manual playing it now exhibits many new acoustic properties.

Fig. 3. The twelve, new installed carillon bells (control levers of mechanical action are visible).

First of all, they are due to newly installed clappers and hammers. When previously, all 37 bells were struck from outside by electromagnetically driven hammers, now, they are struck by mechanically pulled clappers (Fig. 4), or hammers for the four largest swinging bells. These clappers are hung excentrically within the bell mouth in order to reduce the idle motion of action wires and manual keys. Every fixed bell is equipped with an inner rod enabling installation of a spring, which prevents unintended manifold strokes (oscillations) of the clapper against the bell body. This facility was necessary for a few bells only, as for others the clapper masses were sufficient to prevent any unwanted oscillation.

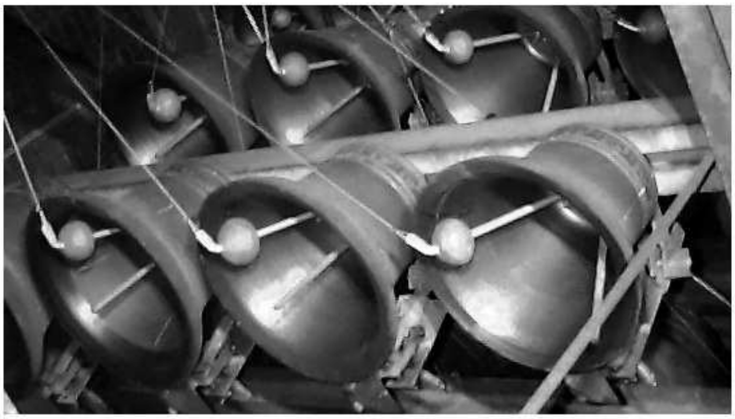

Fig. 4. Carillon bells equipped with a new mechanical system of clappers and pull wires (electromagnetic outer hammers are also visible).

Each of the four largest bells, equipped primarily with clappers (for swinging peals) and electromagnetic hammers (for automatic play, steered from the digital memory) now received an additional hammer, driven by a mechanical action wire (Fig. 5). Thus, hammers are controlled directly from the keyboard levers, using hand or foot strokes of appropriate energy.

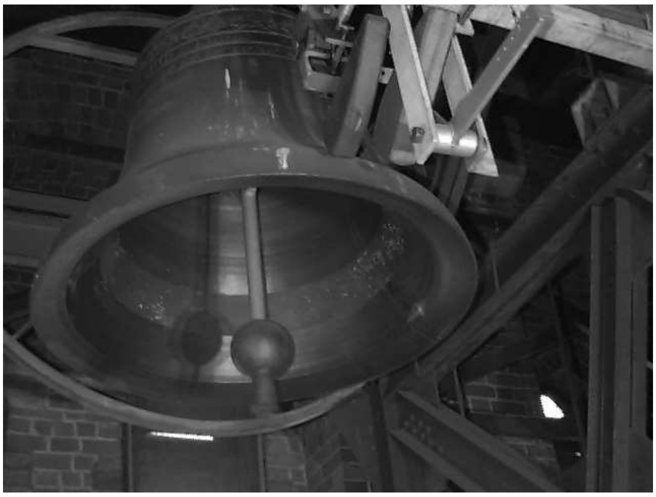

Fig. 5. The largest bell (swinging) with a traditional clapper and two outer hammers: mechanic and electromagnetic one.

The system of mechanical action allows the player to employ variable dynamics of notes played, in contrast to the case of automatic play. Variable dynamics cause variations of timbre, i.e. of spectral content of particular notes. This makes the investigation of the timbre of carillon sounds, which depends on the sound excitation level, much more difficult.

A totally different excitation tool (clapper from inside, vs. hammer from outside) implies a further need for a comparative study of bell sounds excited in both manners mentioned. Although such comparative studies were reported in the literature [3], they were restricted to experiments in laboratory conditions. Thus it seemed reasonable to check and compare results obtained from the existing instrument.

Mechanical action gives the player total freedom in creating time sequences of notes or chords, unattainable e.g. with the electromagnetic action steered from a MIDI system keyboard. Every execution of a piece of music is a genuine one, in contrast to sounds produced by the automatic play system. Thus, music played by a well trained carillonist becomes a true concert activity [2].

## 4. Subjective assessment

Objective analyses in the domain of Musical Acoustics are inseparably bound with subjective assessments, in particular when applied to quality ranking of musical instruments. Listening to recorded melodies played using the carillon investigated, done before, and after its enlarging, might serve as an example for a comparative assessment method.

Preservation of strictly maintained constant values of all recording conditions in both cases would be necessary. This is, however, impossible, because of the mere fact of the existence of all newly installed elements and facilities within the tower, having changed its acoustic properties significantly. Despite the impossibility of exact realization of such comparison, the two monophonically recorded melodies are presented as illustrations, enabling attempts of subjective judgements to be made.

## 5. Critical remarks

It should be emphasized that the properties of the instrument investigated were compared to those reported on other great carillons existing in Western Europe [2, 3]. Such comparisons fully justify the very high ranking of St. Catherine's carillon, and its role as a great concert instrument.

It is obvious from the reported results and observations that the presented investigation should be treated as a preliminary one. St. Catherine's great carillon reveals an extended, rich field of interesting acoustical problems, requiring a systematic effort on the part of investigators to be solved successfully. Thus, further studies and investigations are highly desirable.

In contrast to many scientific projects carried out in laboratory conditions, many difficulties arise in practical realization of the reported investigations.

Recordings should be done rather outdoors, at half the distance from the tower, typical for passers-by willing to listen to carillon sounds. This condition is hard to fulfill due to the intense traffic noise from the neighbourhood of the tower. Using night-time for recordings might be a remedy, yet the necessary, intense ringing at night would disturb the quietness of the night for the neighbourhood residents.

The situating of the measuring microphone inside the tower, well insulated from external noise, thanks to very thick tower walls (about 4 m), ensured the required quality of recording. Disadvantageous were, however, possible resonances in the tower interior. These may affect the results of spectral analyses. Thus, frequential characteristics of the reverberation within the tower interior should be measured, and their shape used for possible interpreting of the reported results. The moreso that the measured sound spectra were highly non-uniform.

The precision of the data obtained from analyses is slightly reduced due to the presence of low frequency beats, being below the threshold of frequential sensitivity of the applied method of analysis. Beats in bell sounds are, of course, inevitable, yet the reduction of precision is so small that it may be disregarded. It should be pointed out here that beats in bell sounds are, to some extent, subjectively desirable [2].

## 6. Conclusion

The St. Catherine's carillon built in 1989 and enlarged over the next ten years is a great instrument of important musical value and of the highest technological quality.

The investigated properties of St. Catherine's carillon, first of all the high accuracy of internal and external tuning of all the 49 carillon bells, proves its highest quality and ensures its beautiful sound. The bells are tuned according to the chromatic, equally tempered scale, ranging from $c'$ to $c^V$ (i.e. from C4 to C8), covering the complete four octaves.

The console containing manual and pedal keyboards situated inside a sound insulating cabin offer the carillonist good conditions even during prolongued concerting.

## References


[1] G. Budzyński, J. Gudel and M. Sankiewicz, *Timbre of the Gdańsk historical bells and carillons*, Preservation of the Industrial Heritage, Gdańsk Outlook p. 73–90, Technical University of Gdańsk, 1993.

[2] E. Leipp, *Aspects technologique et acoustiques du carillon*, Bull. du GAM, No. 66, Paris 1973.

[3] T.D. Rossing (Ed.), *Acoustics of bells*, Van Nostrand Reinhold, New York 1984.

[4] M. Sankiewicz, A. Kaczmarek and G. Budzyński, *Acoustic investigation of the carillons in Poland*, Archives of Acoustics, **19**, 3, 333–353, 1994.

[5] M. Sankiewicz and G. Budzyński, *Analysis of dissonances in carillon chords*, 100th AES Convention, Copenhagen, Preprint 4172, 1996.

[6] M. Sankiewicz and G. Budzyński, *Peculiarities in swinging bell sounds*, 101st AES Convention, Los Angeles, Preprint 4336, 1996.

[7] G. Szychliński, *Zegary wieżowe — The tower clocks*, Muzeum Historii Miasta Gdańska, 1999.

ARCHIVES OF ACOUSTICS
**25**, 2, 157–174 (2000)

# ANALYSIS OF A RESONATOR WITH A DIRECTIONAL ULTRASONIC VIBRATION CONVERTER OF R–L TYPE USING THE FINITE ELEMENTS METHOD

T. GUDRA

Wrocław University of Technology
Institute of Telecommunication and Acoustics
(50-370 Wrocław, Wybrzeże Wyspiańskiego 27, Poland)
e-mail: gudra@zakus.ita.pwr.wroc.pl

Some results of the analysis of the R–L type resonator with directional converter using the finite elements method (FEM) are presented in the paper. Three types of resonator tuning result from the analysis and they can be used for converters of other type. The modal patterns in anti-phase and in-phase vibration modes for all types of tuning are presented. The choice of particular tuning depends on the way of using the converter. The modulus of the relation between the surface displacement amplitude for a longitudinal vibrating resonator and the side displacement amplitude for a radial vibrating resonator can be interpreted as the gain coefficient of converter's vibration amplitude. Moreover the influence of rode and disk resonator dimensions on proper frequencies of the converter vibration is described.

**Keywords:** resonator, directional converter, ultrasonic vibration.

## 1. Introduction

In ultrasonic technology piezomagnetic and piezoelectric transducers are generally applied to obtain high amplitude vibrations. The maximum value of vibration amplitude are limited by the magnetostrictic effect of nonlinearity for a piezomagnetic transducer and by the low mechanical strength of piezoceramic material for a piezoelectric transducer. One method of increasing the vibration amplitude upper limit consists in the use of a radiating source of special design, proposed by K. Itoh and E. Mori [3–6, 8, 9]. Four resonator types with a directional converter have been proposed by those authors: L–L type, L–L–L type, R–L type and L–R type (L — longitudinal, R — radial vibration). In these resonators the ultrasonic energy can be transmitted from the direction of driver to the other and can be concentrated or divided into plural loads from one vibration source.

The goal of this work was an investigation of the manner of the resonator with a directional converter of the R–L type. The finite elements method (FEM) was applied to analyse vibrations. This method enables the application of any dividing density for elements in the real elastic continuum, which allows us to observe local disturbance effects in any chosen fragments of the area; it is not easy to obtain by using the classical method. The latest literature concerning the usage of this type of resonators (including [12 – 15]) points to the fact that despite the time that has passed since their invention, they are still technologically attractive.

The goal of this work was also to verify the usefulness of the FEM for the design and optimization of this type of resonators.

## 2. Structure of the R–L type converter

The resonator with directional R – L conversion consists of a radial vibration disk and a longitudinal vibrating rod. The rod and the disk are coupled together at the velocity node of radial vibration for the disk and that of longitudinal vibration for the rod as shown in Fig. 1. With the suitable choice of dimensions, such a system permits comparatively large amplitudes of rod surface vibrations to be obtained. An energy transmission from the disk to the rod occurs due to the Poisson effect in the mechanically coupled common part of the converter. When the free vibration frequencies of individual resonators are different from each other, each of them vibrates as a free system, whereas when these frequencies are close to one another, there is an interaction between the two resonators.

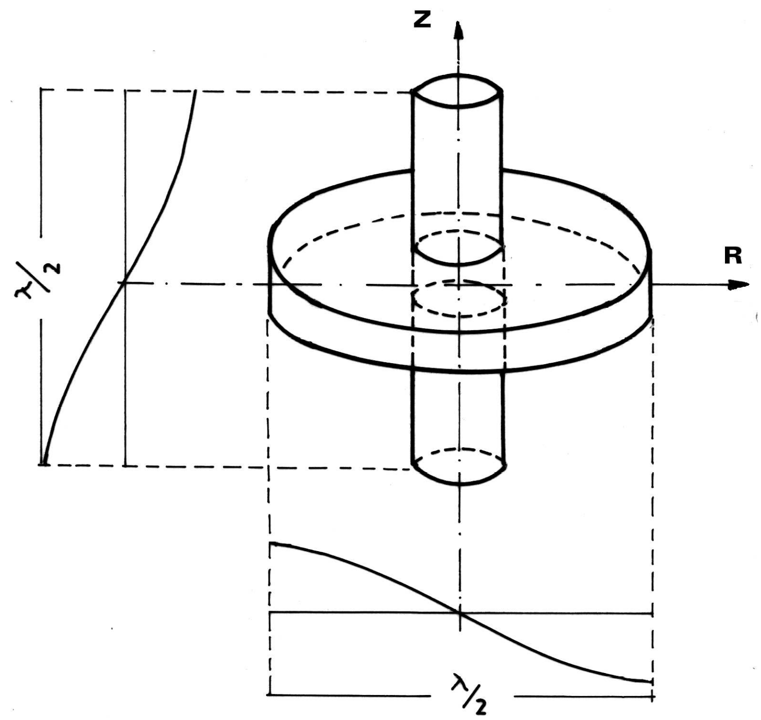


Fig. 1. Resonator with directional converter of the R – L type.

This system has two resonance frequencies depending on the vibration phase of the rod and the disk. In-phase vibrations occur when the ends of the rod and the side surface of the disk vibrate in the phase, whereas for anti-phase vibrations end surfaces of the rod vibrate in the opposite phase in relation to the side surface of the disk.

The resonators with directional converters can be constructed as homogeneous and heterogeneous systems. The homogeneous converters may be excited to vibration by external ultrasonic transducers [11 – 15], in heterogeneous converters the resonator of longitudinal or radial vibration can be a properly vibrating piezoelectric [1, 2] or piezomagnetic [7] ultrasonic transducer.

## 3. Geometry of the system

The resonator with directional conversion of vibration of the R – L type is a system with an axial symmetric stresses distribution. From the mathematical point of view the problem is similar to the two-dimensional problem. Because of the symmetry of the system in each point of the cross-section led along the symmetry axis the displacement is defined by two components. If we mark the radial co-ordinate of the point with $R$ and the axial coordinate of the point with $Z$, $u$ and $v$ will be displacements related to these coordinates then we obtain the two-dimensional case. A chosen element, turning around the axis determines the volume with reference to which all calculations should be done.

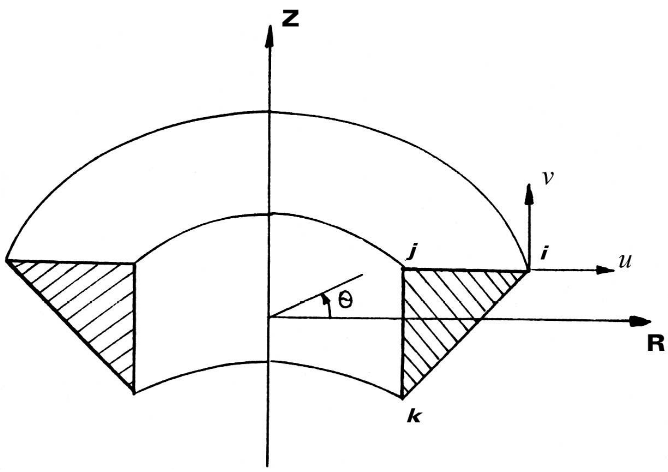


Fig. 2. Triangular ring shaped element.

For a triangular element, as shown in Fig. 2, the nodes are defined as $i$, $j$, $k$. The displacement $\delta$ of the $i$-node is defined by its two components:

$$\{\delta_i\} = \left\{ \begin{array}{c} u_i \\ v_i \end{array} \right\}, \tag{1}$$

so the displacement of an element is defined by the vector

$$\{\delta\}^e = \left\{ \begin{array}{c} \delta_i \\ \delta_j \\ \delta_k \end{array} \right\}. \tag{2}$$

Taking into account the relations characteristic of the FEM and solving the move equation for an elastic system [16] we can calculate free vibration frequencies of the system and node displacements of triangular elements the investigated resonator was divided into.

### 4. R–L type homogeneous converter

The R – L type homogeneous converter made of steel presented in Fig. 3 was subject to an analysis. Dimensions of this converter were such so as to be matched with experimental results obtained by other authors [3, 6].

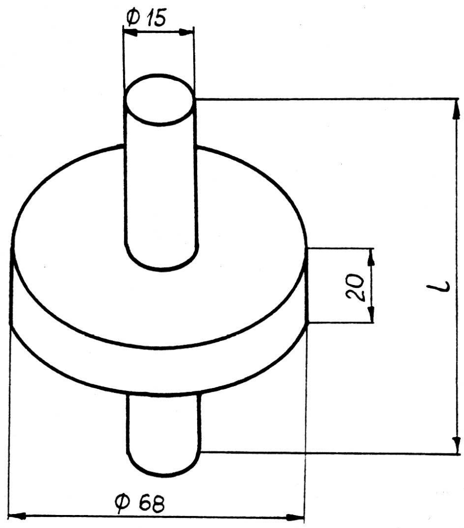


Fig. 3. Dimensions of homogeneous resonator with the R – L type conversion which are the grounds for analysis.

For calculations it has been assumed that the converter is made of steel whose material constants are:

$$\begin{aligned} E &= 0.206 \cdot 10^{12}\,[\mathrm{Pa}], \\ \nu &= 0.283, \\ \rho &= 7700\,[\mathrm{kg/m^3}], \end{aligned}$$

where $E$ — Young modulus, $\nu$ — Poisson's ratio, $\rho$ — density.

The division of the converter into elements is represented in Fig. 4. In consideration of the symmetry of the system, one fourth of the cross-sectional area was divided into 28 elements. The dependence of the converter's free vibration frequency on the length of a rod vibrating in the longitudinal mode is presented in Fig. 5. This dependence is illustrated by two curves corresponding to the frequencies of two modes of vibration: $f_s$ — frequency for the in-phase (synphase) mode, $f_a$ — frequency for the anti-phase mode.

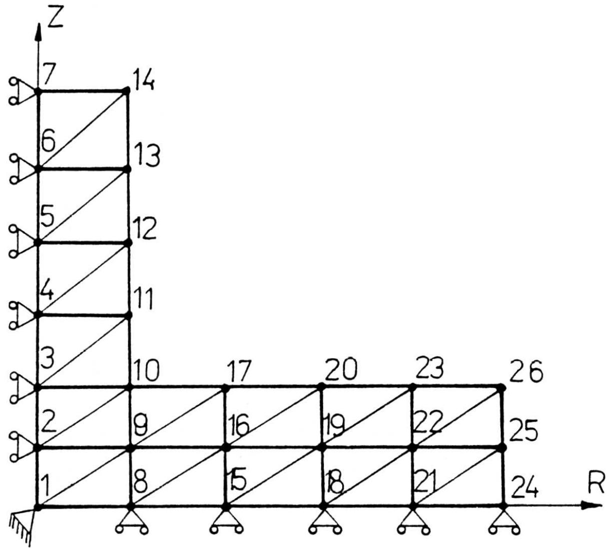


Fig. 4. Division of the R–L type converter into elements. Number of the elements – 28; Number of the nodes – 26; Number of movable degrees of freedom for direction $R$ – 5; Number of movable degrees of freedom for direction $Z$ – 6; Number of movable degrees of freedom for direction $R$ and $Z$ – 14; Number of immovable degrees of freedom – 1.

The distance between the curves for particular lengths of the rod resonator is related to the frequency difference $\Delta f = f_s - f_a$. The characteristic curve for $\Delta f = f(l_{\rm rod})$ is presented in Fig. 6.

Numbers on particular points on the curve in Fig. 5 are the calculated modules of the relation between the surface displacement amplitude for a longitudinal vibration resonator and the side horizontal displacement amplitude for a radial vibration resonator. This relation can be interpreted as the gain coefficient of converter's vibration amplitude. This is of a great practical value since it allows the application of this type of resonator to increase the amplitude of vibrations. For the minimum value of $(f_s - f_a)$ the value of this relation stays the same for both in-phase mode and anti-phase mode vibrations.

For $\min(f_s - f_a)$ we get

$$\left|\frac{\delta_{Z_7}}{\delta_{R_{24}}}\right|\Bigg|_{f_a} = \left|\frac{\delta_{Z_7}}{\delta_{R_{24}}}\right|\Bigg|_{f_s}, \tag{3}$$

where $\delta_{Z_7}$ — displacement of the node No 7 towards $Z$, $\delta_{R_{24}}$ — displacement of the node No 24 towards $R$.

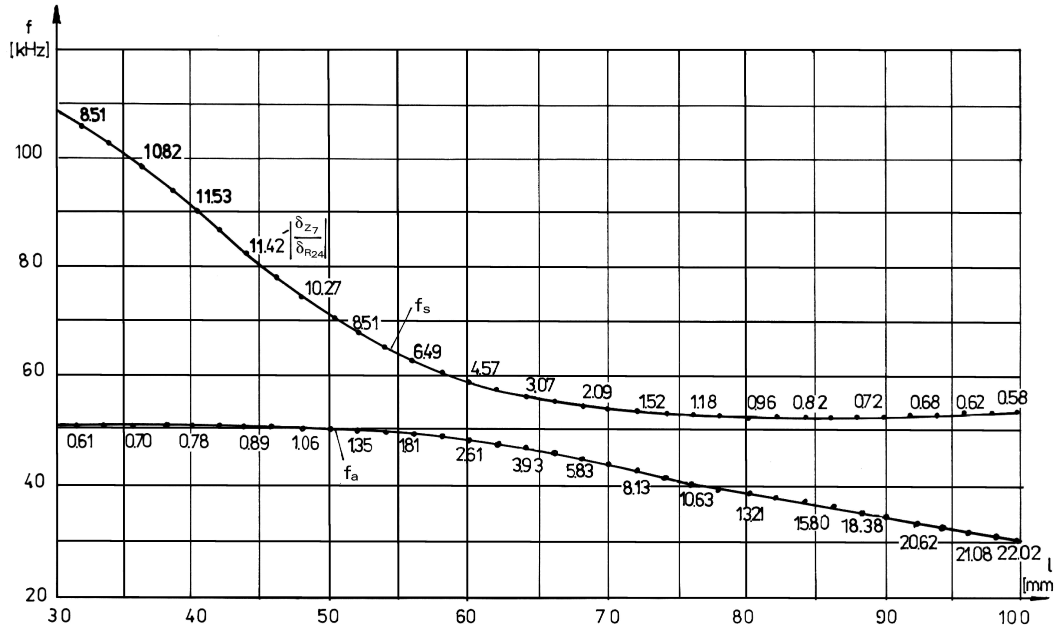


Fig. 5. The dependence of the R–L type converter's free vibration frequency on the length of the longitudinal resonator.

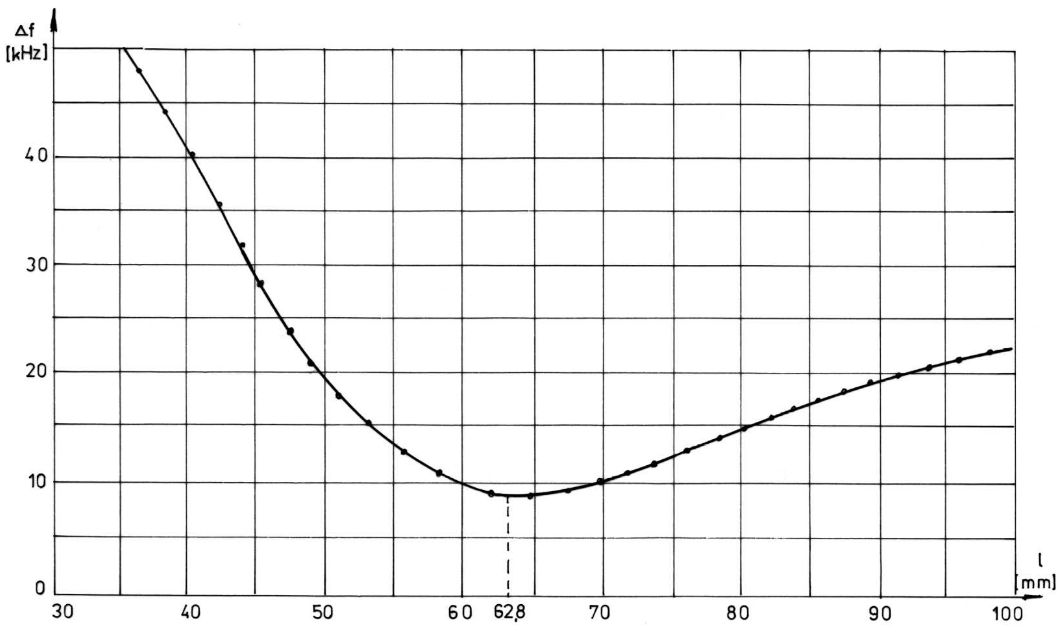


Fig. 6. The dependence of $\Delta f = f_s - f_a$ for the R–L type converter on the length of the rod resonator.

This is explained in a more detailed way in Fig. 7. where the relation $|\delta_{Z_7}/\delta_{R_{24}}| = f(l_{\mathrm{rod}})$ is presented for both modes of vibrations. For the same value of this relation (the point of intersection of both curves) the length of the rod resonator was determined with the assumption that this is one of the possible criteria of "tuning" the R–L type converter. This criterion can be written in a generalised form:

$$\left|\frac{\delta_{Z_{\mathrm{rod}}}}{\delta_{R_d}}\right|\Bigg|_{f_a} = \left|\frac{\delta_{Z_{\mathrm{rod}}}}{\delta_{R_d}}\right|\Bigg|_{f_s}, \tag{4}$$

where $\delta_{\mathrm{rod}}$ — the rod surface displacement towards $Z$, $\delta_{R_d}$ — the disk side horizontal displacement towards $R$.

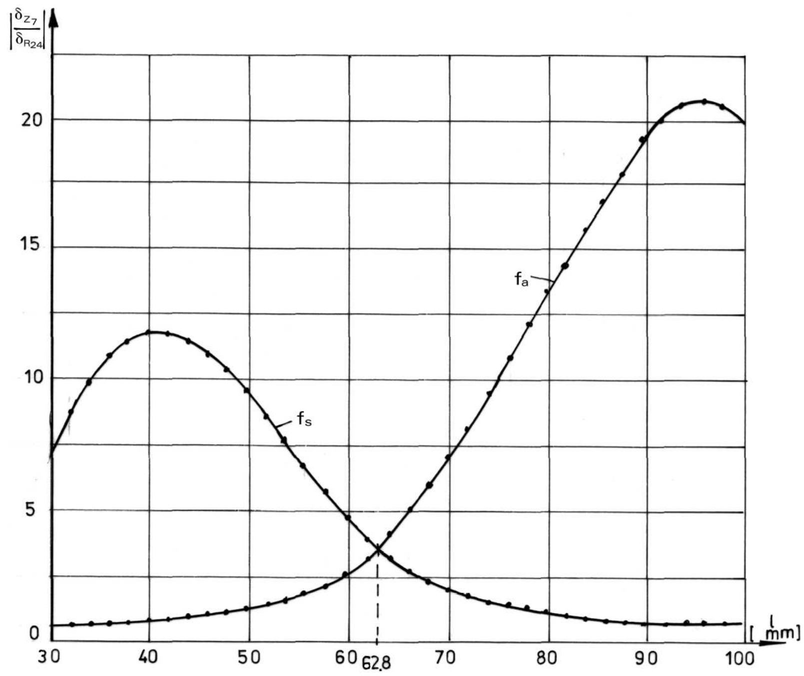


Fig. 7. Characteristic curve for the in-phase and the anti-phase vibration modes.

For such a "tuned" converter the displacements of particular nodes were determined which allowed us to obtain the form of vibrations both for anti-phase and in-phase vibration modes (Fig. 8).

In both figures the direction of vibrations of particular converter surfaces is marked by arrows. The calculated results obtained by means of FEM allow us to follow the way in which particular fragments of the resonator behave during vibrations. For the in-phase and the anti-phase vibration mode there exists a certain optimum length of the rod resonator at which the vibration amplitude gain coefficient $\delta_{Z_{\mathrm{rod}}}/\delta_{R_d}$ reaches its maximum. This is of great importance when designing such resonators since it allows us to define the optimum dimensions of the resonator at the preset frequency and the preset vibration

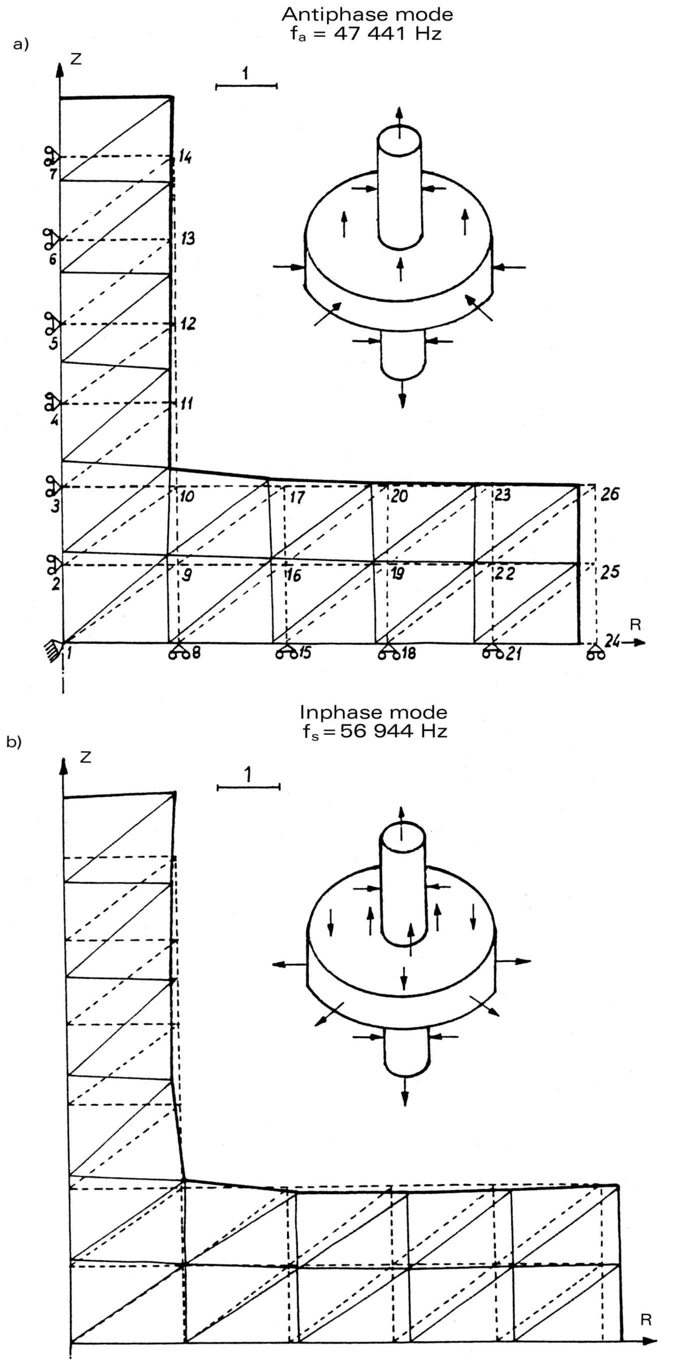


Fig. 8. Vibrations modes of homogeneous the R – L type converter: a) for the anti-phase mode of vibration, b) for the in-phase mode of vibration presented for the aligned converter in accordance with Eq. (3).

mode. Besides the criterion of tuning the R–L type converter (shown as (4)) another criterion can also be considered, i.e., the same value of the modulus representing the relation of surface displacement amplitude in a given direction to maximum displacement amplitude for particular vibration modes which can be written as

$$\left|\left|\frac{\delta_{Z_{\mathrm{rod}}}}{\delta_{R_{\max}}}\right|\right|_{f_a} = \left|\left|\frac{\delta_{Z_d}}{\delta_{R_{\max}}}\right|\right|_{f_a}, \tag{5}$$

and

$$\left|\left|\frac{\delta_{Z_{\mathrm{rod}}}}{\delta_{R_{\max}}}\right|\right|_{f_s} = \left|\left|\frac{\delta_{Z_d}}{\delta_{R_{\max}}}\right|\right|_{f_s}. \tag{6}$$

Figure 9 and 10 show vibration modes of the R–L type converter for such criteria of tuning. When comparing vibration modes in Figs. 9a, b and 10a, b one can easily notice

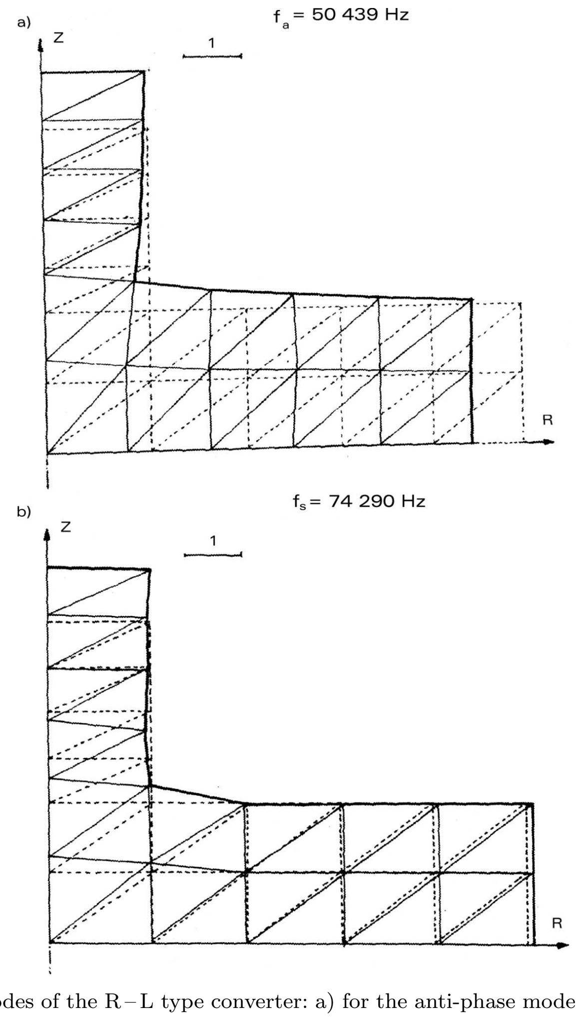


Fig. 9. Vibrations modes of the R–L type converter: a) for the anti-phase mode of vibration, b) for the in-phase mode of vibration presented for the aligned converter in accordance with Eq. (5).

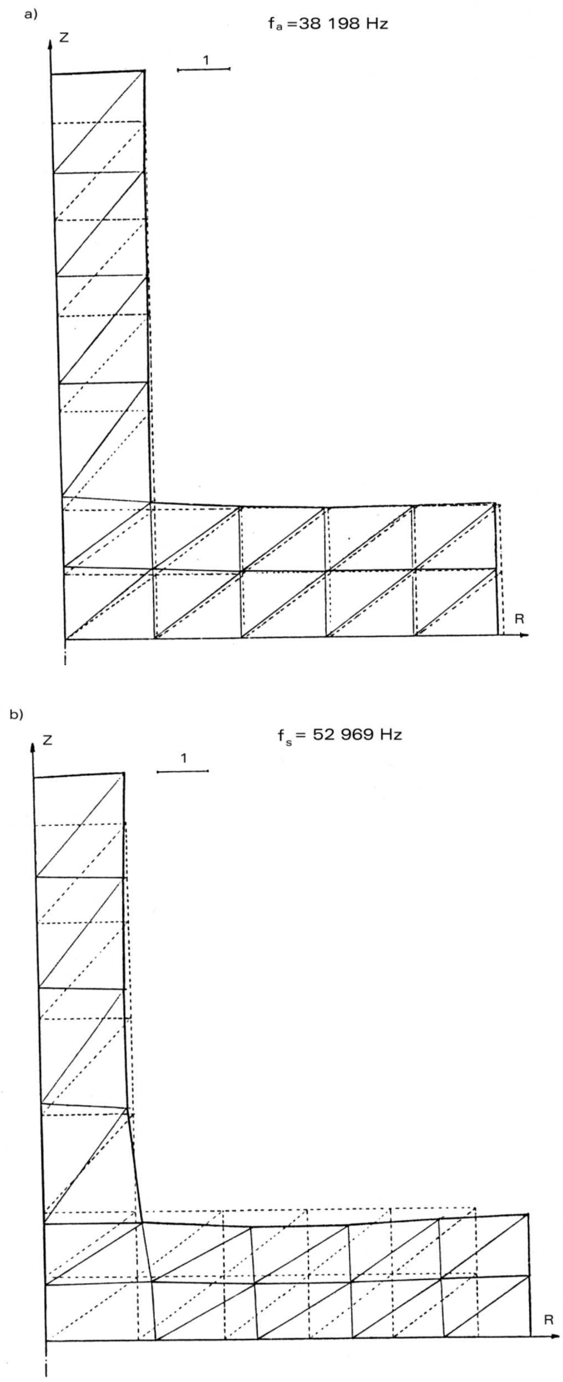


Fig. 10. Vibrations modes of the R – L type converter: a) for the anti-phase mode of vibration, b) for the in-phase mode of vibration presented for the aligned converter in accordance with Eq. (6).

that there is a considerable difference between the magnitude of displacement amplitudes of particular surfaces for both vibration modes at the pre-determined tuning criterion. Whereas the comparison of the obtained free vibration frequencies and the length of the rod resonator for vibration modes determined on the basis of all "tuning" criteria (Eqs. (4), (5), (6)) points to considerable discrepancies between these parameters (which is important in cascade-coupling of several converters).

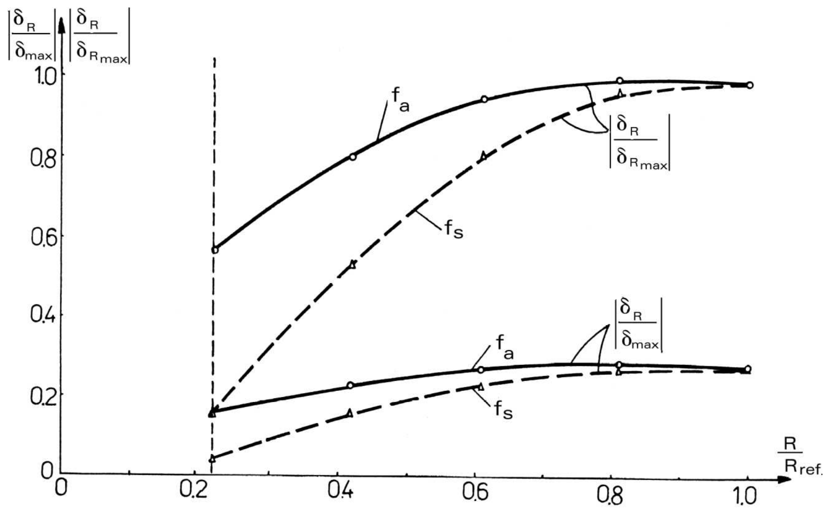


Fig. 11. Displacements distribution along the radius of the disk resonator presented for the aligned converter in accordance with Eq. (3).

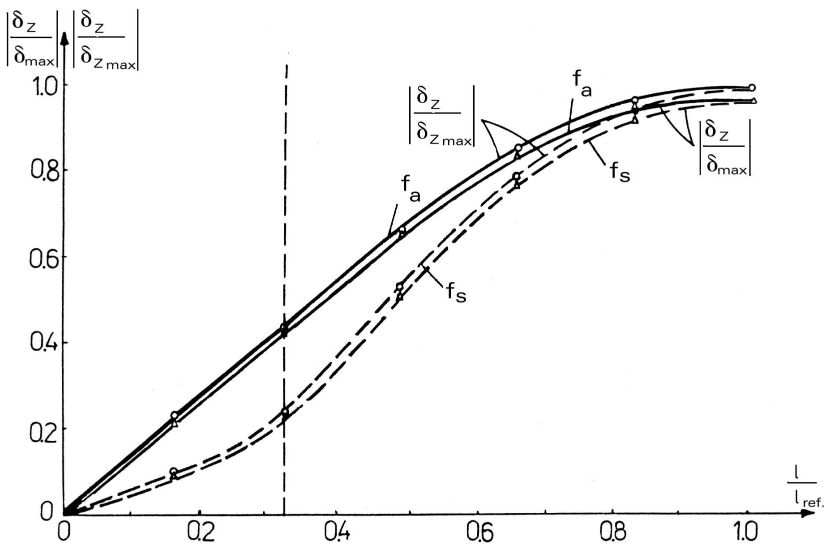


Fig. 12. Displacements distribution along the axis of the rod resonator presented for the aligned converter in accordance with Eq. (3).

Figures 11 and 12 present displacement distributions along the radius of the disk resonator and along the axis of the rod resonator for both vibration modes. For the anti-phase vibration mode the displacements are in each case bigger than for the in-phase mode.

Figures 13 and 14 show the distribution of displacements over the surface of resonators. What follows from both figures is that the displacements along the axis are bigger than those on the surface of particular resonators (for both vibration modes).

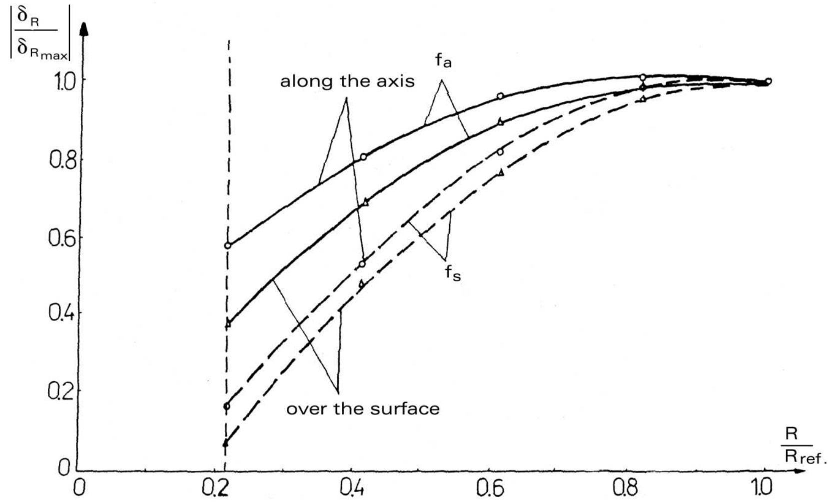


Fig. 13. Displacements distribution along the radius of the disk resonator over its surface and along its symmetry axis presented for the aligned converter in accordance with Eq. (3).

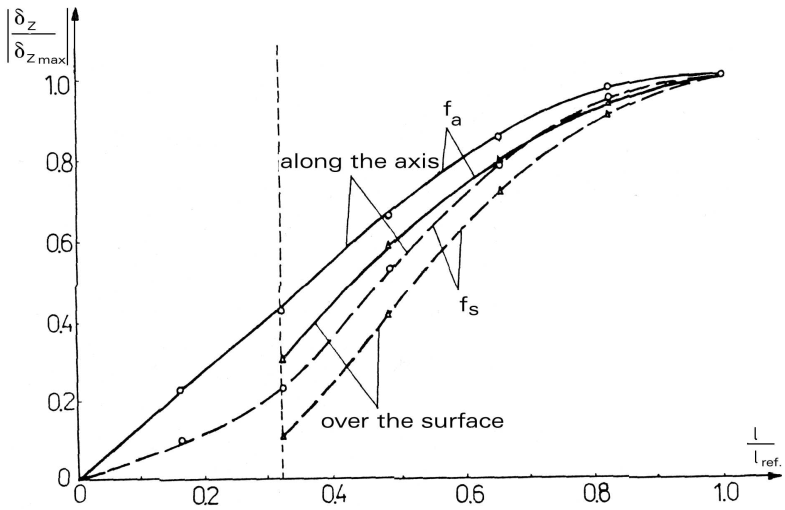


Fig. 14. Displacements distribution along the axis and over the surface of the rod resonator presented for an aligned converter in accordance Eq. (3).

## 5. R – L type heterogeneous converter

Finite elements methods also makes the analysis of resonators made from different materials possible. Figure 15 shows such an R – L type heterogeneous converter which was subject to analysis. The resonator of radial vibrations is a piezoelectric disk made of piezoceramic PXE-4 (PHILIPS). The resonator of longitudinal vibration is a titanium rod fixed in piezoceramic. The piezoelectric disk and the metal rod have been divided here into elements in the same way as the homogeneous converter. The following material constants were assumed for the calculation:

Titanium:

$$\begin{aligned} E &= 0.1157 \cdot 10^{12} [\mathrm{Pa}], \\ \nu &= 0.21, \\ \rho &= 4580\,[\mathrm{kg/m^3}]. \end{aligned}$$

Piezoceramic:

$$\begin{aligned} E &= 0.85 \cdot 10^{11}\,[\mathrm{Pa}], \\ \nu &= 0.3 \\ \delta &= 7500\,[\mathrm{kg/m^3}]. \end{aligned}$$

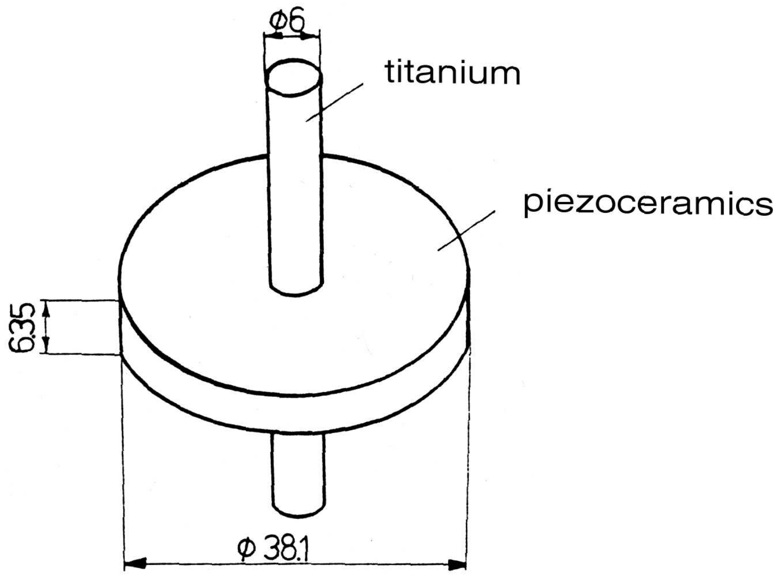


Fig. 15. The R – L type heterogeneous converter.

The analysis of this type of converter with the help of FEM yields characteristic curves and vibration modes similar those in a homogeneous converter. In view of similar character of the curves and vibration modes only some of the analysis results are presented here in Figs. 16, 17 and 18.

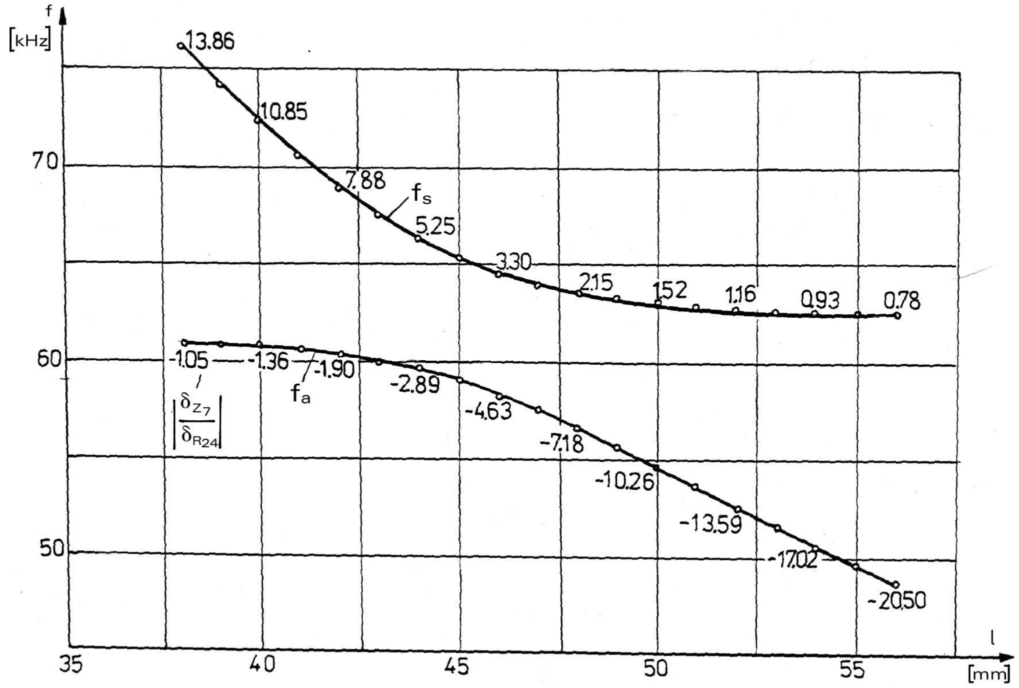


Fig. 16. The dependence of the R – L type heterogeneous converter's free vibration frequency on the length of the longitudinal resonator.

This resonator was experimentally tested by the author and described in [1, 2]. One characteristic of such a converter is its electrical input admittance. An example of a graph of the admittance modulus is presented in Fig. 19. The maxima of this graph correspond to free vibration frequencies of the converter presented in Fig. 17. The frequency spacing depends on the dimensions of the part common for both resonators and is longer the bigger the dimensions are [10]. The maximal values of the modulus of the electrical admittance of the converter depend on the resonator length and are equal for an aligned converter. Other results of investigations of this converter are described in [1, 2]. This construction has already been put into practice.

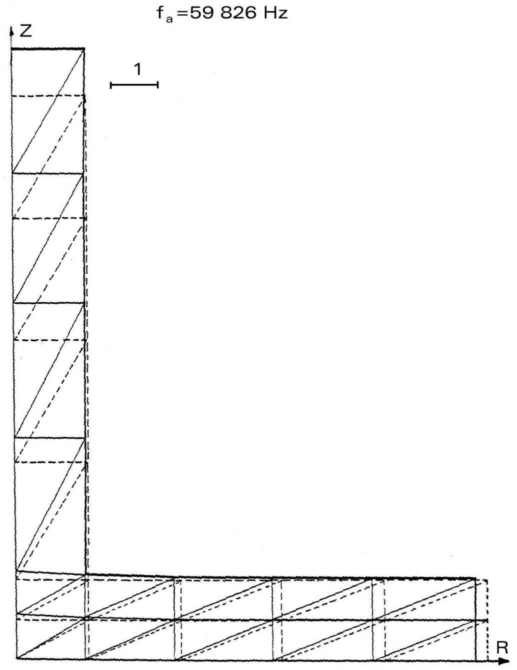


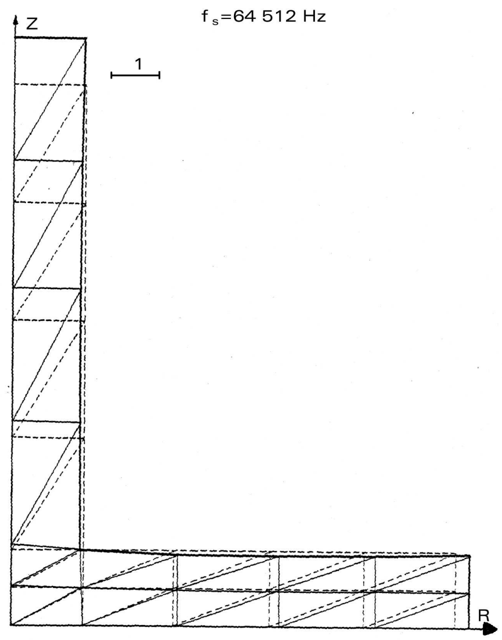


Fig. 17. Vibrations modes of the R–L type heteerogeneous converter: a) for the anti-phase mode of vibration, b) for the in-phase mode of vibration.

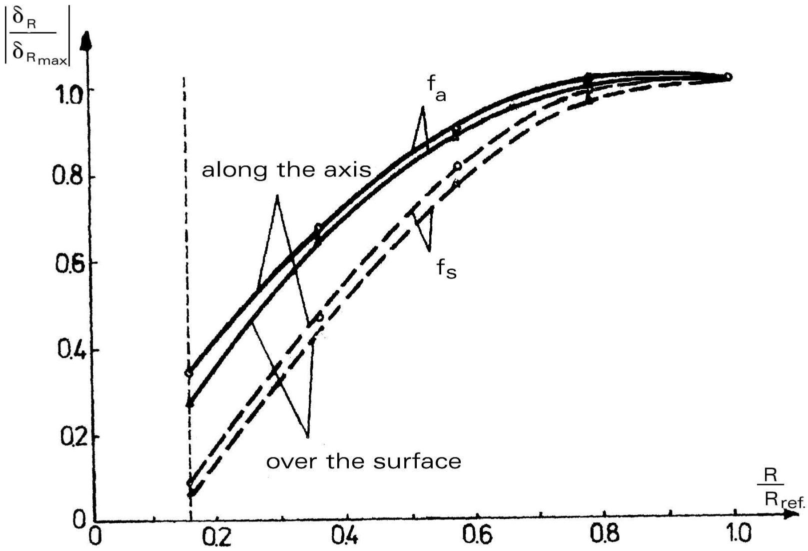


Fig. 18. Displacements distribution along the radius of the disk resonator, over its surface and along its symmetry axis for the aligned converter in accordance with Eq. (3).

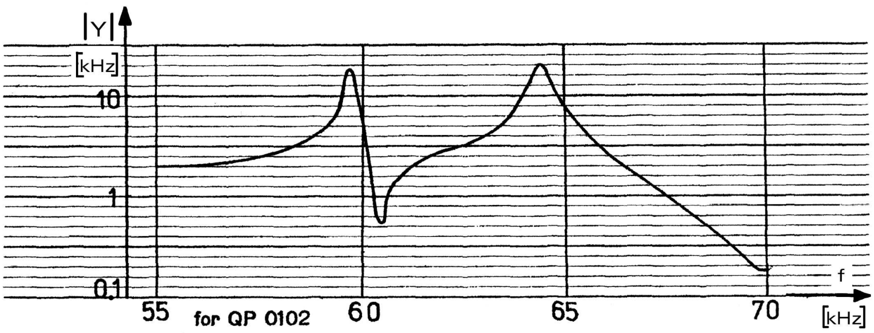


Fig. 19. The modulus of electrical admittance for the heterogeneous converter presented in Fig. 15.

## 6. Conclusions

The obtained results are, in part, compatible with those cited in works of K. Itoh and E. Mori [3, 6]. The authors, when experimenting on a homogeneous converter made of steel S45c (Japanese designation) with dimensions:

- Ø of the rod = 15 mm,
- length of the rod = 52.4 mm,
- Ø of the disk = 68 mm,
- thickness of the disk = 20 mm.

Obtained high free vibration frequencies corresponding to the anti-phase vibration mode $f_a = 50.235$ Hz and to the in-phase vibration mode $f_s = 60.4873$ Hz, result in $\Delta f = f_s - f_a = 10.252$ Hz.

The results obtained with the help of FEM point to the fact that the length of the rod was not optimum and did not allow us to obtain a converter which would be "tuned" according to any of the criteria suggested here. The most approximate result corresponds to the type of tuning in accordance with Eq. (4), for which:

- Ø of the rod = 15 mm,
- length of the rod = 62.8 mm,
- Ø of the disk = 68 mm,
- thickness of the disk = 20 mm,
- $f_a = 47.441$ Hz,
- $f_s = 56.944$ Hz,
- $\Delta = 9.505$ Hz.

Unconformity material constants may have a certain effect on the discrepancy between results presented in [3] and those obtained by means of FEM.

The three types of tuning (Eqs. (4) – (6)) postulated in this paper allow us to apply this type of resonators on large scale. Special attention should be paid to the possibility of using the converters for increasing the vibration amplitude. With the help of FEM it is possible to find the magnitude of this gain with preset input parameters as well as to determine the converter free vibration frequency at which the maximum gain for given resonator dimensions occurs.

The results obtained with the help of the FEM for the R – L type heterogeneous converter correspond to the results obtained from an experimental investigation of this converter.

## References

[1] J. Golanowski and T. Gudra, *Experimental study on resonators with directional converter* [in Polish], Proc. of XXIII Open Seminar on Acoustics, Wisła 1975, 116–117.

[2] J. Golanowski and T. Gudra, *Ultrasonic transducers using radial vibrations of a piezoelectric disc*, Archives of Acoustics, **4**, 3, 245–255 (1979).

[3] K. Itoh and E. Mori, *Experimental study on directional converters of ultrasonic vibration*, Seventh International Congress on Acoustics, Budapest 1971, 641–644.

[4] K. Itoh and E. Mori, *Study on resonator with directional converter (L–L type converter)*, J. Acoustic. Soc. Japan, **28**, 3, 127–135 (1972).

[5] K. Itoh and E. Mori, *Studies on resonator with directional converter (L–L–L type converter)*, J. Acoustic. Soc. Japan, **29**, 1, 28–36 (1973).

[6] K. Itoh and E. Mori, *Study on resonator with directional converter (R–L type converter)*, J. Acoustic. Soc. Japan, **29**, 5, 307–314 (1973).

[7] G.F. Lvovskaya, *Teoreticheskoe issledovaniye characteristik diskosterzhnevogo ultrazvukovogo instrumenta*, Akusticheskii Zhurnal, **22**, 4, 552–557 (1976).

[8] E. Mori and K. Itoh, *The investigation of resonator with directional converter*, The 6-th International Congress on Acoustics, Tokyo 1968, K 89–92.

[9] Y. Morihiro and E. Mori, *Elastic vibration mode converter for ultrasonic power application*, Seventh International Congress on Acoustics, Budapest 1971, 25 U8, 645–648.

[10] G.F. Povolockaya, *Teoreticheskoe issledovaniye instrumentov s preobrazovaniyem napravleniya kolebanii*, Akusticheskii Zhurnal, 20, 1, 87–94 (1974).

[11] G.F. Povolockaya, *Razchet dvuhstierzhnevogo ultrazvukovogo instrumenta rabotayushchego s maloy nagruskoy*, Akusticheskii Zhurnal, **21**, 4, 598–604 (1975).

[12] J. Tsujino and K. Hasegawa, *Ultrasonic wire bonding using high frequency 330, 600 kHz and complex vibration 190 kHz welding system*, Ultrasonics, **34**, 223–228 (1996).

[13] J. Tsujino, T. Ueoka, K. Hasegawa, Y. Fujita, T. Shiraki, T. Okada and T. Tamura, *New methods of ultrasonic welding of metal and plastics materials*, Ultrasonics, **34**, 177–185 (1996).

[14] J. Tsujino, H. Yoshihara, K. Kamimoto and Y. Osada, *Welding characteristics of ultrasonic wire bonding using high frequency and complex vibration locus*, Proc. of World Congress on Acoustics, Yokohama 1997, pp. 156–157.

[15] J. Tsujino, H. Yoshihara, K. Kamimoto and Y. Osada, *Welding characteristics and temperature rise of high frequency and complex vibration ultrasonic wire bonding*, Ultrasonics, **36**, 56–59 (1998).

[16] O.C. Zienkiewicz, *Finite elements method*, Mc Graw Hill Company Limited, UK 1977.

ARCHIVES OF ACOUSTICS
**25**, 2, 175–190 (2000)

# THE INFLUENCE OF ACOUSTIC NONLINEARITY ON ABSORPTION PROPERTIES OF HELMHOLTZ RESONATORS
# PART II. EXPERIMENT

M. MEISSNER

Polish Academy of Sciences
Institute of Fundamental Technological Research
(00-049 Warszawa, Świętokrzyska 21, Poland)
e-mail: mmeissn@ippt.gov.pl

An experimental study of an effect of the acoustic nonlinearity on absorption properties of Helmholtz resonators is presented in this work. By use of the classical standing wave method the changes in the absorption coefficient and the resonators impedance were investigated at moderate and high amplitudes of incident wave. As a result of nonlinearity a high absorption at resonance frequencies was observed and then a decrease in this absorption with increasing amplitude. Measurements of the total loss resistance of resonators have indicated that a change in the resistance at high amplitudes depends strongly on resonator orifice area, the smaller area — the higher increase in the resistance. The experimental results have also shown a growth in resonators reactance which causes an increase in resonance frequency. Quite a good agreement between experimental data and the theory presented in Part I was found.

## 1. Introduction

Helmholtz resonators have been studied extensively, primarily due to their use in a large number of practical applications. They are effective in a narrow frequency range centered by a resonance frequency and are therefore used to absorb sound at selected frequencies, e.g. in enclosed spaces [1], aircraft cabins [2] and panel systems [3, 4]. In order to develop a rational design procedure for the resonators it is important to investigate their acoustic properties in a wide range of sound intensities.

The case of high intensity sound is of special interest, when a resonator absorption depends on the amplitude of driving pressure due to nonlinear behaviour of orifice impedance. The change in absorption properties of Helmholtz resonators has the following physical explanation. At high amplitudes of excitation, there is a strong acoustic motion through the resonator orifice. It results in a separation of boundary layer and a formation of vortex on the outflow side of the orifice. The vortex moves away from the orifice and due to the viscous action its kinetic energy is ultimately dissipated as heat. The part of acoustic energy, which was transferred to the vortical field, represents an additional energy loss to the resonant system.

In the past a number of workers have studied the acoustic properties of Helmholtz resonators at a high intensity sound. INGARD [5] and BIES and WILSON [6] reported measurements of real and imaginary part of the orifice impedance, while WU and RUDNICK [7] presented experimental data showing a variation in a resonance frequency with increasing sound intensity. CZARNECKI [8, 9] investigated an influence of the nonlinear properties of Helmholtz resonators on acoustic conditions in enclosures. He found an increase or a decrease in the absorption coefficients depending on the conditions of the resonator surroundings.

A purpose of the second of two companion papers is a comparison between results of measurements of acoustic properties of Helmholtz resonators at moderate and high amplitudes, and theory presented in Part I [10]. The experiments were performed by using the standing wave apparatus with cylindrical tube which had a diameter $2a$ (Fig. 1). The resonators placed at the end of this tube were terminated at one end, by a rigid plate with a centrally located circular orifice with a diameter of $2b$ and thickness $d$, while at the other end by a rigid wall. The resonators dimensions were much less compared with a length of the incident wave.

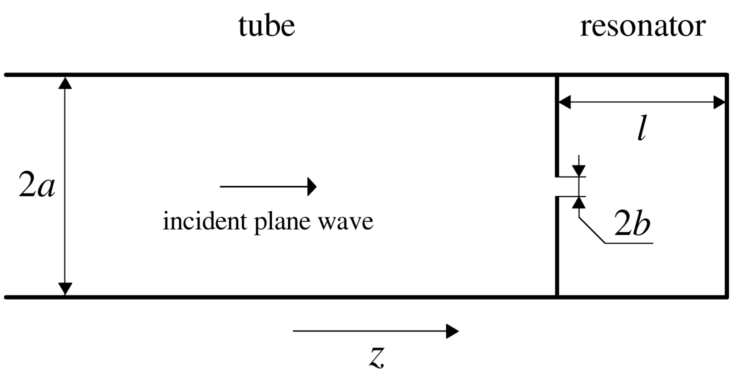


Fig. 1. Helmholtz resonator placed on one end of a tube.

## 2. Theoretical background

The theory pertaining to the nonlinear absorption properties of Helmholtz resonators has been presented with full particulars in Part I [10]. It has shown that changes in absorption coefficient at high amplitudes are associated with losses resulting from the conversion of the acoustic energy into the vortical energy. In the impedance model of resonator these losses were described by the nonlinear orifice resistance $R_n$ given by the expression

$$R_n = \frac{\rho V_0}{2.46\,\pi b^2}\left(\frac{1}{C_c} - \frac{b^2}{a^2}\right)^2, \tag{1}$$

where $V_0$ is the amplitude of a fundamental component of orifice velocity and $C_c$ is the contraction coefficient which is approximately equal to 0.61 in the case of sharp-edged orifice. Due to the fact that resistance $R_n$ is proportional to the velocity amplitude, the losses associated with the transfer of the acoustic energy to the vortical field are dominant at very high amplitudes of a driving pressure. If, however, the amplitudes of the pressure are moderate, we must also include in the impedance model of resonator a resistance connected with a viscous damping inside the resonator orifice. According to INGARD [5], this resistance can be described by the following empirical formula

$$R_\mu = \frac{\sqrt{2\rho\mu\omega}}{\pi b^2}\left(2 + \frac{d}{b}\right), \tag{2}$$

where $\mu$ is the coefficient of viscosity, $\omega$ is the angular frequency of an incident wave and $d$ is the orifice thickness. Thus, the relation between the velocity amplitude $V_0$ and the amplitude $|\hat{P}_i|$ of the driving pressure can be written as

$$V_0 = \frac{2|\hat{P}_i|}{\pi b^2\sqrt{(R_r + R_t)^2 + X^2}}\,, \tag{3}$$

where $R_r = \rho c/(\pi a^2)$ is the radiation resistance, $R_t = R_n + R_\mu$ is the total loss resistance and $X$ is the reactance of the resonator.

The theoretical considerations in Part I have indicated that the reactance $X$ may vary as the amplitude of the driving pressure increases. This is a result of a jet contraction and a change in a co-vibrating mass on the outflow side of the resonator orifice. The variation in $X$ has not any influence on the absorption coefficient of resonators and only causes a shift in the resonance frequency, then, due to the lack of an accurate formula for the reactance $X$ at high amplitudes, we decide to use in calculations the expression for $X$ derived from the linear theory

$$X = \frac{\rho c}{\pi a^2}\cot(kl) - k\frac{\rho c}{\pi b^2}(d + \varDelta d), \qquad \varDelta d = \sum_{n=1}^{\infty}\frac{8aJ_1^2(\gamma_{0n}b/a)}{\gamma_{0n}^3 J_0^2(\gamma_{0n})}\,. \tag{4}$$

where $\varDelta d$ is the total end correction for a typical resonator geometry, in which the ratio $l/a$ is not too small ($l/a \geq 1/2$), and $\gamma_{0n}$ is the $n$-th root of the equation $dJ_0(\gamma)/d\gamma = 0$.

### *2.1. Measurement and calculation of absorption coefficient and impedance of resonator*

The modulus of the pressure inside the tube in a far field area, according to Part I, is given by

$$|\hat{P}_t| = |\hat{P}_i|\sqrt{1 + \beta^2 + 2\beta\cos(2kz - \chi)}\,, \qquad z \leq 0, \tag{5}$$

where $\beta$ and $\chi$ represent a modulus and a phase of complex reflection coefficient

$$\hat{\beta} = \beta e^{j\chi} = 1 - \frac{2R_r}{R_r + R_t + jX}\,. \tag{6}$$

The expression for the absorption coefficient $\alpha$, derived from Eqs. (5) and (6), has a form

$$\alpha = \frac{4|\hat{P}_t|_{\min}|\hat{P}_t|_{\max}}{\left[|\hat{P}_t|_{\min} + |\hat{P}_t|_{\max}\right]^2} = \frac{4R_rR_t}{(R_r + R_t)^2 + X^2}\,. \tag{7}$$

The first part of Eq. (7) enables to determine $\alpha$ by measurements of minimum and maximum values of standing wave pressure inside the tube, while the second part of it with Eqs. (1)–(4) makes possible a numerical calculation of absorption coefficient (Eq. (3) represents an implicit function of $V_0$).

An expression for the experimental determination of an impedance of resonator may be easily obtained from Eq. (6). After rearrangement, one can write this equation as

$$R_t + jX = R_r(1+\hat{\beta})/(1-\hat{\beta}). \tag{8}$$

If $L$ denotes a distance along $z$-axis from the first nodal point inside the tube to the orifice plate, then it results from Eq. (5) that

$$\chi = -2kL - \pi\,. \tag{9}$$

Putting Eq. (9) into Eq. (8) gives finally

$$R_t/R_r \;=\; \frac{1-\beta^2}{1+\beta^2+2\beta\cos(2kL)}\,, \tag{10}$$

$$X/R_r \;=\; \frac{2\beta\sin(2kL)}{1+\beta^2+2\beta\cos(2kL)}\,. \tag{11}$$

### *2.2. Experimental prediction of velocity amplitude in resonator orifice*

It has been shown in Part I that a pressure in the resonator cavity is uniform in a small distance from the orifice plane, because it represents a superposition of multiple plane wave reflections. The formula for the pressure $\hat{P}_l$ on the rigid plate closing the resonator cavity is thus given by

$$\hat{P}_l(t) = \rho\frac{\partial}{\partial t}\int\limits_0^{2\pi}\int\limits_0^{b} V_0 e^{-j\omega t} g_c(z_0=0,\ z=l)\, r_0 dr_0 d\phi_0\,, \tag{12}$$

where $(r_0, \phi_0, z_0)$ is a position of the source point in the cylindrical coordinates and $g_c(z, z_0)$ represents Green's function for the plane wave motion inside the resonator cavity

$$g_c(z,z_0) = -\frac{\cos(kz_0)[\sin(kz)+\cos(kz)\cot(kl)]}{k\pi a^2}\,. \tag{13}$$

After substituting Eq. (13) into Eq. (12) and using the approach $\sin(kl) \approx kl$, which is valid at low frequencies, one can obtain

$$V_0 = \frac{2\pi a^2 fl}{\rho c^2 b^2}\,|\hat{P}_l|, \tag{14}$$

where $f = \omega/2\pi$ is the frequency of an incident wave. As can be seen, the use of Eq. (14) enables to predict the velocity amplitude $V_0$ by a measurement of the pressure amplitude $|\hat{P}_l|$ at the closed end of the resonator.

## 3. Experimental arrangement and apparatus

The tests were carried out by use of the measuring system consisting of a 4002 B&K tube 1 m long and a radius $a = 4.95$ cm, the PW-12 ZOPAN decade generator, the 2712 B&K power amplifier and the 2033 B&K narrowband spectrum analyser (Fig. 2). The 4002 standing wave apparatus permitted a plane wave shape, radiated by the loudspeaker over the frequency range 90 – 1800 Hz, to be obtained. The resonators located at the end of the tube had the form of a cylindrical chamber with the same radius $a$ as the tube and the length $l = 2.5$ cm. A sharp-edged circular orifice of resonators had the thickness $d = 2$ mm and the radius $b$ from 1 to 3.5 mm.

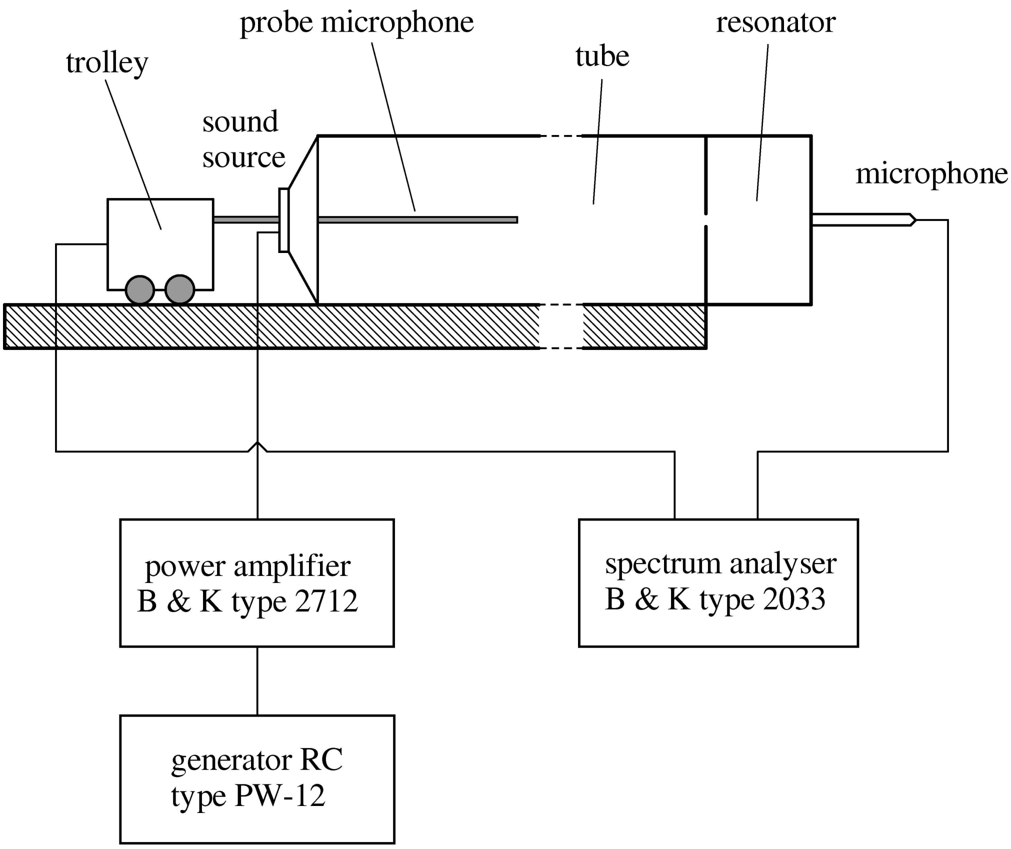


Fig. 2. Setup for measuring the absorption coefficient and impedance of resonator.

The first part of the tests contained measurements of the absorption coefficient $\alpha$ of resonators, in a range of frequencies comprising the fundamental resonance frequency $f_{\text{res}}$, at a constant amplitude $|\hat{P}_i|$ of driving pressure. This condition may be realized experimentally by putting $|\hat{P}_t|_{\min} + |\hat{P}_t|_{\max} = \text{const.}$, because as follows from Eq. (5)

$$|\hat{P}_i| = (|\hat{P}_t|_{\min} + |\hat{P}_t|_{\max})/2\,. \tag{15}$$

The aim of the tests was to investigate the changes of $\alpha$ in the range of moderate and high amplitudes of driving pressure ($|\hat{P}_i| = 0.11-20$ Pa) for resonators with the orifice radius $b = 1.5$, 2.5 and 3.5 mm, and a comparison between experimental and calculation results (Eqs. (1)–(4), (7)). In the second part of the tests, measurements of the total loss resistance $R_t$ and reactance $X$ of the resonator were made for a constant pressure amplitude $|\hat{P}_l|$. In order to measure $|\hat{P}_l|$ an additional slotted line was used with $1/8''$ B&K microphone mounted at the closed end of the resonator (Fig. 2). The purpose of the tests, carried out for resonators with the orifice radius $b = 1$, 1.5, 2, 2.5 and 3.5 mm, was to make a comparison between results of resistance $R_t$ calculations based on the pressure $|\hat{P}_i|$ of incident wave (Eqs. (1)–(4)) and pressure $|\hat{P}_l|$ at the closed end of resonator (Eqs. (1), (2), (14)).

## 4. Comparison between experimental and calculation results

### *4.1. Dependence of absorption coefficient $\alpha$ on pressure amplitude of incident wave*

The results of measurements are collected in Figs. 3–5, showing the influence of the pressure amplitude $|\hat{P}_i|$ on the absorption coefficient $\alpha$ in the frequency ranges comprising $f_{\mathrm{res}}$. It results from the experimental data that an effect of nonlinearity on coefficient $\alpha$ is the strongest one for the resonator with the orifice radius $b = 1.5$ mm. For the smallest amplitude of driving pressure, $|\hat{P}_i| = 0.11$ Pa, the coefficient $\alpha$ equals 0.85 at the resonance frequency $f_{\mathrm{res}} \approx 160$ Hz (Fig. 3a). It follows from the theoretical part that in this case the total loss resistance, being a sum of the velocity dependent nonlinear resistance $R_n$ and the viscous loss resistance $R_\mu$, is approximately twice as large as the radiation resistance $R_r$ (see Eq. (7)). At the amplitude $|\hat{P}_i|$ much bigger than 0.11 Pa the values of $\alpha$ fast decrease around the resonance frequency (Fig. 3b). It results from a growth in the velocity amplitude $V_0$ at the resonator orifice which involves an increase of losses due to nonlinearity. Finally, at the highest amplitude of driving pressure, $|\hat{P}_i| = 20$ Pa, the diminution of $\alpha$ takes place below the value of 0.3 in the whole frequency range (Fig. 3c).

A similar character of changes in the absorption coefficient $\alpha$ in the function of the pressure amplitude $|\hat{P}_i|$ has been obtained for the resonators with higher orifice radius. However, in these cases the effect of the driving pressure on the coefficient $\alpha$ is weaker than in the case $b = 1.5$ mm, because for the orifice radius $b = 2.5$, 3.5 mm and $|\hat{P}_i|$ from the range $0.11-20$ Pa the maximal values of $\alpha$ change from 0.99 to 0.58 (Fig. 4) and from 0.93 to 0.66 (Fig. 5). The weaker influence of $|\hat{P}_i|$ on the absorption coefficient at higher values of $b$ has a theoretical explanation. As can be seen from Eq. (1), it is a result of the inversely proportional dependence of the nonlinear resistance $R_n$ on the area of the orifice.

The best convergence between experimental and theoretical data can be observed in the case of small values of $|\hat{P}_i|$ when a dependence of $\alpha$ on the frequency $f$ is almost symmetrical around the resonance frequency. There is less agreement between measurements and calculations at the highest amplitude of driving pressure because of an irregularity of

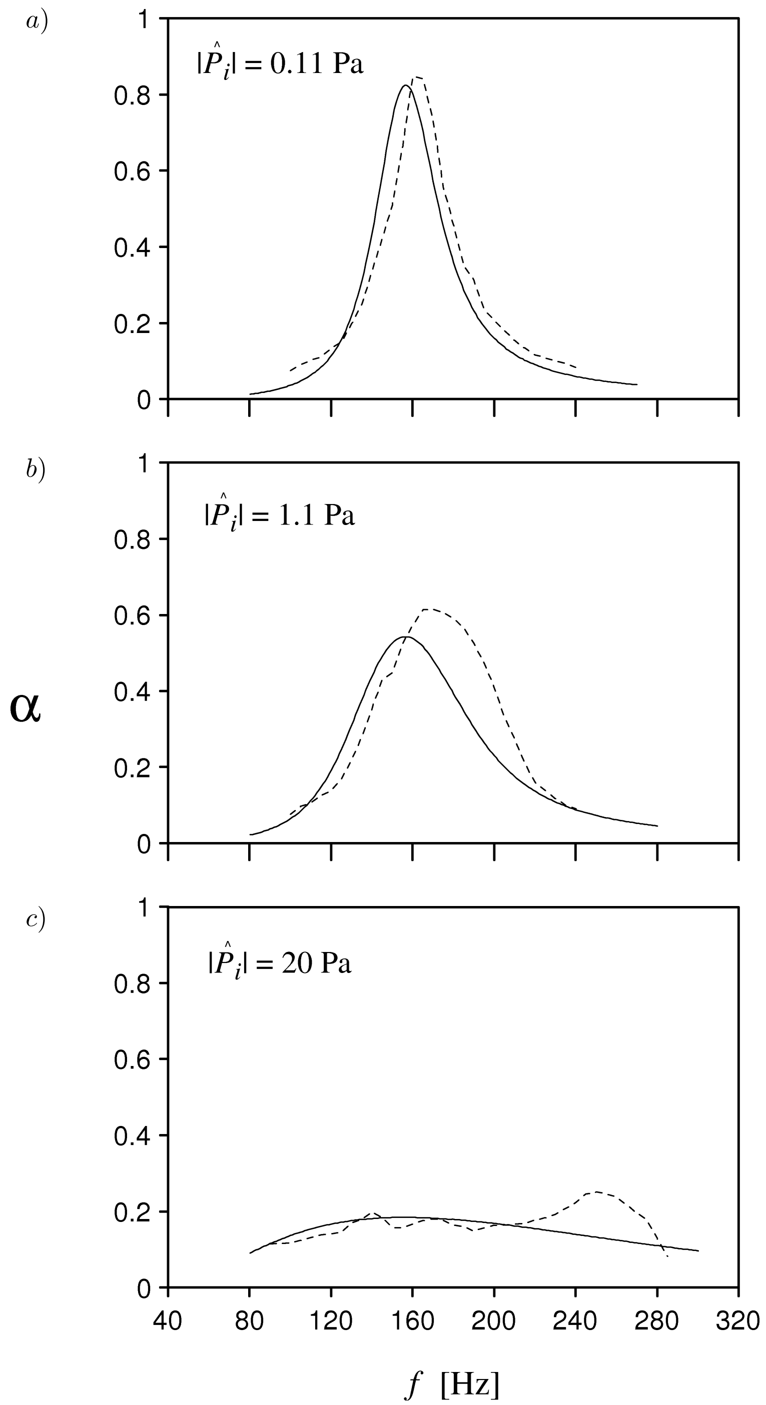


Fig. 3. Frequency dependence of the absorption coefficient $\alpha$ for resonator with orifice radius $b = 1.5$ mm at different pressure amplitudes $|\hat{P}_i|$ of incident plane wave; (- - - -) experiment, (—) calculation.

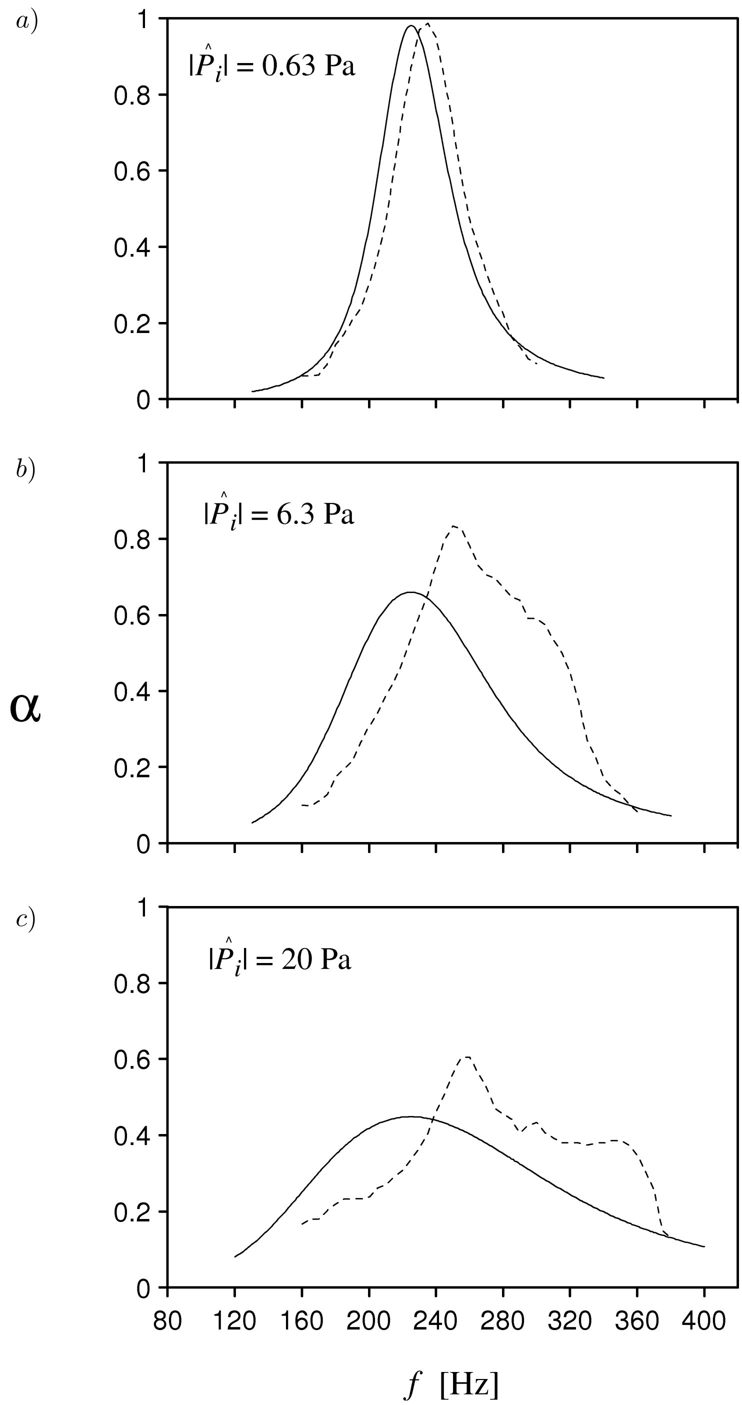


Fig. 4. Frequency dependence of the absorption coefficient $\alpha$ for resonator with orifice radius $b = 2.5$ mm at different pressure amplitudes $|\hat{P}_i|$ of incident plane wave; (- - - -) experiment, (—) calculation.

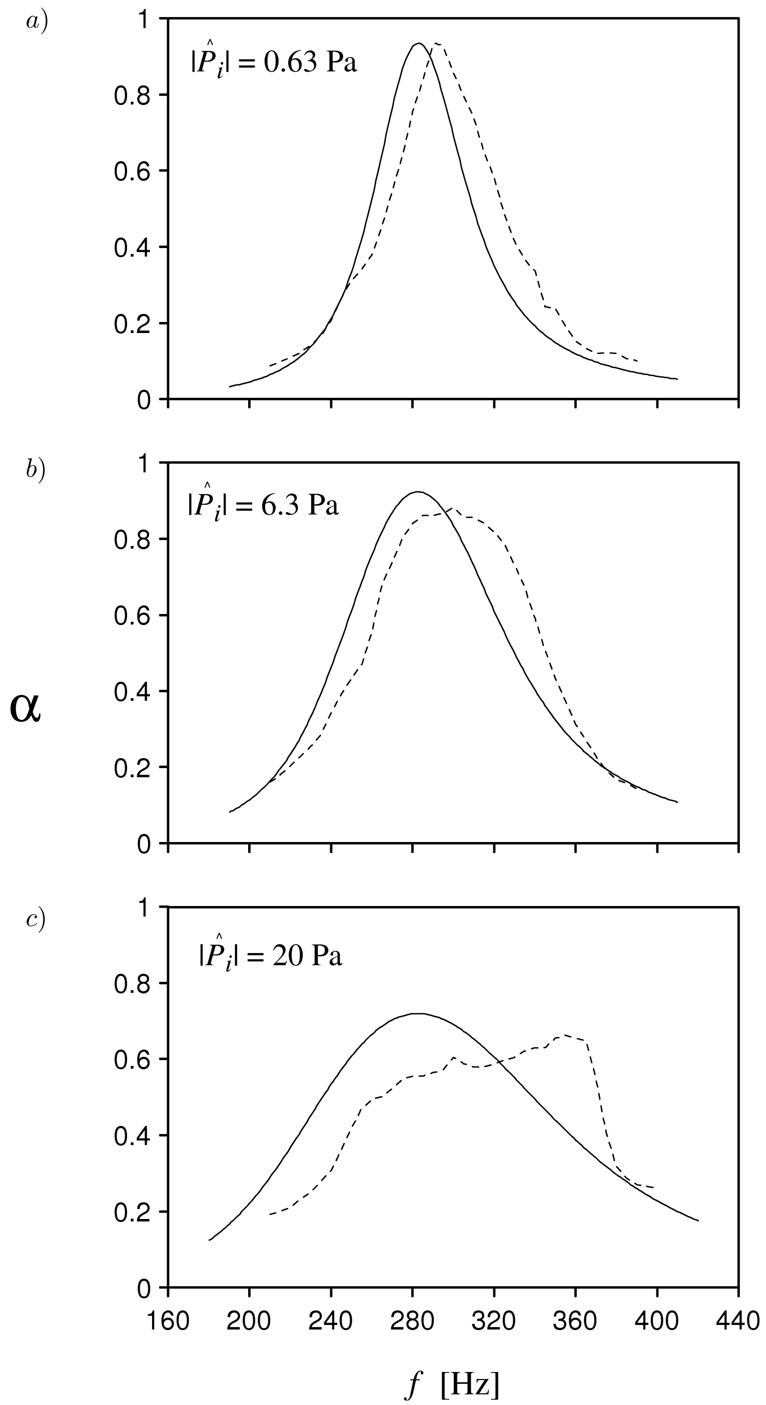


Fig. 5. Frequency dependence of the absorption coefficient $\alpha$ for resonator with orifice radius $b = 3.5$ mm at different pressure amplitudes $|\hat{P}_i|$ of incident plane wave; (- - - -) experiment, (—) calculation.

experimental data changes (Figs. 4b, 4c, 5c). This special dependence of $\alpha$ in the function of $f$ can be explained considering the measuring tube as an additional resonance system closed at one end by the resonator and at the other one by the loudspeakers. As a result of mutual interaction between a sound source and a resonator the changes in mechanical parameters of loudspeaker and acoustic properties of resonator take place [11]. This interaction is the most effective in the case of a high sound intensity and resonance in the tube. It can be clearly observed comparing curves in Figs. 4b, 4c, 5c and the plot in Fig. 6, which exhibits an acoustic response of the measuring tube closed by a rigid surface to the white noise. As may be seen, the local maxima of $\alpha$ occur near resonance frequencies of the tube.

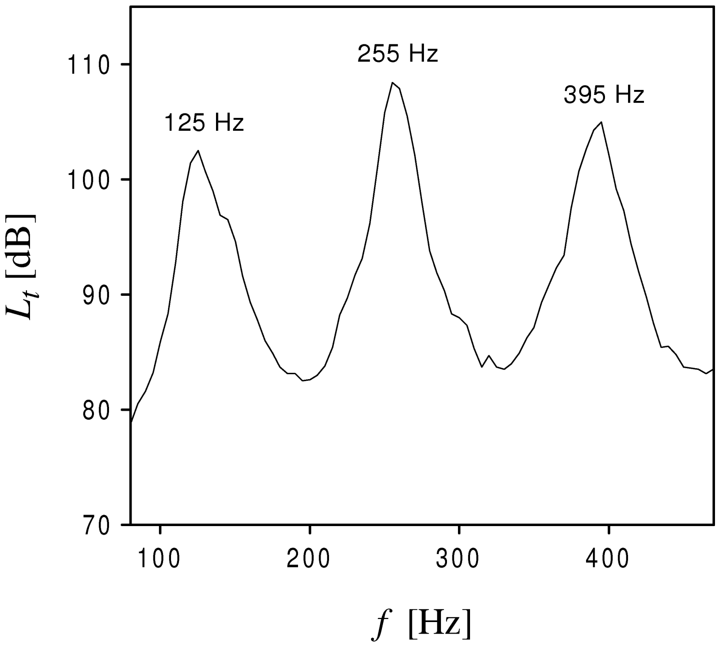


Fig. 6. Frequency dependence of sound pressure level $L_t$ inside the measuring tube closed by a rigid wall in the case of white noise excitation.

### *4.2. Dependence of resistance $R_t$ on pressure amplitude at closed end of resonator*

Equation (14) indicates that a relation between the ratio $V_0/f$ and the pressure $|\hat{P}_l|$ is directly proportional. From this formula and a definition of the total loss resistance the following relationship can be derived

$$\frac{R_t f_{\text{res}}}{R_r f} = \frac{R_\mu f_{\text{res}}}{R_r f} + \frac{\pi l f_{\text{res}} |\hat{P}_l|}{1.23 \rho c^3} \left( \frac{a^2}{b^2 C_c} - 1 \right)^2, \tag{16}$$

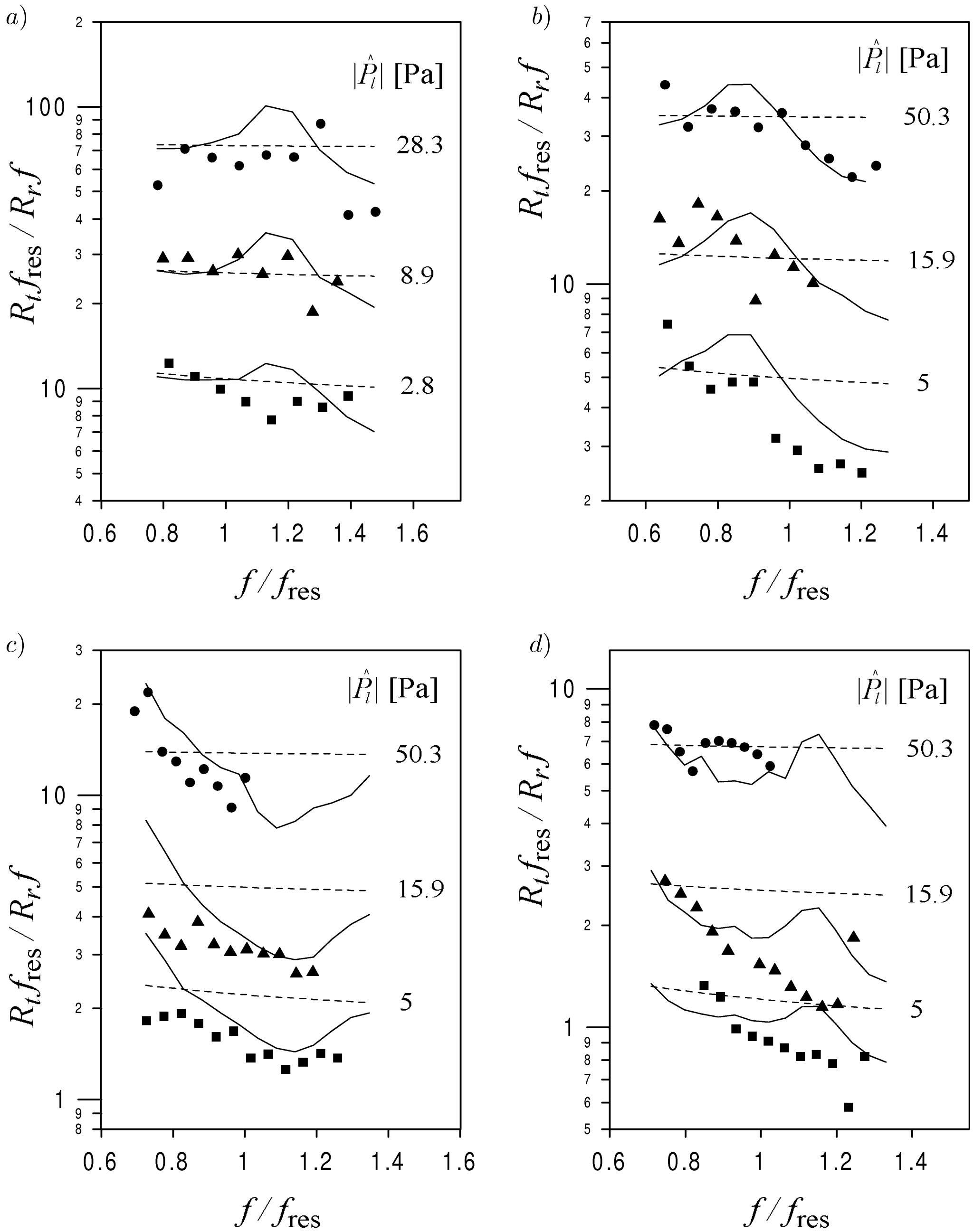


Fig. 7. Changes in $R_t f_{\mathrm{res}}/R_r f$ ratio versus nondimensional frequency $f/f_{\mathrm{res}}$ at different pressure amplitudes $|\hat{P}_l|$ for resonators with orifice radius $b$: a) 1 mm, b) 1.5 mm, c) 2 mm, d) 2.5 mm; circles, triangles and squares denote experimental data, (—) calculation results based on amplitude $|\hat{P}_i|$, (- - - -) calculation results based on amplitude $|\hat{P}_l|$.

therefore, in the high nonlinear regime ($R_n \gg R_\mu$) the quantity $R_t f_{\mathrm{res}}/R_r f$, for the given dimensions of resonator, approximately assumes the same values at the constant pressure amplitude $|\hat{P}_l|$. Figure 7 shows the experimentally and theoretically determined values of $R_t f_{\mathrm{res}}/R_r f$ in a function of nondimensional frequency $f/f_{\mathrm{res}}$ for the pressure $|\hat{P}_l|$ from the range $2.8-50.3$ Pa. The fundamental frequency $f_{\mathrm{res}}$ of the resonators was evaluated from experimental data or calculated from the condition $X = 0$. In this way, differences between the values of $f_{\mathrm{res}}$ obtained from measurements and theory were taken into account in the results presented in Fig. 7.

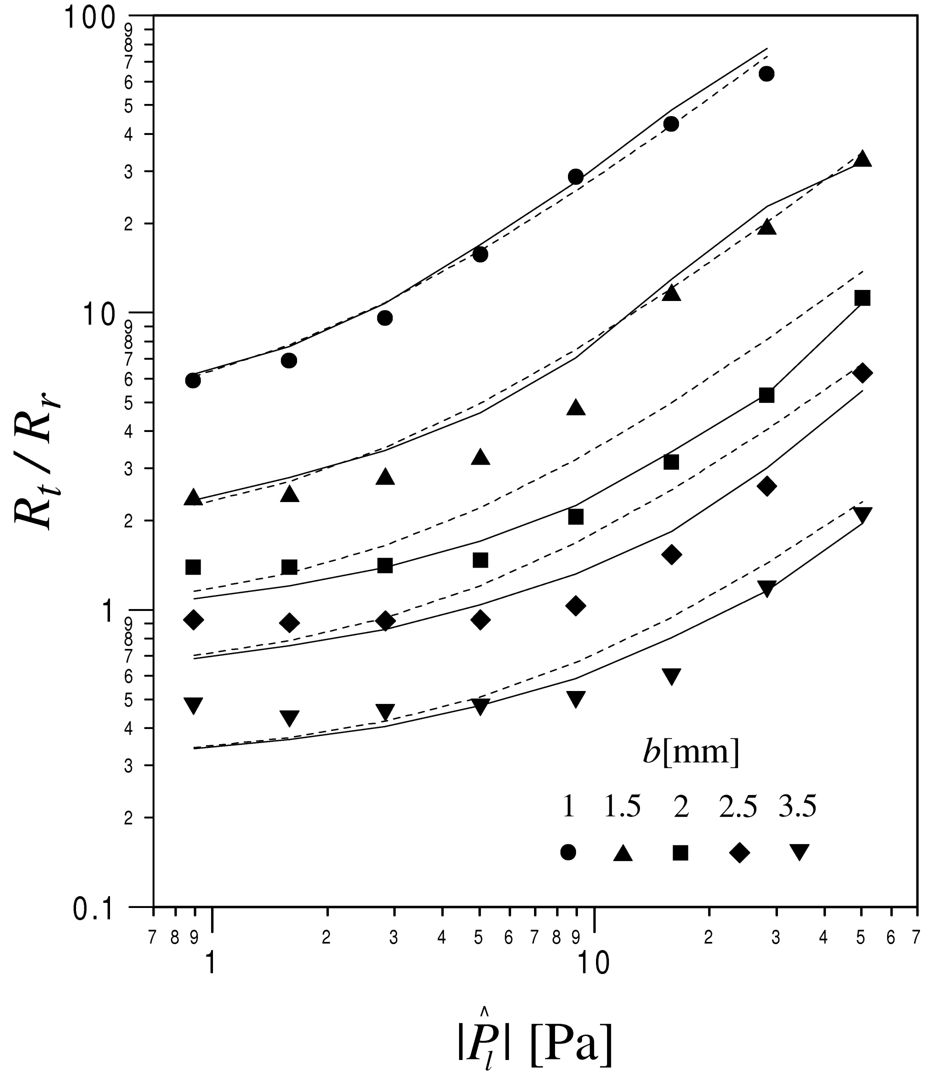


Fig. 8. Dependence of $R_t/R_r$ ratio at resonance frequency on pressure amplitude $|\hat{P}_l|$ for resonators with different orifice radius; (—) calculation results based on amplitude $|\hat{P}_i|$, (- - - -) calculation results based on amplitude $|\hat{P}_l|$.

As it was well predicted by theory, the nondimensional parameter $R_t f_{\mathrm{res}}/R_r f$ increases with the pressure amplitude and depends strongly on the orifice radius $b$. The relation between the quantity $R_t f_{\mathrm{res}}/R_r f$ and the orifice radius $b$, which results from experimental data, can be simply defined: a smaller value of $b$ — a higher value of $R_t f_{\mathrm{res}}/R_r f$ at the same amplitude $|\hat{P}_l|$. A more precise description of this dependence is possible in the case of resonance ($f/f_{\mathrm{res}} = 1$), when the agreement between measurements and data computed from Eq. (15) is satisfactory (in Fig. 7 indicated by dashed lines). For other values of $f/f_{\mathrm{res}}$, results of calculations based on the pressure amplitude $|\hat{P}_i|$ of incident wave (in Fig. 7 indicated by solid lines) approximate better the experimental data.

In order to illustrate a more general dependence between total resistance and pressure amplitude $|\hat{P}_l|$, the changes in $R_t f_{\mathrm{res}}/R_r f$ values for resonance frequencies ($f/f_{\mathrm{res}} = 1$) in a function of $|\hat{P}_l|$ are shown in Fig. 8. It is evident from Fig. 8 that for each resonator the calculation results and the experimental data are in close agreement in a range of $|\hat{P}_l|$ where the energy loss is dominated by the nonlinear absorption. In the case of resonator with the smallest orifice radius this range covers almost all values of $|\hat{P}_l|$ used in the experiment. Larger differences are observed for the resonators with higher orifice dimensions. In the ranges of $|\hat{P}_l|$, where the theory is less accurate, the energy loss is due to the nonlinearity and the viscous damping. In a theoretical model this damping was described by resistance $R_\mu$ (Eq. (2)) and, as may be seen in Fig. 8, a calculated value of $R_\mu$ is somewhat smaller than an experimental one.

### *4.3. Dependence of reactance $X$ on pressure amplitude at closed end of resonator*

An increase in the total loss resistance of Helmholtz resonators is not only unique result of acoustic nonlinearity. The second effect of this phenomenon is a change in the resonator reactance with growing sound intensity. A precise theoretical description of this effect is difficult, therefore in the impedance model of a resonator (presented in Sec. 2) the reactance $X$ was determined by Eq. (4) as in the case of linear theory.

The experimental data shown in Fig. 9 illustrate the changes in nondimensional reactance $X/R_r$ as a function of frequency $f$ for different values of pressure amplitude $|\hat{P}_l|$. The values of $X/R_r$ calculated from Eq. (4) are indicated by solid lines. As may be seen from Fig. 9, there is a good agreement between theory and experiment at the moderate pressure amplitudes $|\hat{P}_l| = 1.6$, 5 Pa. At much higher values of $|\hat{P}_l|$ an increase of the reactance $X$ is observed but it is different for various resonators. The least modification of the reactance can be noted for the resonator with the highest orifice radius (Fig. 9d). For other resonators the changes in $X$ versus frequency at high values of $|\hat{P}_l|$ may appear without any regularity (Fig. 9a) or have almost regular shape (Figs. 9b, 9c). As a result of the increase in the reactance it appears a shift in resonance frequency to higher frequencies which is clearly observed for resonators with the orifice radius $b = 2$ and 2.5 mm at the highest pressure amplitude $|\hat{P}_l|$ (Figs. 9b, 9c).

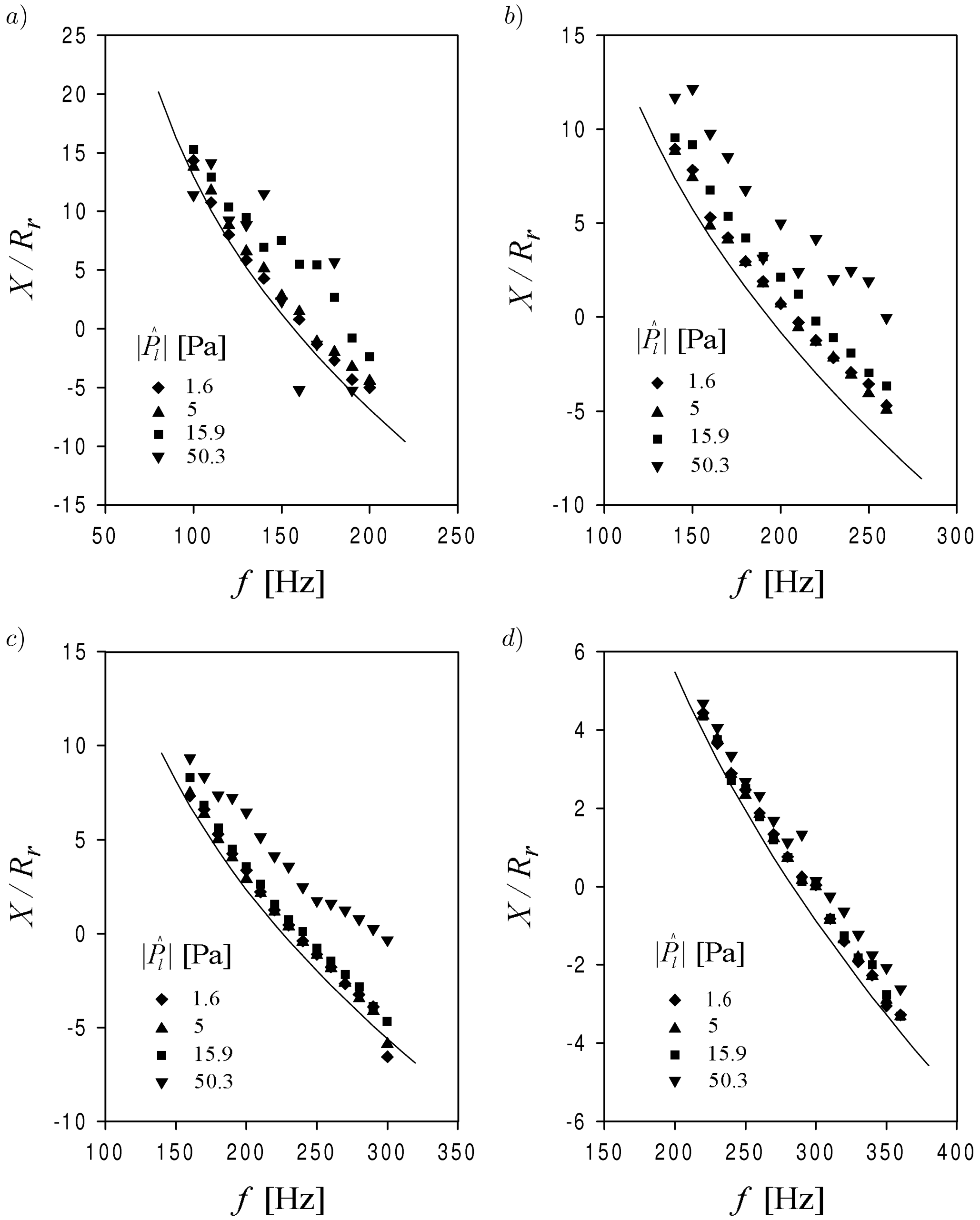


Fig. 9. Changes of nondimensional reactance $X/R_r$ versus frequency $f$ at different pressure amplitudes $|\hat{P}_l|$ for resonators with orifice radius $b$: a) 1.5 mm, b) 2 mm, c) 2.5 mm, d) 3.5 mm; (—) calculation results.

## 5. Conclusions

The experimental results presented in this paper have demonstrated the effect of nonlinearity on acoustic properties of Helmholtz resonators. The most important aspect of this phenomenon is a change in the absorption coefficient $\alpha$ at the high sound intensities. The measurements performed under condition of constant amplitudes $|\hat{P}_i|$ of driving pressure have shown that for a small diameter of the resonator orifice an influence of nonlinearity may be very strong because it results in an increase in $\alpha$ to value near unity at a resonance frequency even at moderate pressure amplitudes (Figs. 4a, 5a). In the case of much higher pressures, as it was predicted by the theory, the observed decrease in $\alpha$ was evidently larger for a smaller orifice diameters (Figs. 3c, 4c, 5c).

According to the theory developed in Part I, a change in $\alpha$ with the sound intensity is connected with an increase of nonlinear resistance. It was confirmed by results of resistance $R_t$ measurements which were performed under condition of constant amplitude $|\hat{P}_l|$ of pressure at the closed end of resonator. A comparison between experimental data and calculation results has proved that at high values of $|\hat{P}_l|$ a relation between the resistance $R_t$ and the pressure amplitude $|\hat{P}_l|$ at the resonance frequency may be approximated by Eq. (15). The agreement between measurements and theory was worse in the range of low values of $|\hat{P}_l|$ when energy absorption is dominated by viscous damping (Fig. 8).

In the presented theory a reactance of Helmholtz resonators has been described as a part of the impedance which is independent of the amplitude of incident wave. A change in the reactance has no influence on absorption properties of resonators but it may cause an increase in the resonance frequency. It appears that the reactance is much less sensitive than the resistance to changes in sound intensity because a shift in the resonance frequency to higher frequencies was clearly observed only at the highest pressure amplitude $|\hat{P}_l|$ (Fig. 9).

## References

[1] F.J. Fahy and C. Schifield, *A note on the interaction between a Helmholtz resonator and an acoustic mode of an enclosure*, J. Sound Vib., **72**, 3, 365–378 (1980).

[2] H.L. Kuntz, R.A. Prydz, F.J. Balena and R.J. Gatineau, *Development and testing of cabin sidewall acoustic resonators for the reduction of cabin tone levels in propfan-powered aircraft*, Noise Control Engineering Journal, **37**, 3, 129–142 (1991).

[3] J.M. Mason and F.J. Fahy, *The use of acoustically tuned resonators to improve the sound transmission loss of double-panel partitions*, J. Sound Vib., **124**, 2, 367–379 (1988).

[4] R.A. Prydz, L.S. Wirt, H.L. Kuntz and L.D. Pope, *Transmission loss of a multilayer panel with internal tuned Helmholtz resonators*, J. Acoust. Soc. Amer., **87**, 4, 1597–1602 (1990).

[5] U. Ingard, *On the theory and design of acoustic resonators*, J. Acoust. Soc. Amer., **25**, 6, 1037–1061 (1953).

[6] D.A. Bies and O.B. Wilson, *Acoustic impedance of a Helmholtz resonator at very high amplitude*, J. Acoust. Soc. Amer., **29**, 6, 711–714 (1957).

[7] J. Wu and I. Rudnick, *Measurements of the nonlinear tuning curves of Helmholtz resonators*, J. Acoust. Soc. Amer., **80**, 5, 1419–1422 (1986).

[8] S. Czarnecki, *Utilization of nonlinear properties of resonators for improving acoustic conditions in rooms*, Proceedings of the 6th International Congress on Acoustics, Tokyo, Japan, 197–200 (1968).

[9] S. Czarnecki, *Nonlinear absorption properties of acoustic resonance systems* [in Polish], Arch. Akustyki, **1**, 4, 37–49 (1969).

[10] M. Meissner, *The influence of acoustic nonlinearity on absorption properties of Helmholtz resonators. Part I. Theory*, Arch. Acoust., **24**, 2, 179–190 (1999).

[11] M. Meissner, *Mechano–acoustic feedback in the case of an interaction between a sound source and a resonance system*, Arch. Acoust., **8**, 3, 235–248 (1983).

ARCHIVES OF ACOUSTICS
**25**, 2, 191–204 (2000)

# ANALYSIS OF BLOOD PRESSURE WAVE IN THE HUMAN COMMON CAROTID ARTERY ON THE BASIS OF NON-INVASIVE ULTRASONIC EXAMINATIONS

T. POWAŁOWSKI

Polish Academy of Sciences
Institute of Fundamental Technological Research
(00-049 Warszawa, Świętokrzyska 21, Poland)
e-mail: tpowal@ippt.gov.p

The aim of the study was the examination of the forward and reflected blood pressure waves in the common carotid artery on the basis of non-invasive ultrasonic examinations. The study concerned the effect of stenosis of the internal carotid artery caused by atherosclerosis on the mean reflection coefficient modulus and the time delay between the reflected blood pressure wave and the forward blood pressure wave. The investigations were carried out on a group of healthy persons (30 cases) and on a group of sick persons (17 cases) with stenosis or occlusion of the internal carotid artery.

**Keywords:** forward and reflected blood pressure waves, vascular input impedance, common carotid artery, ultrasound.

## 1. Introduction

The blood pressure wave propagating along the vascular tree is reflected, the main points of reflection being the places of stenosis, or bifurcations of arteries [5]. In the case when behind the point of measurements there is a series of blood pressure wave reflections at various points spaced from one another, we cannot practically separate from one another the individual reflected waves reaching the measurement point. Under such circumstances, the wave propagating in the direction opposite to the forward wave and being superposition of the reflected waves is considered reflected wave. The shape of the blood pressure wave observed in particular points along the vascular tree can be reconstructed by a sum of the cosine waves which amplitudes and phases are determined in frequency domain as the results from the Discrete Fourier Transform of the blood pressure wave. The relationship between the spectrum components of the total $P$, forward $P_f$ and reflected $P_r$ blood pressure waves for the successive harmonics $n$ of the heartbeat frequency in frequency domain is as follows:

$$P_n = P_{fn} + P_{rn} = P_{fn}(1 + \varGamma_n), \tag{1}$$

where

$$P_n = |P_n|e^{j\theta_n}, \quad P_{fn} = |P_{fn}|e^{j\theta_{fn}}, \quad P_{rn} = |P_{rn}|e^{j\theta_{rn}}, \quad \varGamma_n = |\varGamma_n|e^{j\gamma_n}.$$

The reflection coefficient $\Gamma_n$ present in formula (1) is calculated on the basis of the vascular input impedance $Z_n$ and characteristic impedance $Z_{on}$ measured in the chosen cross-section of the artery:

$$\Gamma_n = \frac{P_{rn}}{P_{fn}} = \frac{Z_n - Z_{on}}{Z_n + Z_{on}} = |\Gamma_n| e^{j\gamma_n}. \tag{2}$$

The input and characteristic impedances are defined in the frequency as:

$$Z_n = \frac{P_n}{Q_n} = |Z_n| e^{j\varphi_n}, \qquad Z_{on} = \frac{P_{fn}}{Q_{fn}} = |Z_{on}| e^{j\phi_n}, \tag{3}$$

where $P_n$, $P_{fn}$, are spectrum components of the total and forward blood pressure waves, $Q_n$, $Q_{fn}$ are spectrum components of the total and forward blood flow waves.

According to formula (1) the spectrum components $P_{fn}$ and $P_{rn}$ of the forward and reflected blood pressure waves are calculated for the succesive harmonics $n$ of the heartbeat frequency as follows:

$$P_{fn} = \frac{P_n}{(1+\Gamma_n)} = |P_{fn}| e^{j\theta_{fn}}, \qquad P_{rn} = P_n - P_{fn} = |P_{rn}| e^{j\theta_{rn}}. \tag{4}$$

The components $P_{fn}$ and $P_{rn}$ are the basis for detrmination of the course of the forward and reflected blood pressure waves in time domain.

The phenomenon of blood pressure wave reflection has been considered up to now only on the basis of the invasive measurements performed mainly on animals [17, 20]. In this study the forward and reflected blood pressure waves in the human common carotid artery was determined on the basis of ultrasonic non-invasive measurements of the blood pressure and volumetric blood flow. The aim of the study was to estimate the effect of the internal carotid artery stenosis caused by atherosclerosis on the mean reflection coefficient modulus and delay of the reflected wave relative to the forward wave. The time delay $\Delta t$ was determined by the zero-crossing method between the rising slopes of the forward and reflected blood pressure waves at the mean blood pressure level $P_a$ (Fig. 5 and 7). Moreover the time delay was also determined by the correlation method. The values of the mean reflection coefficient modulus $|\Gamma|_a$ was calculated on the basis of the values of the moduli $|P_{fn}|$ and $|P_{rn}|$ of the spectrum components of the forward and reflected blood pressure waves for the first ten harmonics of the heartbeat frequency according to the formula:

$$|\Gamma|_a = \frac{\frac{1}{10}\sum_{n=1}^{10} |P_{rn}|}{\frac{1}{10}\sum_{n=1}^{10} |P_{fn}|}. \tag{5}$$

The mean reflection coefficient modulus thus determined is mainly dependent upon those harmonic components, which have major influence on the shape of the forward and reflected blood pressure waves.

## 2. Method and equipment

In the developed method the instantaneous values of blood pressure $P(t)$ in the common carotid artery was determined on the basis of ultrasonic measurements of the instantaneous artery diameter $D(t)$. The function $D(P)$ presented by Powałowski and Peńsko [10] having the following form is assumed as the basis of calculations:

$$D(P) = D_{\min}\sqrt{1+\frac{1}{\alpha}\ln\left(\frac{P}{P_d}\right)} \qquad \text{for} \quad P \geq \frac{P_d}{\exp(\alpha)} > 0, \tag{6}$$

where $\alpha$ has been defined as a logarithmic artery wall rigidity coefficient and has the form expressed by the following formula:

$$\alpha = \frac{D_{\min}^2}{(D_{\max}^2 - D_{\min}^2)}\ln\left(\frac{P_s}{P_d}\right), \tag{7}$$

where $D_{\min}$ and $D_{\max}$ are minimum and maximum artery diameters corresponding to the diastolic blood pressure $P_d$ and systolic blood pressure $P_s$, respectively. Upon transformation of formula (6) the instantaneous blood pressure $P(t)$ is given as:

$$P(t) = P_d \exp\left[\frac{D^2(t) - D_{\min}^2}{D_{\max}^2 - D_{\min}^2}\ln\left(\frac{P_s}{P_d}\right)\right]. \tag{8}$$

In the non-invasive examinations the blood pressure $P(t)$ thus determined was calibrated by means of the systolic blood pressure and diastolic blood pressures, measured by means of a sphigmomanometer. In the case of the blood pressure $P(t)$ determination in the carotid arteries, the blood pressure $P_s$ and $P_d$ measurements were performed on the brachial artery, when the patient was lying down. A right to use the function described by formula (6) has been confirmed for a group consisting of 20 persons by Powałowski *et al.* [13, 14] for the common carotid artery for different values of the systolic and diastolic blood pressures. The results of the investigations of the relationship between the diameter of the common carotid artery and the variations of the systolic and diastolic blood pressure in the brachial artery obtained by the above mentioned authors are presented for the three chosen persons in Fig. 1.

The relationship between the common carotid artery diameter and the blood pressure was also investigated in the conditions of the dynamic blood pressure variations. Investigations were carried out in the common carotid artery of a dog([1]). The instantaneous blood pressure and the instantaneous artery diameter were measured simultaneously in the same artery cross-section. The blood pressure was measured invasively by means of 1 mm pressure catheter developed by Sentron. The artery diameter was examined non-invasively using VED ultrasonic equipment described in the further part of this paper. The results of the examinations in the common carotid artery of a dog (Fig. 2) have shown that relationship (8) describes perfectly well the blood pressure variations. The coefficient

(1) Investigations were performed at the University in Maastricht (the Netherlands) within research project PL 92.0907 financed by the European Commission.

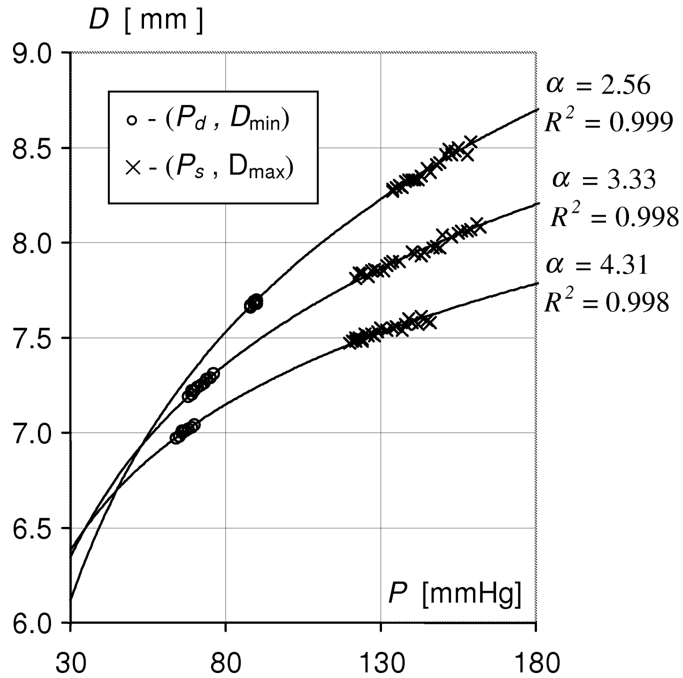


Fig. 1. Results of the measurements [13] of the relationship between diameter $D$ (minimum $D_{\min}$ and maximum $D_{\max}$ diameter) of the common carotid artery and the blood pressure $P$ (diastolic $P_d$ and systolic $P_s$ pressure) on the brachial artery for three patients aged 36, 38, and 42 years, for whom the mean value of $\alpha$ coefficient as calculated from formula (7), was 3.33, 2.56 and 4.31, respectively. Solid line presents the function $D(P)$ determined from formula (6). The function $D(P)$ was plotted by means of the least squares method. Conformity of description of the experimental points by the assumed function $D(P)$ has been expressed by the coefficient of determination $R^2$.

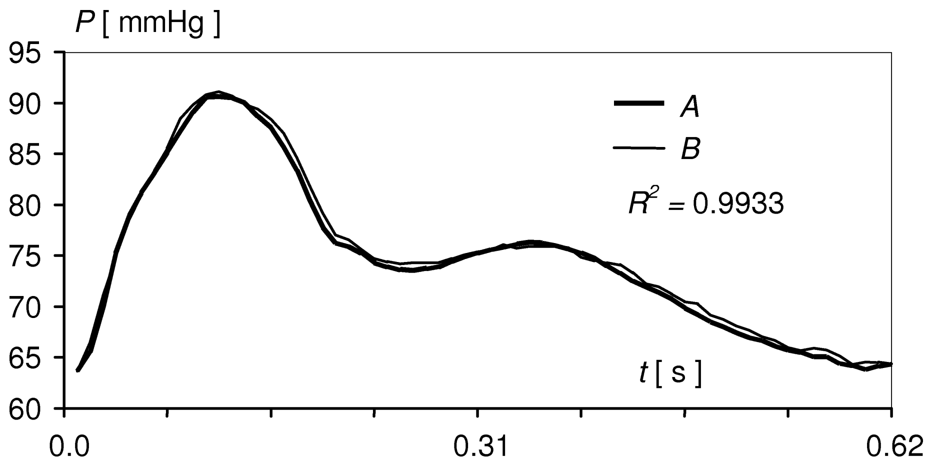


Fig. 2. Blood pressure $P$ averaged from the consecutive ten cardiac cycles in the common carotid artery of a dog: (A) — measured, (B) — calculated on the basis of artery diameter variations, according to relationship (8).

of determination $R^2$ between the blood pressure measured in the invasive way and that calculated from formula (8) was 0.9933. Moreover, the obtained results of investigations have shown that the effect connected with the viscous properties of the artery wall in the relationship between the artery diameter variations and blood pressure variations may be neglected. The phase shift in the relationship $D(P)$ did not exceed 9° for the first five harmonic components of the instantaneous blood pressure $P(t)$. This has confirmed the earlier works done by BERGEL [1, 2], LEAROYD *et al.* [8], GOW *et al.* [6, 7] and WESTERHOF *et al.* [19]. The above mentioned authors agree that the phase shift between the artery diameter variations and blood pressure variations does not exceed $10^0$.

Non-invasive blood pressure measurements, together with non-invasive ultrasonic measurements of the volumetric blood flow were basis for determination of the vascular input impedance [12].

Besides the input impedance, subsequent magnitude necessary for determination of the blood pressure wave reflection coefficient is the characteristic impedance. In this study the characteristic impedance was determined on the basis of the formula given by WOMERSLEY [21]. Womersley has presented a relationship, which describes characteristic impedance of the artery, based on the assumptions that artery with ideally elastic wall is contracted and does not move in the longitudinal direction and that blood can be treated as viscous Newtonian liquid:

$$Z_{on} = \frac{\rho c}{\pi R^2 \sqrt{(1-\sigma^2) M'_{10n}}} e^{-j\frac{\varepsilon_{10n}}{2}}, \tag{9}$$

where $\rho$ is the blood density, $R$ is the artery radius, $\sigma$ is the Poisson constant, $M'_{10n}$, and $\varepsilon_{10n}$ are values, which are functions of the artery radius, blood viscosity and harmonics $n$ of the heartbeat frequency, $c$ is the pulse wave velocity.

Values $M'_{10n}$ and $\varepsilon_{10n}$ are given in tables [9]. Pulse wave velocity $c$ given in formula (9) has been defined on the basis of the Moens–Korteweg equation:

$$c = \sqrt{\frac{Eh}{2R\rho}}, \tag{10}$$

where $E$ is the Young's modulus of the artery wall, $h$ is the artery wall thickness, $\rho$ is the blood density, $R$ is the mean artery radius.

Moens–Korteweg formula has been derived for an extremely thin-walled tube for which the condition $h/R \ll 1$ is satisfied. In order to eliminate difficulties connected with the measurement of the artery wall thickness and Young's modulus, BRAMWELL and HILL [3] in 1922 proposed the following relationship describing the value of the pulse wave velocity $c$:

$$c = \sqrt{\frac{V\,dP}{\rho\,dV}}\,, \tag{11}$$

where $\rho$ is the blood density, $dP$ is the blood pressure variation producing relative variation of the artery volume $dV/V$.

Having assumed that the length of the artery has not changed due to blood pressure variations, we can obtain formula (11) in the following form:

$$c = \sqrt{\frac{S\,dP}{\rho\,dS}}\,, \tag{12}$$

where $dP$ is the blood pressure variation, which causes relative variation of the cross-section area of the artery $dS/S$.

The formula given above has been confirmed theoretically in the paper published by Tedgui *et al.* [18] for an incompressible Newtonian liquid flowing in an elastic tube. In the paper cited above it has been proved that the pulse wave velocity described by formula (12) corresponds to the pulse wave velocity as calculated on the basis of the Moens–Korteweg formula. According to formula (12), in the non-invasive ultrasonic investigations, the pulse wave velocity has been calculated from the following relationship:

$$c = \sqrt{\frac{S\,\Delta P}{\rho\,\Delta S}} = \sqrt{\frac{(P_s - P_d)D_{\min}^2}{\rho\,(D_{\max}^2 - D_{\min}^2)}}\,, \tag{13}$$

where $D_{\max}$ and $D_{\min}$ are maximum and minimum internal artery diameter with the systolic $P_s$ and diastolic $P_d$ blood pressures being subordinated to these values, respectively.

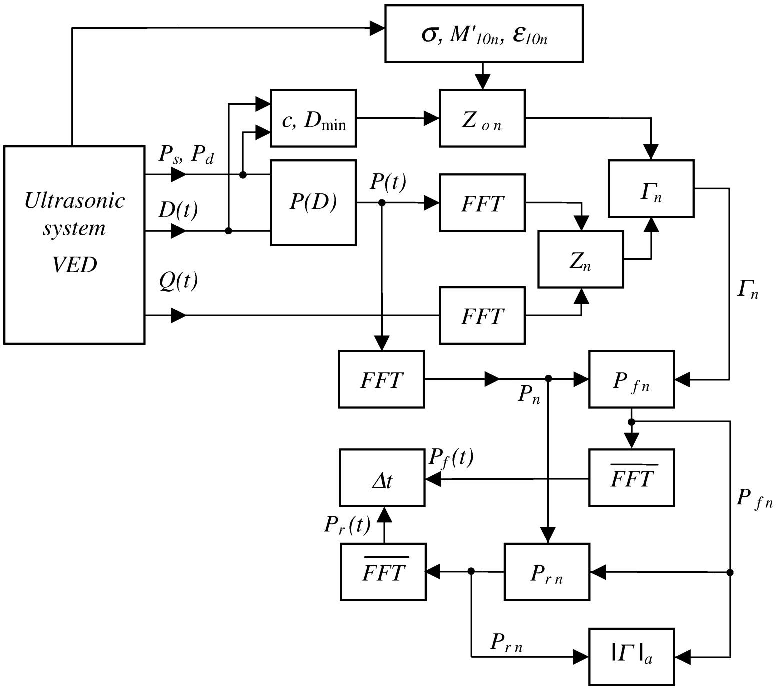


Fig. 3. Flow chart of determination and analysis of the forward $P_f$ and reflected $P_r$ blood pressure waves according to the formulae: (8), (4), (2), (3), (9), (13) and (5); FFT — Fast Fourier Transform, $\overline{\text{FFT}}$ — inverse Fast Fourier Transform, $|\mathit{\Gamma}|_a$ — mean reflection coefficient modulus, $\Delta t$ — time delay of the reflected blood pressure wave relative to the forward blood pressure wave.

The forward and reflected blood pressure waves were determined in conformity with formulae: (8), (4), (2), (3), (9) and (13) on the basis of the simultaneous measurements of the instantaneous values of the volumetric blood flow $Q(t)$ and artery diameter $D(t)$ in the same cross-section area of the common carotid artery and on the basis of the measurement of the systolic blood pressure $P_s$ and diastolic blood pressure $P_d$ on the brachial artery by means of sphigmomanometer. The flow chart of determination and analysis of the forward and reflected preesure waves is given in Fig. 3. The investigations were carried out by means of VED ultrasonic equipment developed at the Institute of Fundamental Technological Research of the Polish Academy of Sciences. This equipment consists of a continuous wave Doppler flowmeter with a two-channel 128 point FFT Doppler signal analyser and a pulse wall tracking system [11]. The frequency of the ultrasonic wave transmitted in the Doppler flowmeter was 4.5 MHz, and in the tracking system — 6.75 MHz. The longitudinal resolution at the artery diameter measurements as determined on the basis of the model investigations was $< 0.33$ mm. Measuring accuracy of artery wall displacements was 7 µm. Measuring data were presented during the investigations on the screen of an IBM PC connected on line with an ultrasonic equipment and were stored in the computer memory (Fig. 4). Apart from the data obtained from ultrasonic measurements, also the values of the systolic and the diastolic blood pressures were transmitted to the computer memory. The forward and reflected blood pressure waves were determined using 128 point Fast Fourier Transform (FFT).

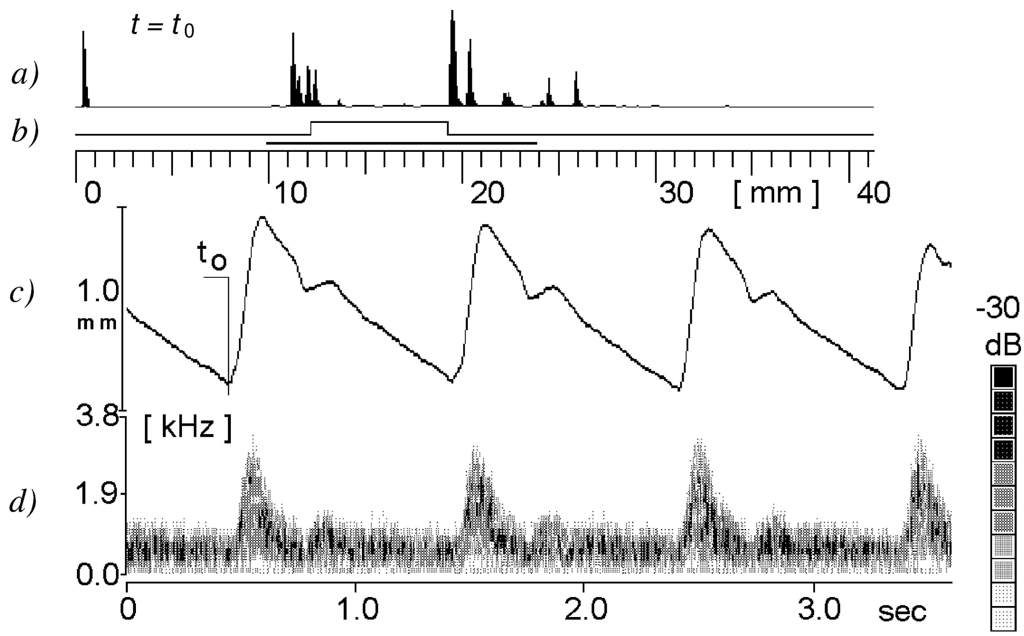


Fig. 4. Data presented in the course of the measurements in the human common carotid artery: a) echoes from artery wall surface, b) gate presenting internal artery diameter, c) relative artery diameter variation, d) power density spectrum of the Doppler signal; $t_0$ is a moment of taking of the picture of the recorded echoes.

## 3. Results

The examinations performed in the common carotid artery were preceded by an estimate of influence of stenosis of the brachial artery caused by compression on the values of the mean reflection coefficient modulus and the time delay of the reflected blood pressure wave with respect to the forward blood pressure wave. (Powałowski *et al.* [15]). The measurements were performed on a male 22 years old. The results of examinations are presented in Fig. 5. The measuring point was located 56 cm from fingertips. An apparent blood pressure wave reflection point as determined on the basis of the pulse wave velocity (formula (13)) and the time delay $\Delta t$ between the reflected and forward waves was spaced by 60 cm from the measuring point. After compressing the artery at a distance of 12 cm from the measuring point, the time delay $\Delta t$ has been reduced from 132 ms to 35 ms and the value of the mean reflection coefficient modulus $|\Gamma|_a$ has increased from 0.4398 to 0.7983. Compressing of the brachial artery brought a 60% reduction in the volumetric blood flow.

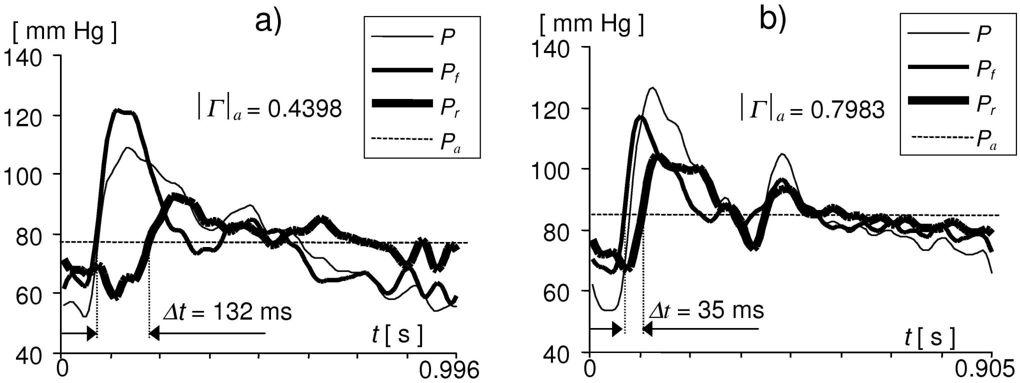


Fig. 5. Blood pressure waves: total $P$, forward $P_f$ and reflected $P_r$ determined on the basis of the brachial artery measurements: a) without artery compression, b) with artery compression at a point lying 12 cm distal the measurement point; $P_a$ is the mean blood pressure.

The clinical examinations (Powałowski *et al.* [16] were performed at the Department of the General and Thoracic Surgery of the Medical Academy in Warsaw on a control group of healthy persons without any atherosclerotic lesions in the carotid arteries and on a group of sick persons with atherosclerotic lesions in the initial segment of the internal carotid artery (Fig. 6). The examinations were carried out in the common carotid artery at a distance of 3–4 cm proximal to the bifurcation of the artery. The ultrasonic examinations (B-mode+Doppler) did not show any atherosclerotic plaque in the common carotid artery where the measurements were taken. The measurements were done while the subjects were lying down, following 15 minute rest periods. The stenosis range of the internal carotid artery was classified on the basis of the combined ultrasonographic and Doppler measurements. Generally accepted criteria were used (de Bray and Glatt [4]). The results of the blood flow and blood pressure measurements have been averaged for four cardiac cycles. In Fig. 7 are presented the results of the chosen blood

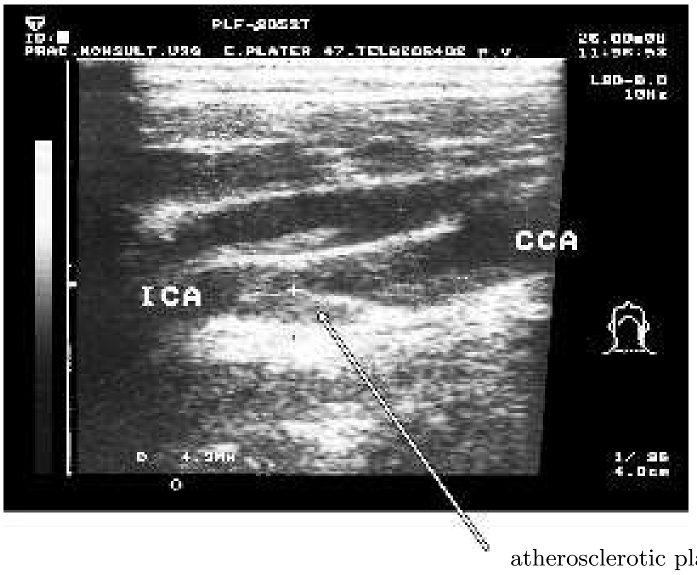


atherosclerotic plaque

Fig. 6. Ultrasonic B-mode image of the common carotid artery (CCA) bifurcation in the case of a person with atherosclerosis of the internal carotid artery (ICA).

pressure $P$ and blood flow $Q$ measurements, the input and characteristic impedance, as well as the forward and reflected blood pressure wave for the healthy person and for the patients with 50% and 70% stenosis of the internal carotid artery. It may be seen that in the case of persons with stenosis of the internal carotid artery there is a visible increase in the input impedance modulus $|Z_n|$ of with respect to the characteristic impedance modulus $|Z_{on}|$, coupled with an increase of the reflected wave amplitude and shortening of the time delay $\Delta t$ of the reflected blood pressure wave $P_r$ with respect to the forward blood pressure wave $P_f$.

The total results of examinations have been given in Table 1. Amplitude and time delay of the reflected blood pressure wave measured in the common carotid artery were obtained as a sum of the waves reflected from various points of vascular system fed by the common carotid artery. The results of the examinations have shown that an increase of the degree of stenosis of the internal carotid artery is also accompanied by an increase in the value of the mean reflection coefficient modulus and decrease in the time delay of the reflected blood pressure wave relative to the forward blood pressure wave. In the case of the persons with a critical stenosis, or occlusion of the internal carotid artery, the mean reflection coefficient modulus was greater by about 48% and the apparent reflection point as determined on the basis of the time delay and the pulse wave velocity (formula (13)) was situated at distance $\Delta L$ relative to the measuring point about 4.4 times shorter than in the case of the healthy persons.

The time delay $\Delta t$ of the reflected blood pressure wave relative to the forward blood pressure wave obtained by the zero crossing method was compared with the time delay obtained by the correlation method. In order to enhance resolution of the correlation

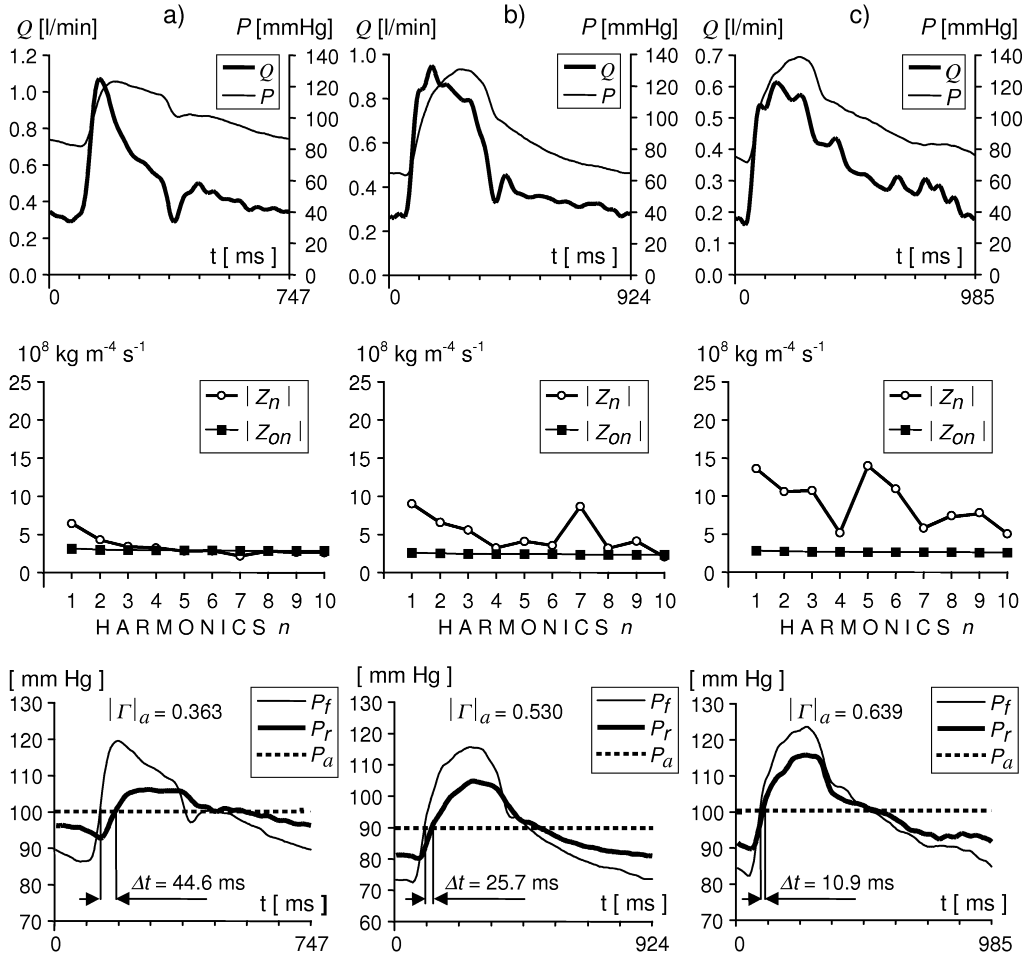


Fig. 7. Results of examination in the common carotid artery in the case of the healthy person (a), the person with 50% stenosis of the internal carotid artery (b) and the person with 70% stenosis of the internal carotid artery (c).

method, the time course of the forward and reflected blood pressure waves for the given cardiac cycle was divided into $2^{12}$ samples having assumed linear approximation between the primary samples ($2^7$ samples) of both waves. Average difference of the values of the time delay $\Delta t$ following from the above methods of $\Delta t$ determination was 2%, for A, C and D groups of the persons being examined given in Table 1, and 10% — for group B.

In this paper the propagation of the forward wave and the wave reflected between two measuring points situated at a known distance from each other was also considered. The distance between the measuring points was determined on the basis of the time delay difference at both measuring points and on the basis of pulse wave velocity, according to the following relationship:

$$\Delta L^* = \frac{c(\Delta t_1 - \Delta t_2)}{2}, \tag{14}$$

where $\Delta t_1$ and $\Delta t_2$ are time delays between the reflected wave and the forward wave at a measuring point situated at a greater and smaller distance from the wave reflection point respectively, $c$ is the pulse wave velocity in the distance between the measuring points.

**Table 1.** Results of measurements in the common carotid artery for a control group of healthy persons (A) and the persons with stenosis (B – D) of the internal carotid artery (ICA). $P_s$, $P_d$ are systolic and diastolic blood pressures on the brachial artery, $D_{\min}$ is minimum internal diameter, $Q_{\text{med}}$ is the mean volumetric blood flow, $c$ is the pulse wave velocity, $|\Gamma|_a$ is the mean reflection coefficient modulus, $\Delta t$ is the time delay of the reflected blood pressure wave relative to the forward blood pressure wave determined by zero-crossing method, $\Delta L$ is the distance between the measuring point and the apparent blood pressure wave reflection point, $\Delta t^*$ is the time delay of the reflected blood pressure wave relative to the forward blood pressure wave determined by the correlation method.

| Examined group | (A) Control | (B) ICA stenosis 50% | (C) ICA stenosis $50-70\%$ | (D) ICA stenosis $> 90\%$ or occlusion |
|---|---|---|---|---|
| Number of cases | 30 | 5 | 6 | 6 |
| Age [years] | $48.3 \pm 14.2$ | $59.0 \pm 12.5$ | $62.3 \pm 10.0$ | $64.8 \pm 7.4$ |
| $P_s$ [mmHg] | $119.7 \pm 11.2$ | $138.4 \pm 7.4$ | $158.7 \pm 24.9$ | $142.5 \pm 19.4$ |
| $P_d$ [mmHg] | $74.1 \pm 8.6$ | $79.6 \pm 9.5$ | $83.5 \pm 11.1$ | $75.8 \pm 9.4$ |
| $D_{\min}$ [mm] | $7.182 \pm 1.015$ | $8.294 \pm 0.733$ | $8.728 \pm 0.750$ | $9.528 \pm 0.780$ |
| $Q_{\text{med}}$ [l/min] | $0.605 \pm 0.113$ | $0.589 \pm 0.082$ | $0.595 \pm 0.153$ | $0.416 \pm 0.094$ |
| $c$ [m/s] | $6.80 \pm 1.54$ | $8.70 \pm 1.96$ | $8.65 \pm 2.43$ | $8.94 \pm 1.58$ |
| $\|\Gamma\|_a$ | $0.448 \pm 0.048$ | $0.527 \pm 0.024$ | $0.603 \pm 0.083$ | $0.661 \pm 0.060$ |
| $\Delta t$ [ms] | $52.7 \pm 13.4$ | $27.0 \pm 6.1$ | $22.1 \pm 10.6$ | $9.1 \pm 4.8$ |
| $\Delta L$ [cm] | $17.6 \pm 5.5$ | $11.4 \pm 1.2$ | $9.0 \pm 3.9$ | $4.0 \pm 2.0$ |
| $\Delta t^*$ [ms] | $53.8 \pm 13.9$ | $24.6 \pm 5.7$ | $21.7 \pm 9.3$ | $9.0 \pm 4.6$ |

The examinations were carried out in the human common carotid artery and on a model([2]) in elastic tube ($\sigma = 0.5$) of inside diameter 19.8 mm, through which liquid of viscosity $\eta$ and density $\rho$ similar to those of blood ($\eta = 3.3 \cdot 10^{-2}$ P, $\rho = 1100\,\text{kg/m}^3$) flowed. The obtained results are shown in Table 2. It may be seen that the distance between the measuring points as determined from the time delay difference and the pulse wave velocity differs only slightly from the existing distance between the measuring points. This difference was equal to 5% for a segment of the common carotid artery 3 cm long and 1% for a segment of elastic tube 25 cm long.

**Table 2.** Distance between the measuring points: measured ($\Delta L$) and determined on the basis of the pulse wave velocity and on the basis of the time delay difference at two measuring points ($\Delta L^*$) (formula (14)).

| | $\Delta L$ | $\Delta L^*$ |
|---|---|---|
| Elastic tube | 25.0 cm | 24.75 cm |
| Common carotid artery | 3.0 cm | 2.86 cm |

The influence of atherosclerosis in the internal carotid artery upon the phenomenon of blood pressure wave reflection has also been considered theoretically, by calculation

([2]) The model investigations were carried out at the Department of Mechanical Engineering, Technical University of Eindhoven [15].

of the value of the reflection coefficient in the common carotid artery for the case of the normal internal and external carotid arteries, as well as for the case of an occlusion of the internal carotid artery. In the calculations the results of non-invasive blood pressure and volumetric blood flow measurements in the internal and external carotid arteries for a healthy male aged 38 were applied. The measurements were carried out close to the bifurcation of the carotid artery. Neglecting the distance of the measuring points from the bifurcation of the common carotid artery, the time course of the blood flow velocity in the common carotid artery at the point of bifurcation was calculated as a sum of the time courses of the blood flows in the external and the internal carotid arteries. Moreover, blood pressure has been determined as an arithmetic mean of the blood pressures in the external and the internal carotid arteries. The obtained results of measurements were basis for the determination of the reflection coefficients in the three above mentioned carotid arteries at the point of bifurcation of the common carotid artery. Reflection coefficient in the common carotid artery was determined from the successive harmonic $n$ of the heartbeat frequency from the following relationship:

a) for the case of the normal (without atherosclerotic plaques) internal and external carotid arteries:

$$\Gamma_{cn} = \frac{Z_{cn} - Z_{con}}{Z_{cn} + Z_{con}} = \frac{\dfrac{Z_{en}Z_{in}}{Z_{en} + Z_{in}} - Z_{con}}{\dfrac{Z_{en}Z_{in}}{Z_{en} + Z_{in}} + Z_{con}}$$

$$= \frac{\dfrac{1}{Z_{con}} - \left[\dfrac{1}{Z_{eon}}\left(\dfrac{1-\Gamma_{en}}{1+\Gamma_{en}}\right) + \dfrac{1}{Z_{ion}}\left(\dfrac{1-\Gamma_{in}}{1+\Gamma_{in}}\right)\right]}{\dfrac{1}{Z_{con}} + \left[\dfrac{1}{Z_{eon}}\left(\dfrac{1-\Gamma_{en}}{1+\Gamma_{en}}\right) + \dfrac{1}{Z_{ion}}\left(\dfrac{1-\Gamma_{in}}{1+\Gamma_{in}}\right)\right]}. \tag{15}$$

b) for the case of the internal carotid artery occlusion:

$$\Gamma_{cn} = \frac{Z_{cn} - Z_{con}}{Z_{cn} + Z_{con}} = \frac{Z_{en} - Z_{con}}{Z_{en} + Z_{con}} = \frac{\dfrac{1}{Z_{con}} - \dfrac{1}{Z_{eon}}\left(\dfrac{1-\Gamma_{en}}{1+\Gamma_{en}}\right)}{\dfrac{1}{Z_{con}} + \dfrac{1}{Z_{eon}}\left(\dfrac{1-\Gamma_{en}}{1+\Gamma_{en}}\right)}, \tag{16}$$

where $Z_{cn}$, $Z_{en}$, $Z_{in}$ are the input impedances, $Z_{con}$, $Z_{eon}$, $Z_{ion}$ are the characteristic impedances, $\Gamma_{cn}$, $\Gamma_{en}$, $\Gamma_{in}$ are the reflection coefficients in carotid arteries: common, external and internal respectively.

In the case of the normal carotid arteries it has been assumed at the determination of the reflection coefficient $\Gamma_{cn}$ in the common carotid artery that the characteristic admittance in the common carotid artery at the point of bifurcation is equal to the sum of the characteristic admittances in the external and internal carotid arteries. The reflection coefficient $\Gamma_{cn}$ calculated from formulae (15) and (16) was basis for determination of the forward and reflected blood pressure waves in the common carotid artery. The mean modulus $|\Gamma|_a$ of the reflection coefficient was calculated on the basis of forward wave modulus and reflected wave modulus according to the formula (5). The results of calculations of the mean modulus $|\Gamma|_a$ of the reflection coefficient were presented in Table 3.

The performed calculations have confirmed the phenomenon of an increase of the value of mean modulus $|\Gamma|_a$ for the case of the occluded internal carotid artery (Table 1).

**Table 3.** Mean modulus $|\Gamma|_a$ of the reflection coefficient calculated on the basis of the non-invasive blood pressure and blood flow velocity measurements in the common carotid artery (CCA), external carotid artery (ECA) and internal carotid artery (ICA) and on the basis of a model of bifurcation of the common carotid artery (*) described by the formulae (15) and (16).

| Artery | $\|\Gamma\|_a$ |
|---|---|
| ECA | 0.444 |
| ICA | 0.540 |
| CCA (for normal ECA and ICA) | 0.471, (0.490*) |
| CCA (for occluded ICA+ normal ECA) | 0.663* |

## 4. Conclusions

The results of examinations obtained in the human common carotid artery indicate that the stenosis of the internal carotid artery caused by atherosclerosis was the source of the reflected blood pressure wave. This is expressed by an increase in value of the mean reflection coefficient and a decrease in the time delay between the reflected and forward blood pressure wave accompanying the degree of stenosis of the common carotid artery. These observations indicate that the proposed method of investigation of the forward and reflected blood pressure waves may be in the future a new diagnostic tool useful for the detection of atherosclerotic lesions in the arteries.

## References


[1] D.H. Bergel, *The visco-elastic properties of the arterial wall*, PhD Thesis, University of London 1960.

[2] D.H. Bergel, *The dynamic elastic properties of the arterial wall*, J. Physiol., 156, 458–469 (1961).

[3] J.C. Bramwell and A.V. Hill, *The velocity of the pulse wave in man*, Proc. Roy. Soc. London, s. B, 93, 298–306 (1922).

[4] J.M. De Bray and B. Glatt, *Quantification of atheromatous stenosis in the extracranial internal carotid artery*, Cerebrovasc Dis., **5**, 414–426 (1995).

[5] U. Gessner, *Vascular input impedance*, [in:] Cardiovascular Fluid Dynamics, D.H. Bergel [Ed.], Academic Press, London and New York, vol. 1, chapter 10, 315–349 (1972).

[6] B.S. Gow, D. Schonfeld and D.J. Patel, *The dynamic elastic properties of canine left circumflex coronary artery*, J. Biomechanics, **7**, 389–395 (1974).

[7] B.S. Gow and C.D. Hadfield, *The elasticity of canine and human coronary arteries with reference to postmortem changes*, Circ. Res., **45**, 588–594 (1979).

[8] B.M. Learoyd and M.G. Taylor, *Alterations with age in the viscoelastic properties of human arterial walls*, Circ. Res., **18**, 278–292 (1966).

[9] D.A. McDonald, *Blood flow in arteries*, E. Arnold Ltd., London 1960.

[10] T. Powałowski and B. Peńsko, *A noninvasive ultrasonic method for the elasticity evaluation of the carotid arteries and its application in the diagnosis of the cerebro-vascular system*, Archives of Acoustics, **13**, 1-2, 109–126 (1988).

[11] T. Powałowski, *Ultrasonic system for noninvasive measurements of hemodynamic parameters of human arterial-vascular system*, Archives of Acoustics, **13**, 1-2, 89–108 (1988).

[12] T. Powałowski, *A noninvasive ultrasonic method for vascular input impedance determination applied in diagnosis of the carotid arteries*, Archives of Acoustics, **14**, 3-4, 293–312 (1989).

[13] T. Powałowski and Z. Trawiński, *Noninvasive evaluation of the elasticity of common carotid artery wall*, Archives of Acoustics, **19**, 4, 451–465 (1994).

[14] T. Powałowski, Z. Trawiński and M. Żebrowski, *The method and ultrasonic equipment for elasticity examination of the carotid arteries*, Lecture notes of the ICB Seminars Ultrasound in Biomeasurements, Diagnostics and Therapy, Warsaw, September 1994, Ed. ICB, **24**, 156–169 (1995).

[15] T. Powałowski, Z. Trawiński, L. Borowska and M. Rutten, *Non-invasive ultrasonic examination of the forfard and reflected pressure wave in human arteries*, Lecture notes of the ICB Seminars Ultrasound in Biomeasurements, Diagnostics and Therapy, Warsaw, September 1998, Ed. ICB, **42**, 158–164 (1999).

[16] T. Powałowski, Z. Trawiński, A. Hoeks and M. Rutten, *Ultrasonic examination of the forward and reflected pressure waves in human arteries*, 137th Meeting of the Acoustical Society of America and the 2nd Conventional of the European Acoustics Association, Forum Acousticum, Berlin, March 14-19, Collected Papers (CD) (1999).

[17] W. Sperling, R.D. Bauer, R. Busse, H. Korner and Th. Pasch, *The resolution of arterial pulses into forward and backward waves an approach to the determination of the characteristic impedance*, Pflugers Arch., **335**, 217–227 (1975).

[18] A.S. Tedgui, B.L. Levy and S.R. Sebag, *Instantaneous blood flow, impedance and elastic properties computed in man from aortic pulse waves*, J. Theor. Biol., **101**, 345–354 (1983).

[19] N. Westerhof and A. Noordergraaf, *Arterial viscoelasticity. A generalized model, effect on input impedance and wave travel in the systematic tree*, J. Biomechanics, **3**, 357–379 (1970).

[20] N. Westerhof, P. Sipkema, G.C. Van Den Bos and G. Elzinga, *Forward and backward waves in the arterial system*, Cardiovascular Research, **6**, 648–656 (1972).

[21] J.R. Womersley, *Method for the calculation of velocity, rate of flow and viscous drag in arteries when the pressure gradient is known*, J. Physiol., **127**, 553–563 (1955).

ARCHIVES OF ACOUSTICS
**25**, 2, 205–212 (2000)

# COMMON CAROTID WALL ELASTICITY AND INTIMA-MEDIA THICKNESS EXAMINATIONS BY MEANS OF ULTRASOUND

T. POWAŁOWSKI, Z. TRAWIŃSKI

Polish Academy of Sciences
Institute of Fundamental Technological Research
(00-049 Warszawa, Świętokrzyska 21, Poland)

L. HILGERTNER

Department of General and Thoracic Surgery
Medical Academy
(Warsaw, Poland)

The aim of this study was to examine the relation between the intima-media thickness and the wall elasticity measured simultaneously in the same cross-section of the common carotid artery. A group of 40 persons (19 healthy and 21 with hypertension and/or atherosclerosis) aged 22 to 81 were diagnosed by means of ultrasound. A high correlation occurred between the wall stiffness coefficient $\alpha$ and the intima-media thickness ($r = 0.950$, $p < 0.00001$).

**Keywords:** arterial wall elasticity, intina-media thickness, carotid artery, ultrasound.

## 1. Introduction

Non-invasive examinations of arteries walls are essential in modern medical diagnosis. Changes in the wall structure resulting from age and vascular diseases, including hypertension and atherosclerosis contribute to the increase of its stiffness and thickness [1, 2, 5, 9 – 11, 15, 17, 19, 22, 23, 25, 26]. Ultrasonic measurements of vascular wall dimensions and its elasticity are carried out independently, owing to the different measuring techniques and applied apparatus. The wall thickness is assessed through analysis of two-dimensional ultrasonic image (B-mode) of artery [1, 5, 9, 10, 26]. Wall elasticity is examined by means of ultrasonic wall tracking systems detecting changes in vascular diameter influenced by blood pressure changes [2, 11, 15, 19].

The paper presents the results of simultaneous ultrasonic measurements of wall elasticity and intima-media thickness in the common carotid artery which were carried out on a group of 40 persons (19 healthy and 21 with hypertension and/or atherosclerosis) aged 22 to 81.

## 2. Method and equipment

Wall elasticity in the common carotid artery was determined on the basis of ultrasonic measurement of the maximum and minimum diameters of the common carotid artery and the systolic and diastolic blood pressures taken by cuff on the brachial artery. The subjects were examined in a lying position. The vascular wall elastic properties were evaluated through the following parameters: compliance coefficient CC, distensibility coefficient DC and stiffness coefficient $\alpha$ [19]. They are formulated as follows:

$$\mathrm{CC} = \frac{\pi\left(D_{\max}^2 - D_{\min}^2\right)}{4(P_s - P_d)}, \tag{1}$$

$$\mathrm{DC} = \frac{D_{\max}^2 - D_{\min}^2}{D_{\min}^2(P_s - P_d)}, \tag{2}$$

$$\alpha = \frac{D_{\min}^2}{(D_{\max}^2 - D_{\min}^2)} \ln\left(\frac{P_s}{P_d}\right), \tag{3}$$

where $D_{\max}$, $D_{\min}$ being the maximum and minimum arterial diameter values for the systolic $P_s$ and diastolic $P_d$ blood pressure respectively.

The intima-media thickness (IMT) was measured simultaneously with the elasticity parameters in the same vessel cross-section. The examinations were performed using the VED system designed by the authors from the Institute of Fundamental Technological Research, Polish Academy of Sciences. The apparatus comprised of a pulse system tracking displacement of vascular wall with measurement precision of up to 7 µm. The inner diameter was determined through digital time measurement between chosen echoes (RF signal) received from the inner vascular wall layer. The frequency of transmitted ultrasound was 6.75 MHz. The wave was focused at 1 to 3 cm below the skin surface. The longitudinal resolution of the apparatus obtained by model examination was 0.33 mm

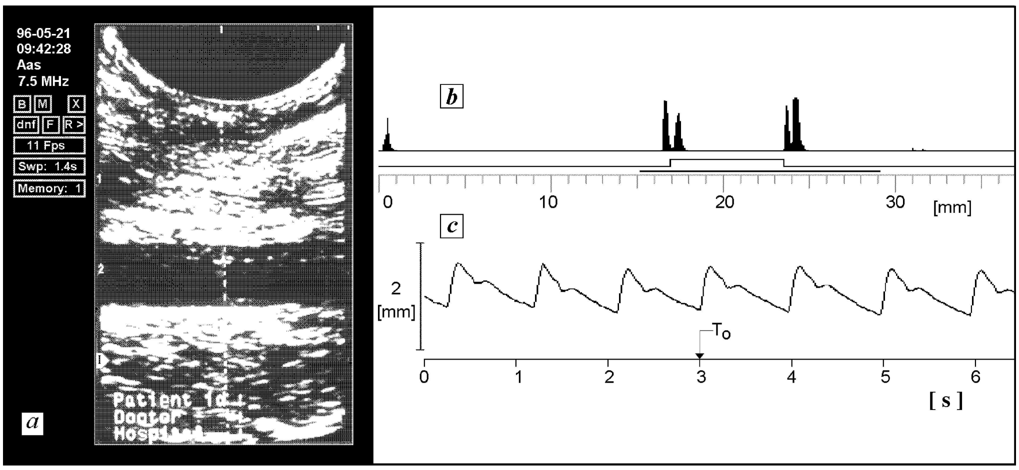


Fig. 1. The longitudinal ultrasound image of the common carotid artery (a) and the data presented in the course of the measurements in the common carotid artery by means VED ultrasonic system: b) echoes from the wall of the artery, c) artery diameter variations. $T_o$ — the time of registering the echoes.

in water. The measured data were displayed on the screen of an IBM PC (Fig. 1) connected on-line with the ultrasonic equipment and stored in the computer memory. The intima-media thickness (IMT) was determined on the basis of the ultrasonic echo image (A-mode) of the arterial wall (Fig. 2).

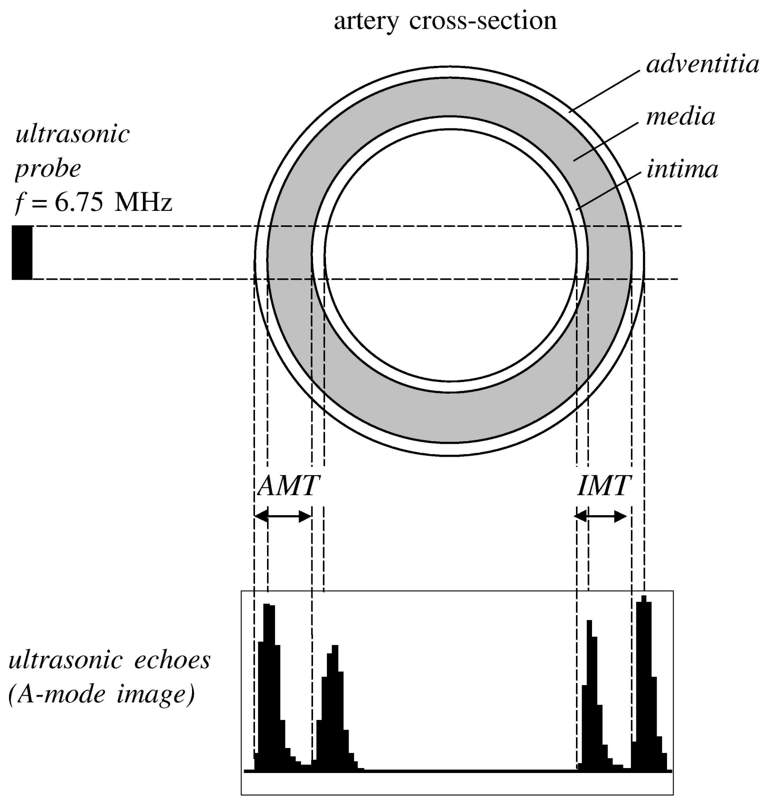


Fig. 2. The method of intima-media thickness (IMT) examination by means of ultrasound.

The common carotid artery wall is composed of three layers: the adventita, media and intima. The basic difficulty in examination of wall thickness is limited longitudinal resolution of ultrasonic systems used for this purpose. For the applied transmission frequency between 5 – 10 MHz the longitudinal resolution is from 0.4 to 0.2 mm. Generally it is not enough to measure the intima thickness which value is less than 0.2 mm [8, 27]. In this situation, the intima-media thickness (IMT) was calculated on the basis of the distance between two successive echoes which correspond to reflection from intima and adventitia layers respectively (Fig. 2). Moreover, the wall thickness changed under the blood pressure change during the cardiac cycle [6, 12, 14]. In VED system for each cardiac cycle 8 echo pictures were recorded synchronously with instantaneous value of artery diameter. The mean value of IMT over cardiac cycle was used for analysis.

The reproducibility of the measurements was tested on a control group of 10 healthy persons: 5 women and 5 men aged 23 to 30. Each person was tested independently by two examiners experienced in such measurements. Coefficient of variation CV was taken as a criterion of reproducibility. It was calculated for every parameter investigated as a ratio of a standard deviation between two compared groups of results to mean value of one of the groups chosen as a reference for a comparative evaluation.

The coefficient of variation CV in examining the intima-media thickness and vascular wall elastic properties was as follows: $11.84 \pm 0.18\%$ for IMT (mean IMT = 0.45 mm), $10.01 \pm 0.13\%$ for stiffness coefficient $\alpha$, $12.85 \pm 0.73\%$ for distensibility coefficient DC and $14.73 \pm 0.14\%$ for compliance coefficient CC measurements.

## 3. Results

The measurements were carried out in the common carotid arteries of 40 persons (19 female, 21 male) aged 22 to 81 (mean age 49.9) of whom 19 were healthy, 3 were suffering from hypertension, 9 were suffering from atherosclerosis and a further 9 from both. The measurements were done while the subjects were lying down, following 15 minute rest periods. Ultrasonic B-mode examinations did not show any stenotic plaque in the common carotid artery where the measurements were taken.

The results, depicted in Fig. 3, show the increase of stiffness coefficient $\alpha$ to be coupled with the increase of intima-media thickness. The distensibility coefficient DC and the compliance coefficient CC decreased as a function of IMT increase. The correlation coefficient $r$ between $\alpha$ and IMT was very high: 0.950 ($p < 0.00001$). It was slightly lower for IMT and DC ($r = -0.839$, $p < 0.00001$). The lowest correlation was for IMT and CC ($r = -0.554$, $p < 0.0002$). Table 1 shows the mean values of measurements in healthy and sick persons respectively.

**Table 1.** The values of parameters measured in the groups of healthy and sick persons.

| Examined group | Age [years] | $P_s$ [mmHg] | $P_d$ [mmHg] | $D_{\min}$ [mm] | IMT [mm] | $\alpha$ | CC [$10^{-7}$ m$^2$/kPa] | DC [$10^{-3}$/kPa] |
|---|---|---|---|---|---|---|---|---|
| healthy persons | 44.0 ±17.9 | 119.7 ±14.3 | 74.2 ±8.0 | 6.78 ±0.80 | 0.57 ±0.08 | 3.31 ±1.19 | 9.75 ±3.52 | 27.64 ±11.20 |
| sick persons | 55.4 ±14.3 | 137.0 ±20.7 | 77.1 ±13.3 | 8.48 ±1.31 | 0.73 ±0.12 | 5.39 ±1.55 | 8.42 ±3.37 | 15.19 ±5.74 |

The results show a significant dependence between the increase of vascular wall stiffness in the common carotid artery and the intima-media thickness. This may be due to the vascular wall structural changes bringing about an increase in both its thickness and stiffness. The increase of vascular wall stiffness is mostly explained in terms of an increase of collagen fibres in the wall and an increase in the ratio of collagen fibres to elastin fibres [7].

The authors wanted to find out how the stiffness coefficient $\alpha$ and intima-media thickness are related to the age of examined persons. The analysis was carried out for the groups of healthy and sick persons described above. The results are shown in Fig. 3. In the healthy group the increase of $\alpha$ and IMT values as a function of age was very significant

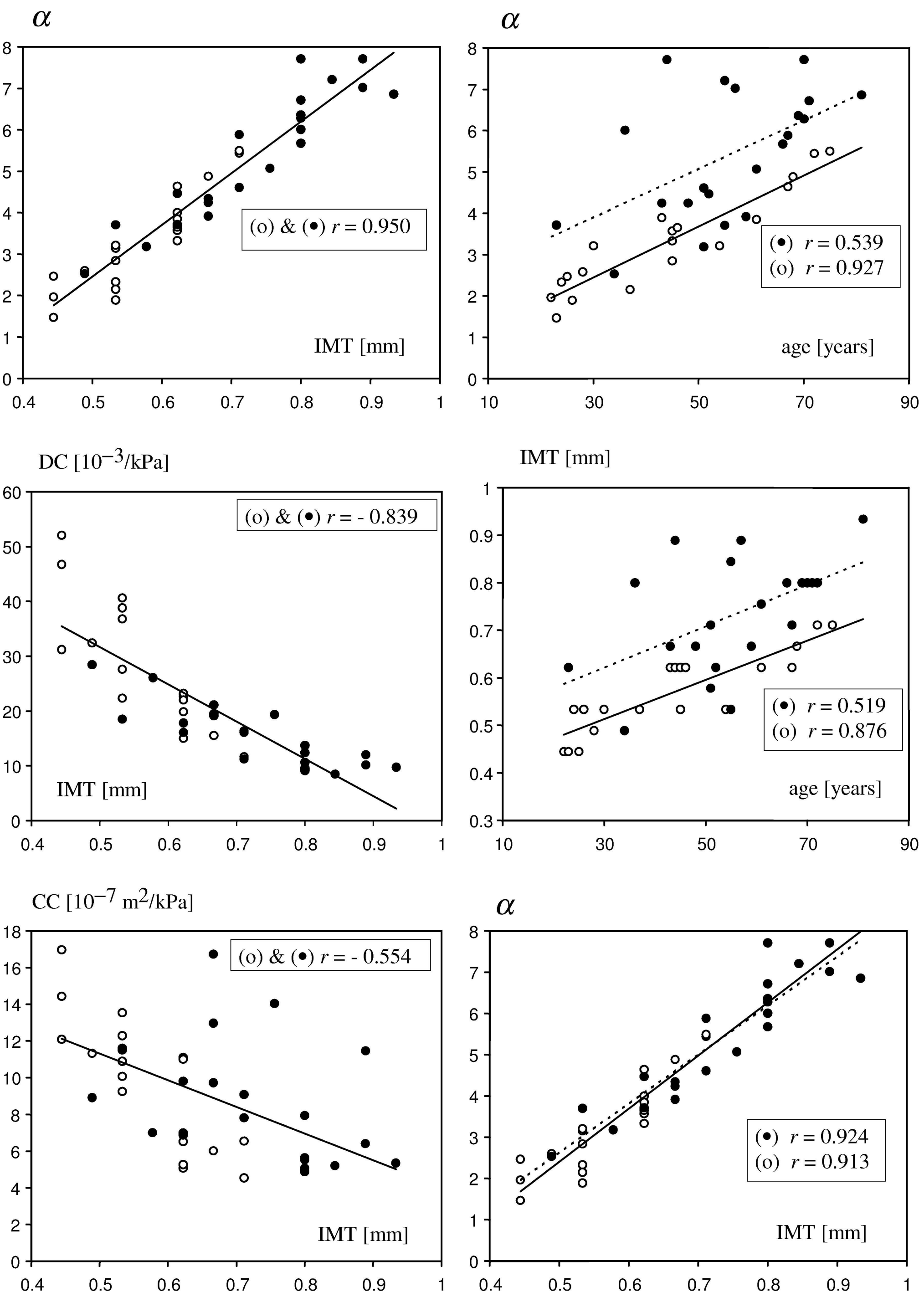


Fig. 3. The intima-media thickness IMT, compliance coefficient CC, distensibility coefficient DC and stiffness coefficient $\alpha$ determined in common carotid artery for healthy (○) and sick (•) persons.

(the correlation coefficients were $r = 0.972$ and 0.876 respectively, $p < 0.00001$). In the sick persons the dependence was very weak with the respective values of the correlation coefficient being $r = 0.539$ and $r = 0.519$ ($p < 0.02$). This means that the structural changes that occur in the vascular wall as a result of disease overshadow the symptoms of ageing. Nevertheless, the very high correlation between the value of $\alpha$ and the IMT for both groups is worth emphasising (the correlation coefficients were $r = 0.913$ and $r = 0.924$ for the healthy and sick group respectively, $p < 0.00001$).

Finally, it should be pointed out that the IMT correlates with the stiffness coefficient $\alpha$ to a much greater degree than with the distensibility and compliance coefficients DC and CC. This may be due to DC and CC being linked to the blood pressure value. Experimental studies performed on large arterial vessels (the aorta, the common carotid artery and the femoral artery) by Bergel [3, 4], Loon *et al.* [18], Simon *et al.* [24], Langewouters et al. [16] and Hayashi *et al.* [13] indicate that the reaction of the artery wall to a change in blood pressure is nonlinear. This means that the coefficients CC and DC described by formulae (1) and (2) depend on the blood pressure, making it difficult to comparatively evaluate the arterial wall elasticity studies performed on their basis. It is necessary to note that the values of coefficients CC and DC are most commonly used in the literature for evaluation of elasticity of arterial wall. The stiffness coefficient $\alpha$ was developed by Powałowski and Peńsko [19] on the basis of the nonlinear function between cross-sectional area of the artery and the blood pressure. Powałowski *et al.* show that the coefficient $\alpha$ is independent of the systolic blood pressure changes [20, 21].

## 4. Conclusions

The measurements carried out in the common carotid arteries of healthy and sick persons point to a statistically evident correlation between the increase of the wall stiffness and the increase of the intima-media thickness. The highest correlation with the wall thickness increase was observed for the stiffness coefficient $\alpha$ ($r = 0.950$, $p < 0.00001$) and the lowest for the compliance coefficient CC ($r = -0.554$, $p < 0.0002$). In persons suffering from hypertension and/or atherosclerosis an observed increase of stiffness coefficient $\alpha$ and intima-media thickness (IMT) was significant in comparison to healthy persons ($p < 0.001$).

## References

[1] G. Belcaro, G. Laurora, M.R. Cesarone, M.T. de Sanctis, S. Renton and L.C. Chong, *Evaluation of arteriosclerosis progression with ultrasonic biopsy and intima-media thickness measurements*, VASA, **22**, 1, 15–21 (1993).

[2] A. Benetos, S. Laurent, A.P. Hoeks, P.H. Boutouyrie and M.E. Safar, *Arterial alterations with aging and high blood pressure*, Arterioscl. and Thromb., **13**, 90–97 (1993).

[3] D.H. Bergel, *The dynamic elastic properties of the arterial wall*, J. Physiol., **156**, 458–469 (1961).

[4] D.H. Bergel, *The static elastic properties of the arterial wall*, J. Physiol., **156**, 445–457 (1961).

[5] M.L. Bots, A. Hofman, A.M. de Bruyn, P. de Jong and D.E. Grobbee, *Isolated systolic hypertension and vessel wall thickness of the carotid artery*, The Rotterdam Elderly Study, Arteriosclerosis and Thrombosis, **13**, 64–69 (1993).

[6] A.M. Brant, S.S. Shah, V.G.J. Rodgers, J. Hoffmeister, I.M. Herman, R.L. Kormos and H.S. Borovetz, *Biomechanics of the arterial wall under simulated flow conditions*, J. Biomechanics, **21**, 2, 107–113 (1988).

[7] P.B. Dobrin, *Mechanical properties of arteries*, Physiol Rev., **58**, 397–460 (1978).

[8] G. Gamble, B. Beaumont, H. Smith, J. Zorn, G. Sanders M. Merrilees, S. Macmahon and N. Sharpe, *B-mode ultrasound images of the carotid artery wall, correlation of ultrasound with histological measurements*, Atherosclerosis, **102**, 163–173 (1993).

[9] P. Guarini, C. Tedeschi, G. Giordano, V. Messina, A.M. Cicatiello and L. Strollo, *Effects of hypertension on intimal-medial thickness, left ventricular mass and aortic distensibility*, International Angiology, **13**, 4, 317–322 (1994).

[10] N. Handa, M. Matsumoto and H. Maeda, *Ultrasonic evaluation of early carotid atherosclerosis*, Stroke, **21**, 1567–1572 (1990).

[11] F. Hansen, P. Mangell, B. Sonesson and T. Lanne, *Diameter and compliance in the human common carotid artery-variation with age and sex*, Ultrasound in Med. & Biol., **21**, 1, 1–9 (1995).

[12] H. Hasegawa, M. Ozawa, H. Kanai, N. Hoshimiya, N. Chubachi and Y. Koiwa, *Evaluation of elastic property of the arterial wall by measuring small velocity signals using ultrasound*, Proc. IEEE Ultrasonics Symposium, 1169–1172 (1997).

[13] K. Hayashi, H. Handa, S. Nagasawa, A. Okumura and K. Moritake, *Stiffness and elastic behaviour of human intracranial and extracranial arteries*, J. Biomechanics, **13**, 2, 175–184 (1980).

[14] A. Herment, P. Peronneau and G. Demoment, *Echographic signal processing*, Archives of Acoustics, **9**, 1-2, 121–130 (1984).

[15] T. Kawasaki, S. Sasayama, S. Yagi, T. Asakawa and T. Hiraia, *Non-invasive assessment of the age related changes in stiffness of major branches of the human arteries*, Cardiovascular Research, **21**, 9, 678–687 (1987).

[16] G.J. Langewouters, K.H. Wesseling and W.J. Goedhard, *The static elastic properties of 45 human thoracic and 20 abdominal aortas in vitro and the parameters of a new model*, J. of Biomechanics, **17**, 6, 425–435 (1984).

[17] S. Laurent, B. Caviezel, L. Beck, X. Girerd, E. Billaud, P. Boutouyrie, A. Hoeks and M. Safar, *Carotid artery distensibility and distending pressure in hypertensive humans*, Hypertension, **23**, part 2, 878–883 (1994).

[18] P. Loon, W. Klip and E. Bradley, *Length-force and volume pressure relationships of arteries*, Biorheology, **14**, 181–201 (1977).

[19] T. Powałowski and B. Peńsko, *A noninvasive ultrasonic method for the elasticity evaluation of the carotid arteries and its application in the diagnosis of the cerebro-vascular system*, Archives of Acoustics, **13**, 1-2, 109–126 (1988).

[20] T. Powałowski and Z. Trawiński, *Noninvasive evaluation of the elasticity of common carotid artery wall*, Archives of Acoustics, **19**, 4, 451–465 (1994).

[21] T. Powałowski, Z. Trawiński and M. Żebrowski, *The method and ultrasonic equipment for elasticity examination of the carotid arteries*, Lecture notes of the ICB Seminars Ultrasound in Biomeasurements, Diagnostics and Therapy, Warsaw, September 1994, Ed. ICB, **24**, 156–169 (1995).

[22] R.S. Reneman, T. Van Merode, P. Hick and A.P.G. Hoeks, *Cardiovascular applications of multi-gate pulsed Doppler systems*, Ultrasound in Med. & Biol., **12**, 5, 357–370 (1986).

[23] W.A. Riley, R.W. Barnes, G.W. Evans and G.L. Burke, *Ultrasonic measurement of the elastic modulus of the common carotid artery*, The Atherosclerosis Risk in Communities (ARIC) Study, Stroke, **23**, 952–956 (1992).

[24] B. Simon, A. Kobayashi, D. Strandness and C. Wiederhielm, *Large deformation analysis of the arterial cross-section*, J. of Basic Eng., **93D**, 2 (1971).

[25] T. Van Merode, P.J. Hick, A.P.G. Hoeks, K.H. Rahn and R.S. Reneman, *Carotid artery wall properties in normotensive and borderline hypertensive subjects of various ages*, Ultrasound in Med. & Biol., **14**, 7, 563–569 (1988).

[26] I. Wendelhag, O. Wiklund and J. Wikstrand, *Arterial wall thickness in familial hypercholesterolemia, ultrasound measurement of intima-media thickness in the common carotid artery*, Arteriosclerosis and Thrombosis, **12**, 70–77 (1992).

[27] M. Wong, J. Edelsten, J. Wollman and M.G. Bond, *Ultrasonic-pathological comparison of the human arterial wall. Verification of intima-media thickness*, Arteriosclerosis and Thrombosis, **13**, 482–486 (1993).

ARCHIVES OF ACOUSTICS
**25**, 2, 213–227 (2000)

# PERIODIC CRACK-MODEL OF COMB TRANSDUCERS: EXCITATION OF INTERFACE WAVES

E. DANICKI

Polish Academy of Sciences
Institute of Fundamental Technological Research
(00-049 Warszawa, Świętokrzyska 21, Poland)
e-mail: edanicki@ippt.gov.p

A model for a comb transducer is proposed and analyzed. It is shown that interface waves are generated in the comb-sample contact area. The interface waves are leaky waves that transport acoustic energy along the interface towards the comb edges, where it is eventually converted into surface acoustic waves propagating outside the comb. By including piezoelectric effects in the comb and the sample materials, it is possible to analyze the incident bulk wave generated by embedded metal strips on both sides of the interface. Approximations for the scattered wavefield and the relationship describing the energy transfer along the interface are derived. Numerical examples are presented.

## 1. Introduction

Comb transducers may be used for the generation of finite-amplitude surface acoustic waves in solids [1]. For this purpose, where transducer efficiency is a crucial parameter, an optimization of the structure is badly needed; this requires transducer modelling.

There is not satisfactory theoretical model of combs in literature for this purpose. An existing model [10] exploits weak-coupling assumption between a comb and a sample. Even if this could be somehow realized experimentally allowing Rayleigh wave to propagate unperturbed under the comb, the efficiency of bulk to surface wave transformation would be weak because of strong incident wave reflection at almost stress-free comb-sample interface.

Here, a model is proposed that will help to determine the comb's main parameters as well as the main phenomena that transform an incident bulk wave into surface waves under the comb. It will be shown that this transformation is a by-product [2] of the wave scattering by periodic voids that form between the comb teeth and the sample surface, as shown in Fig. 1(a).

## 2. Description of the model

In the model illustrated in Fig. 1(b), the typically thin voids of the comb are replaced by cracks. To simplify analysis, periodic cracks are assumed with period $\Lambda$ and width

$\Lambda - w$. Because the system is infinite, surface waves cannot propagate along a free surface. Instead, an interface wave [3] (a "crack wave") can exist at the cracked interface between the two solid halfspaces of the comb and the sample. These crack interface waves would be transformed into surface waves at the edges of a real finite comb. This phenomenon is not analyzed here, since we are interested primarily in the transformation phenomenon of the incident wavebeam into an interface wave during its scattering by periodic cracks. The system under consideration is two-dimensional, with infinite cracks in the $z$-direction and a wavefield independent of $z$.

The incident wavebeam is assumed to be finite. This makes it possible to evaluate the crack wave amplitude excited by the incident wavebeam at a position just outside the area of incidence. In a typical comb transducer, the incident wave is generated by a piezoelectric plate transducer placed on the top of comb; the generated wavebeam of roughly uniform amplitude propagates towards the comb-sample interface, as shown in Fig. 1(a). (Naturally, the wavebeam undergoes diffraction as it propagates, so that its exact shape at the comb-substrate interface may deviate from uniformity.)

In this model, the incident wave is generated using the piezoelectric effect. To do this, we include weak piezoelectricity in both of the elastic halfspaces (comb and sample), and embed periodic metal strips on either side of the interface (without disturbing the material mechanical integrity). These strips can be either grounded or connected to an external voltage source in the manner of an ordinary piezoelectric transducer electrode. The other electrode is grounded to the fully metallized interface at $y = 0$, as shown in Fig. 1(b). The strips excite bulk waves in the same way that an ordinary piezoelectric transducer does. Current is also induced in the grounded strips by the local wavefield in the same way as in piezoelectric transducers. This effect will be later exploited to detect the amplitude of the scattered wavefield at a given strip position in either of two halfspaces.

The strips are periodic with the same period $\Lambda$ as the cracks, but have a fairly wide width $w_e$. Therefore, applying a voltage to a series of strips mimics a single wider transducer electrode and thus generates a wider wavebeam. The polarization of the wavebeam can be either longitudinal or shear, depending on the piezoelectricity of the solid halfspaces. Assuming that the $y$-axis is perpendicular to the interface and the strips, and that the $x$-axis lies along the periodic system of cracks and strips, the piezoelectric modulus $e_{22}$ results in the generation of longitudinal normal propagating incident wavebeam, while $e_{26}$ will generate a shear incident wavebeam. The wavenumbers of the longitudinal and shear waves are denoted by $k_l$ and $k_t$, respectively. The grounded strip current will be correspondingly sensitive to either one or the other component of the local wavefield.

In summary, by including piezoelectricity in the comb and sample materials and by embedding periodic strips on either side of the the interface, we are able to 1) generate a normal incident wavebeam of the required width and polarization, and 2) detect the local wavefield on either side of the interface. We are most interested in the detection of the scattered wavefield amplitude at different positions along the periodic system of strips, that is, at different lateral distances from the incident wavebeam. Figure 1(c) presents

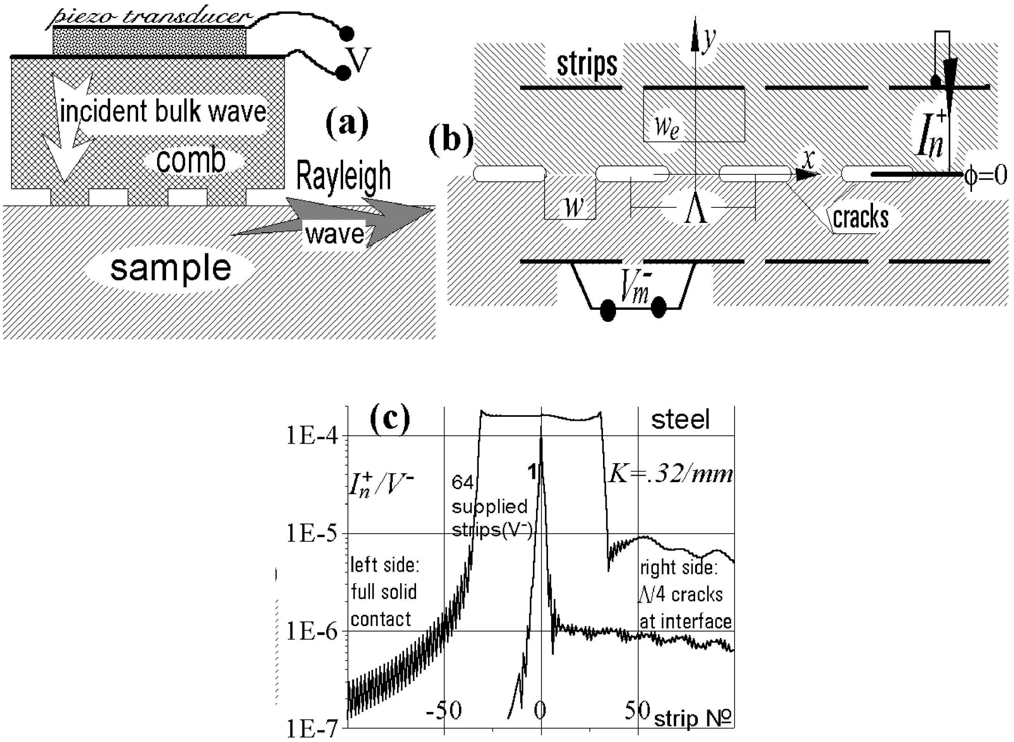


Fig. 1. a) Schematic diagram of a comb transducer with a plate piezoelectric transducer on top, attached to the sample surface. The period of the comb teeth is chosen equal to the wavelength of the generated surface wave. It is assumed that the voids formed between the comb teeth and the sample are thin. b) In the model, voids are modelled by periodic cracks at the interface of two elastic halfspaces (comb and sample). A side effect of this model is that the generated surface wave can propagate in both halfspaces as an entire interfacial wave. Moreover, the system is considered infinite. Mechanical contact between the cracks that model the tooth-sample contact can be either solid or sliding. Weak piezoelectricity of the halfspaces is included. The embedded wide ($\Delta_e = -0.9$) ideal conducting strips on both sides of the interface help to model the generation of a normal incident wavebeam of finite aperture width, and to detect the scattered wavefield in any lateral position with respect to the incident wave. c) Illustration of how the inclusion of piezoelectricity works. One or 64 strips in the lower strip system are supplied with voltage $V^-$ and generate the normal incident wavebeam onto the interface. The currents $I_n^+$ induced in strips on the other side (which is grounded to the interface plane) depend on the strips' lateral position with respect to the incident beam (horizontal axis is the strip number). The current amplitude is shown in a logarithmic scale for two cases: with perfectly contacting halfspaces without cracks (left), and with relatively narrow cracks that do not allow interface waves to exist (right). In both cases, the plots represent typical transmission patterns with limited diffraction effects due to the small distance $2d$ between the embedded strips. The small values of $I^+/V^-$ result from the weak piezoelectric effect assumed: $e_{26} = 1\,\mathrm{Cm}^{-2}$ for generation of a shear incident wave. In all of the figures, both the comb and sample are assumed to be made of steel with the following parameters: $k_t = 0.3097$/mm, $k_l = 0.1695$/mm, and $\rho = 7700\mathrm{kg\,m}^{-3}$ (at $\omega = 10^6\,\mathrm{s}^{-1}$).

examples of how the system works for solid contact between the halfspaces (without cracks), and for certain system of narrow cracks between the halfspaces that does not allow interface waves to propagate. Under these conditions, the figure presents typical diffraction patterns plotted on a log scale; it will be later compared to Fig. 2.

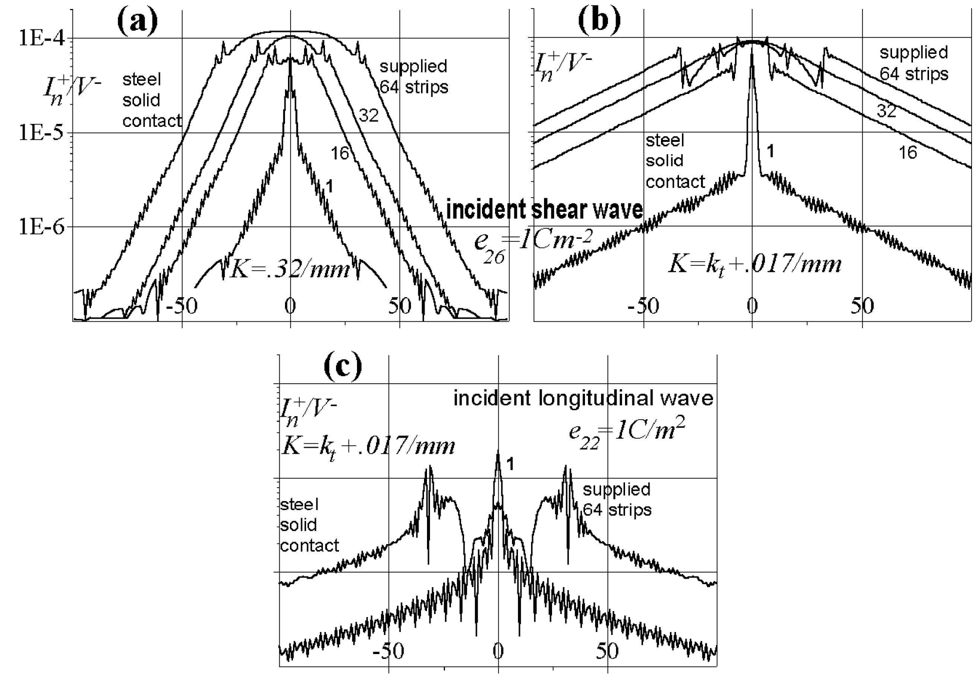


Fig. 2. a) Diffraction pattern for cracks of width $3/4\Lambda$ wide enough for interface waves to exist, for crack period $\Lambda = 2\pi/K$, for comparison with (b) plotted for another crack period. The strong dependence on $K$ suggests a resonant phenomenon of the wave scattering. Three features are worth mentioning with respect to Fig. 1(c): 1) almost the same maximum signal level as for direct, unperturbed transmission by cracks; 2) much wider range of the scattered pattern; and 3) linear slope of the pattern when plotted logarithmically, which shows the exponential decaying phenomenon involved. These all confirm the following interpretation. The incident wavebeam is scattered by cracks and simultaneously an interface leaky wave is generated. This wave propagates along the interface delivering acoustic power to large distances from the area of incidence, and reradiates bulk waves due to a leakage phenomenon. The reradiated bulk waves are detected by strips much farther away from the incident wavebeam than would be possible with pure diffraction phenomenon only. The linear slope confirms that we are indeed dealing with a leaky interface wave, as opposed to scattering of a longitudinal wavebeam ($e_{22}$ =1 $\mathrm{Cm}^{-2}$ applied instead of $e_{26}$) drawn in figure (c), that does not excite interface waves in this system. There is no long range of the scattered wavefield, and no linear slope of the pattern outside the area of incidence. (A small interface wave may still exist, however, which is excited by nonuniformities in the incident wave.)

## 3. Characterization of a layered halfspace

Introducing a potential $\phi$ of the electric field $E_i = -\phi_{,i}$, $i = 1, 2$, the wave-motion of a piezoelectric body is governed by the following system of equations:

$$\begin{aligned} T_{ij} &= c_{ijkl}u_{k,l} + e_{lij}\phi_{,l} \,, \\ D_i &= e_{ijk}u_{j,k} - \epsilon_{ij}\phi_{i,j} \,, \\ \rho u_{i,tt} &= T_{ij,j} \,, \\ D_{i,i} &= 0, \end{aligned} \tag{1}$$

where $T$ is the stress, $D$ is the electric induction, $u$ is the displacement, $c$ is the stiffness tensor of an assumed isotropic body with Lamé constants $\lambda$ and $\mu$, and $\rho$ is the mass density. $e$ and $\epsilon$ are the piezoelectric and dielectric constants. Here, only $e_{222} = e_{22}$ in matrix notation or $e_{212} = e_{26}$ may be assumed different from zero and equal 1 $\mathrm{Cm}^{-2}$, and $\epsilon_{ii}/\epsilon_0$ is set to 10.

In this paper, a time-harmonic field $\exp(j\omega t)$ is considered, so that $\rho u_{i,tt} = -\rho\omega^2 u_i$. Later, if a spatial-harmonic field $\exp(-jpx - jsy)$ is considered, Eqs. (1) can be transformed into Stroh equation [4]

$$\mathbf{H}\,\mathbf{F} = q\,\mathbf{F}, \tag{2}$$

where an eigenvalue $q = s/p$ characterizes the mode dispersion property, in which the polarization is described by an eigenvector $\mathbf{F} = [jpu_i, jp\phi, T_{2l}, D_2]^T$, $i, l = 1, 2$. The matrix $\mathbf{H}$ depends on the material constants and on $\rho\omega^2/p^2$. $\mathbf{H}$ is a $6\times 6$ matrix, because we neglect the wave-field dependence on $z$, as well as $z$-polarized transverse waves. The matrix is real for real $p$.

Solving Eq. (2) for a given spectral variable $p$, one obtains the eigenvalues $q_n$ and wavevector components $(p, s_n)$ of six possible modes $\mathbf{F}^{(n)}$, $n = 1, ..., 6$. Three of the modes ($n = 1, 2, 3$) satisfy the radiation conditions at $y \to \infty$ (the modes either carrying energy into infinity or decaying at $y \to \infty$), and the other three satisfy the corresponding radiation conditions at $y \to -\infty$. These two families of solutions to Eq. (2) will be exploited in constructing the solutions to the wavefields in the elastic halfspaces $y > 0$ and $y < 0$.

In the layered halfspace $y > 0$, the stress $T^+_{2i}$ at $y = +0$ and the surface electric charge is $D^+$ at $y = d$ are both assumed to be known in the form of a harmonic distribution $\exp(-jpx)$ (neglecting harmonic dependence on time) with corresponding complex amplitudes (with notation held unchanged). The superscript "+" denotes the field in the halfspace $y > 0$. Thus the boundary conditions which must be satisfied by the $y$-dependent wavefields are

$$\begin{aligned} T_{2i}(y=0) &= T^+_{2i}, \\ \phi(y=0) &= 0, \\ T_{2i}(y=d-0) &= T_{2i}(y=d+0), \\ u_i(y=d+0) &= u_i(y=d-0), \\ D_2(y=d+0) &- D_2(y=d-0) = D^+, \\ \phi(y=d-0) &= \phi(y=d+0) = \phi^+. \end{aligned} \tag{3}$$

(The second equation makes the interface plane electrically grounded, and the third and fourth equations ensure mechanical integrity across the strips.)

We seek the solution for $u_i(y=+0) = u^+_i$ and $\phi(y=d) = \phi^+$ which also satisfies the radiation conditions at $y \to \infty$ ($s_n = pq_n$):

$$\begin{aligned} y \in (0, d): &\quad \sum_{n=1}^{6} A_n\,\mathbf{F}^{(n)} e^{-js_n y}, \\ y > d: &\quad \sum_{n=1}^{3} B_n\,\mathbf{F}^{(n)} e^{-js_n y}. \end{aligned} \tag{4}$$

Substituting the above expansion into Eqs. (3) and eliminating expansion constants, one obtains

$$\begin{bmatrix} jpu_i^+ \\ jp\phi^+ \end{bmatrix} = \mathbf{G}^+(p) \begin{bmatrix} T_{2j}^+ \\ D^+ \end{bmatrix}, \qquad i,j = 1,2, \tag{5}$$

where the $3 \times 3$ matrix $\mathbf{G}^+$ can be evaluated numerically for any given value of the spectral variable $p$.

Note [4] that for $p$ much larger than the bulk cut-off wavenumber $k_t$, all $q_n$ are complex. Furthermore, the wavefield generated by the applied $T^+$ at $y = 0$, or by $D^+$ at $y = d$, is highly localized at these two planes and thus contributes nothing to the wavefield on the other plane. In conclusion, the value of $G_{33}(p \to \infty)$ is the same as in an infinite body without a boundary at $y = 0$, while $G_{ij}(p \to \infty)$, $i,j = 1,2$ is the same as for an elastic halfspace without the plane of charge at $y = d$. Moreover, the influence between these two planes vanishes at large $p$,

$$\mathbf{G}^+(p \to \infty) = \begin{bmatrix} G_{ij}(\infty) & 0 \\ 0 & G_{33}(\infty) \end{bmatrix}, \qquad i,j = 1,2. \tag{6}$$

In fact, $\mathbf{G}^+(p) \approx \mathbf{G}^+(\infty)$ for $p > p_\infty$, with $p_\infty$ several times larger than $k_t$. This will help to solve the boundary-value problem formulated in the following section. Also note that $\mathbf{G}^+(-\infty) = -\mathbf{G}^+(\infty)$.

The matrix $\mathbf{G}^-(p)$ which describes the relation between $[jpu_i^-, jp\phi^-]^T$ and $[T_{2j}^-, D^-]$ of the halfspace $y < 0$ (with electric charge at $y = -d$) has similar properties. These two matrices, $\mathbf{G}^\pm$, are the planar harmonic Green's functions of the spectral variable $p$. They sufficiently characterize the comb ($y > 0$) and the sample ($y < 0$) halfspaces, with weak piezoelectricity. This relationship will be exploited below in the solution of the boundary-value problem for periodic cracks at the interface between these two halfspaces, and strips embedded at distance $d$ on both sides of the interface $y = 0$.

## 4. Periodic boundary-value problem

We now formulate the above boundary-value problem for arbitrary $p$. Let us first note that $jp\phi$ is a Fourier transform of $E_1 = -\partial\phi/\partial x$. Similarly, $jpu_i$ corresponds to the spatial function $U_i = -\partial u_i/\partial x$. For convenience, the boundary problem is formulated using the above $x$-derivatives instead of the functions themself, in the equations governing the body (Eq. (5)) as well as in the boundary conditions at the plane of strips ($y = \pm d$) and the plane of cracks ($y = 0$):

$$\left.\begin{aligned} E_1^\pm &= 0 \quad \text{on strips}, \quad x \in (-w_e, w_e) \\ D^\pm &= 0 \quad \text{between strips}, \quad x \in (w_e, \Lambda - w_e) \end{aligned}\right\} y = \pm d,$$

$$\left.\begin{aligned} T_{2i}^- = T_{2i}^+ &= 0 \quad \text{on cracks}, \quad x \in (w, \Lambda - w) \\ T_{2i}^- = T_{2i}^+ &= T_{2i} \quad \text{between cracks}, \quad x \in (-w, w) \\ U_i^+ &= U_i^- \quad \text{between cracks}, \quad x \in (-w, w) \end{aligned}\right\} y = 0, \tag{7}$$

for $x$ in one periodic domain. The above equations concern the solid contact between the two halfspaces at the interface $y = 0$. Other simple boundary conditions exist for sliding contact, where $T_{21} = 0$, $x \in (-\Lambda/2, \Lambda/2)$, and the displacement continuity is $U_2^+ = U_2^-$ instead of $U_i^+ = U_i^-, i = 1, 2$ above. (Another simple, albeit nonphysical, case would be $T_{22} = 0$ at the interface and $U_1^+ - U_1^-$ between cracks.)

The first and the last equations in Eqs. (7), stated for the $x$-derivatives of the corresponding wavefields, do not sufficiently describe the boundary conditions at the strips and cracks. (A possible constant difference between $u_i^+$ and $u_i^-$ makes it underdetermined.) The boundary conditions must be appended by conditions for the wavefield evaluated at a single point anywhere in the corresponding domain. These are called the "single-point" conditions, and here the point of $x = 0$ at the center of a strip or a comb tooth is used:

$$\begin{aligned} \int (U_i^+ - U_i^-)\, dx &= \overline{U}_i, \\ -\int E_1^\pm\, dx &= V^\pm. \end{aligned} \tag{8}$$

$\overline{U}_i$ and $V_i^\pm$ are assumed to be known. $V^\pm$ are the strip potentials, and $\overline{U}_i = 0$ ensures the perfect contact of both halfspaces between cracks. Otherwise, the comb teeth would be separated by a constant distance $\overline{U}_i$.

We now introduce a relationship between $U_i = U_i^+ - U_i^-$, $T_{2i}$, $D^\pm$ and $jp\phi^\pm$ in the spectral domain that results from Eq. (5), accounting for $\mathbf{T} = \mathbf{T}^+ = \mathbf{T}^-$ for any $x$ at the interface $y = 0$ $(i, j = 1, 2)$:

$$\begin{gathered} \begin{bmatrix} \mathbf{U} \\ \mathbf{E} \end{bmatrix} = \mathbf{g} \begin{bmatrix} \mathbf{T} \\ \mathbf{D} \end{bmatrix}, \\ \mathbf{g} = \begin{bmatrix} G_{ij}^+ - G_{ij}^- & G_{i3}^+ & -G_{i3}^- \\ G_{3i}^+ & G_{33}^+ & 0 \\ G_{3i}^- & 0 & G_{33}^- \end{bmatrix}, \qquad \mathbf{g}_\infty = \begin{bmatrix} \overline{\mathbf{g}}_\infty & \mathbf{O} \\ \mathbf{O} & \tilde{\mathbf{g}}_\infty \end{bmatrix}, \end{gathered} \tag{9}$$

where $i, j = 1, 2$. In our notation, $\mathbf{E} = [E_1^+, E_1^-]^T$, $\mathbf{D} = [D^+, D^-]^T$, $\mathbf{U} = [U_i]$, $\mathbf{T} = [T_{i2}]$, and $\mathbf{O}$ is a zero matrix. The matrix $\mathbf{g}$, which depends on $p$, assumes the limit $\mathbf{g}_\infty$ at $p \to \infty$. Under certain approximations and for properly chosen, sufficiently large $p_\infty$, we may use $\mathbf{g}(p > p_\infty) = \mathbf{g}_\infty$. Note that $\mathbf{g}(-p_\infty) = -\mathbf{g}(p_\infty)$.

For completeness, an average measure of the wavefield on the strips and between the cracks (that is, on the comb teeth), can be defined as follows:

$$\begin{aligned} \overline{\mathbf{T}} &= \int_{-\Lambda/2}^{\Lambda/2} \mathbf{T}\, dx, \quad \text{where } \mathbf{T} = [T_{i2}^+], \\ \mathbf{I} &= [I^+, I^-]^T = j\omega \int_{-\Lambda/2}^{\Lambda/2} \mathbf{D}\, dx. \end{aligned} \tag{10}$$

The integrations are originally taken over a comb tooth between neighboring cracks or over a strip and then extended into the full period $\Lambda$ accounting for Eqs. (7).

### 5. A method of solution

We now apply the method used in an earlier paper [3] with an extension concerning the electric field [5]. This method is presented here only briefly. First, the wavefield is expanded into a Bloch series (summation over $n$) with its expansion coefficients represented in the so-called BIS expansion [5]

$$\begin{aligned}
\mathbf{T} &= \sum_{n=-\infty}^{\infty}\sum_{m}\mathbf{T}^{(m)}P_{n-m}(\Delta)e^{-j(r+nK)x},\\
\mathbf{U} &= \sum_{n=-\infty}^{\infty}\sum_{m}\mathbf{U}^{(m)}S_{n-m}P_{n-m}(\Delta)e^{-j(r+nK)x},\\
\mathbf{D} &= \sum_{n=-\infty}^{\infty}\sum_{m}\mathbf{D}^{(m)}P_{n-m}(\Delta_e)e^{-j(r+nK)x},\\
\mathbf{E} &= \sum_{n=-\infty}^{\infty}\sum_{m}\mathbf{E}^{(m)}S_{n-m}P_{n-m}(\Delta_e)e^{-j(r+nK)x},
\end{aligned}\tag{11}$$

where $\Delta = \cos Kw$, $\Delta_e = \cos Kw_e$, $S_\nu = 1$ for $\nu \geq 0$ or $-1$ otherwise, and $P_\nu$ is the Legendre function. These expansions satisfy the boundary conditions (7) for any expansion coefficients marked by the superscript "$(m)$".

The summation over $m$ has finite limits $[-M, M+1]$ depending on $K$, $k_t$, and $d$. These limits are set following the general rule that, for certain large $|n| > M$, the system of equations (13) that results should be satisfied automatically for arbitrary $\mathbf{T}^{(0)}$ and $\mathbf{D}^{(0)}$ (within an accepted accuracy [3, 6]). In computations with $K \approx k_t$ and $d \approx \Lambda/2$, we have found that $M = 3$ is satisfactory. In the above expansions, $r$ is limited to one Brillouin zone $r \in (0, K)$; note that all wavefield amplitudes involved in the above equations depend on this reduced spectral variable.

Accounting for the property of $\mathbf{g}_\infty$, we notice that [6]

$$\begin{aligned}
\mathbf{U}^{(m)} &= \overline{\mathbf{g}}_\infty \mathbf{T}^{(m)},\\
\mathbf{E}^{(m)} &= \tilde{\mathbf{g}}_\infty \mathbf{D}^{(m)}.
\end{aligned}\tag{12}$$

Substitution of expansions (11) into Eq. (9) yields for any $n$

$$\sum_m \left[\mathbf{g}_\infty S_{n-m} - \mathbf{g}(r+nK)\right]\begin{bmatrix}\mathbf{T}^{(m)}P_{n-m}(\Delta)\\ \mathbf{D}^{(m)}P_{n-m}(\Delta_e)\end{bmatrix} = 0. \tag{13}$$

This is satisfied automatically for $|n| > M$ provided that $M$ is chosen properly ($M > k_t/K$).

Let us now discuss the first equation of the system (13) concerning the mechanical field $\mathbf{T}$ and $\mathbf{U}$ at the interface. If the systems of strips are embedded deeply inside the halfspace (large $d$), then $G_{i3}^{\pm}$ have significant nonzero values only for such $p = r + nK$ for which the eigenvalues $q$ are real. (Otherwise, the exponential functions in Eq. (4) vanish, preventing any significant influence of the electric charge on the wavefield at the interface.) A real eigenvalue $q_l$ corresponds to a propagating mode $\mathbf{F}^{(l)}$ excited by the strips which is an incident bulk wave onto the crack system. We are interested primarily in normal incidence for which $p \approx 0$ and (if $K$ is not too small) $r \approx 0$. Accounting for the zeros $\mathbf{O}$ in the matrix $\mathbf{g}_\infty$ of Eq. (9), the incident wave is represented by the right hand side of

$$\sum_m \left[\overline{\mathbf{g}}_\infty S_{n-m} - \overline{\mathbf{g}}(r+nK)\right] \mathbf{T}^{(m)} P_{n-m}(\Delta) = \delta_{n0}\tilde{\mathbf{U}}, \tag{14}$$

where $\delta_{ij}$ is a Kroenecker delta. $\tilde{\mathbf{U}} = [G_{i3}^{+}(r+nK), -G_{i3}^{-}(r+nK)]\mathbf{D}_n$ where $\mathbf{D}_n$ is the $n$-th harmonic component of Bloch series (11) and depends indirectly on the voltage applied to the metal strips. It follows from Eq. (5) that $\tilde{\mathbf{U}} = jr[\tilde{u}_i^{+}(r+nK) - \tilde{u}_i^{-}(r+nK)]$ can be considered known, because for weak piezoelectricity $\mathbf{D}_n$ can be evaluated directly from the known strip potentials [5, 6], neglecting the mechanical field. Thus $\tilde{u}_i^{\pm}(r+nK)$ are particle displacements associated with the incident waves generated by either the upper or lower system of strips.

The nontrivial equations in Eq. (13) are those for $-M \le n \le M$. To close the system of equations, we need to account for Eqs. (8), which are

$$\begin{aligned} \sum_m (-1)^m \mathbf{U}^{(m)} P_{-m-r/K}(-\Delta) &= \frac{K}{\pi}\overline{\mathbf{U}} \sin \pi r/K, \\ \sum_m (-1)^m \mathbf{E}^{(m)} P_{-m-r/K}(-\Delta_e) &= \frac{K}{\pi}\mathbf{V} \sin \pi r/K, \end{aligned} \tag{15}$$

where $\mathbf{V} = [V^+, V^-]^T, \overline{\mathbf{U}} = [\overline{U}_i]$. Equations (13) and (15), accounting for (12), allow us to evaluate all of the expansion coefficients in Eqs. (11) and their dependence on $\overline{\mathbf{U}}$ and $\mathbf{V}$.

Finally, substitution of the expansion (11) into Eqs. (10) results in

$$\begin{aligned} \overline{\mathbf{T}} &= \Lambda \sum_m \mathbf{T}^{(m)} P_{-m-r/K}(\Delta), \\ \mathbf{I} &= j\omega\Lambda \sum_m \mathbf{D}^{(m)} P_{-m-r/K}(\Delta_e). \end{aligned} \tag{16}$$

Accounting for Eqs. (15), we obtain

$$\left[\overline{\mathbf{T}}, \mathbf{I}\right]^T = \overline{\mathbf{Y}}(r) \left[\dot{\mathbf{U}}, \mathbf{V}\right]^T \sin \pi r/K. \tag{17}$$

For further convenience, we have introduced the notation $\dot{\mathbf{U}} = j\omega[\overline{U}_i^{+} - \overline{U}_i^{-}]$ which has the physical meaning of the comb tooth velocity relative to the sample, Eq. (8) (Fig. 3). Note that the above solution depends on $r$, a reduced spectral variable whose value is in the domain of one Brillouin zone $(0, K)$: $\overline{\mathbf{Y}}(K-r) = \overline{\mathbf{Y}}(r)$. This results from the symmetry concerning the mode propagation direction. $\dot{\mathbf{U}}$ and $\mathbf{V}$ may also be functions of $r$ in this domain without any change in the above considerations.

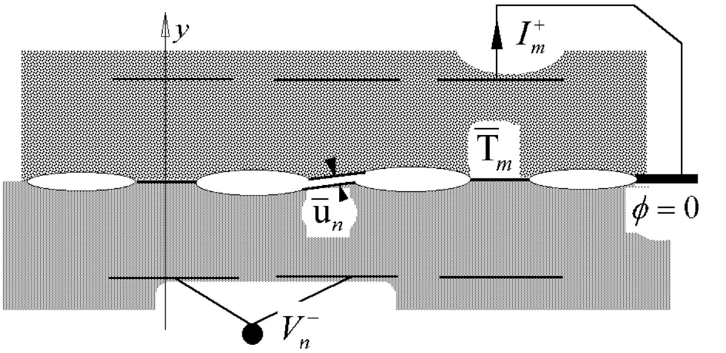


Fig. 3. An interpretation of the transfer relationship, Eq. (19), and the quantities involved. $I_m^{\pm}$ is the current in strip number $m$ excited by the local wavefield at the strip position $x = m\Lambda$, above or below the interface (marked by superscript $\pm$). This wavefield results from the incident wavebeam generated by strip number $n$ to which a voltage $V_n^{\pm}$ is applied relative to the grounded interface $y = 0$; the other strips are grounded. The local wavefield can be also characterized by a force $\overline{\mathbf{T}}_m$ that the comb tooth of number $m$ exerts on the sample surface. An artificial comb tooth displacement $\overline{\mathbf{u}}_n$ with respect to the sample surface may be used to represent the incident wavebeam local amplitude. (This is a quantity that can be evaluated from the known amplitude of incident wavebeam at a given comb tooth.) Note that we may apply only the difference $\overline{u}_i^+ - \overline{u}_i^-$ which is constant over an entire comb tooth (contact area between cracks). The position and the inclination of this area with respect of the interface plane $y = 0$ results from the solution. It is marked in the figure by two parallel bounds of lower and upper halfspaces between cracks, which are somewhat shifted and inclined with respect to $y = 0$ plane.

## 6. Discrete functions

In fact, $\mathbf{V}$ and $\overline{\mathbf{U}}$ are the Fourier transforms of discrete functions which depend on the strip or crack number $l$ along their periodic positions in the systems. In particular, for known strip potentials $\mathbf{v}(l) = [V^+(l), V^-(l)]^T$ and comb tooth displacements with respect to the sample surface $\overline{\mathbf{u}}(l) = [u_i^+ - u_i^-]$ with velocity $\dot{\mathbf{u}} = j\omega\overline{\mathbf{u}}$, the inverse discrete Fourier transforms [7] are defined by

$$\begin{aligned} \mathbf{v}(k) &= K^{-1} \int_0^K \mathbf{V}(r) e^{-jrk\Lambda}\, dr, \\ \dot{\mathbf{u}}(k) &= K^{-1} \int_0^K \dot{\mathbf{U}}(r) e^{-jrk\Lambda}\, dr. \end{aligned} \tag{18}$$

It is evident that $\mathbf{V}(r)$ must be equal to the sum over all strips, $\sum_l \mathbf{v}(l)\exp(jrl\Lambda)$, and similarly $\dot{\mathbf{U}}(r) = \sum_k \dot{\mathbf{u}}(l)\exp(jrl\Lambda)$.

Substitution of the above into Eqs. (17) yields the discrete spatial dependence

$$\begin{aligned} \begin{bmatrix} \overline{\mathbf{T}}(k) \\ \mathbf{I}(k) \end{bmatrix} &= \mathbf{Y}(k-l) \begin{bmatrix} \dot{\mathbf{u}}(l) \\ \mathbf{v}(l) \end{bmatrix}, \\ \mathbf{Y}(m) &= K^{-1} \int_0^K \overline{\mathbf{Y}}(r) e^{-jrm\Lambda} \sin \pi r/K \, dr. \end{aligned} \tag{19}$$

The integrand $\overline{\mathbf{Y}}(r)$ is a regular function, so the evaluation of the above integral can be easily performed using the convenient FFT algorithm.

This relationship has the following interpretation for the natural case of $\dot{\mathbf{u}}(l) = 0$ for all $l$ (Fig. 3). Assume that only one, zeroth strip in the lower system of strips has an applied voltage $v^-(l = 0) = v^-_{l=0}$ (using alternative subscript numbering). It results from Eq. (19) that the currents of this and neighboring strips in this lower, $I^-(k) = I^-_k$, and upper, $I^+_k$ systems of strips are excited in spite of the metallized grounded screening interface $y = 0$. This can only be caused by means of a bulk wavebeam transmitted through the interface, that was excited by the strip. Currents are excited in strips positioned a lateral distance $|l - k|\Lambda$ from the wavebeam.

Figure 1(c) presents the excited currents $I^+_k$ in an example where there are no cracks at the interface (perfect contact between halfspaces), or weakly scattering cracks. It represents simple wavebeam transmission through a small distance $2d$ so that the diffraction effect is small, resulting in almost uniform detected wavebeam. The range $|k - l|\Lambda$ of the detected field is confined to the excited wavebeam width (1 or 64 strip periods in the figure).

In the case of strongly scattering cracks, for instance for wider cracks at the interface as in Fig. 2, the scattered field propagates in all directions and can be detected over a much wider range (that is, by strips of numbers $k$ much different from those with number $l$ to which voltage has been applied). Another phenomenon that causes an excessively wide range of the scattered field will be discussed below.

Equations (19) yields yet another wavefield characteristic, the force $\overline{\mathbf{T}}(k)$ at the interface. Following its definition (10), this is a vector of the full force between two neighboring cracks. Within the model framework of a comb transducer, it corresponds to the total force exerted by a single comb tooth of number $k$ on the sample surface. This force represents the local wavefield at the interface and, when evaluated for different $k$, similar figures can be obtained as discussed above for strip currents. Finally, we note that the assumption of weak piezoelectricity makes the wave scattering by strips negligible.

## 7. The scattered field approximation

It was shown in an earlier paper [3] that there can be leaky interfacial waves guided along the system of cracks. They are attenuated and have complex wavenumber $k_c = K - r_c$ close to $k_t$ for cracks embedded in otherwise homogeneous media. It has also been shown that such waves can be excited by a bulk wave at close to normal incidence, for certain crack wavenumbers $K$ within a narrow range just above $k_t$. Above, we developed a suitable tool for analysis these phenomena, and indeed, they appear in the scattering pattern presented in Figs. 2(a) and (b).

The first striking feature of these plots on a log scale is a linear slope of the wavefield amplitude outside the domain of incidence. This means that the scattered field decays exponentially in the area where there are no propagating incident or reflected wavebeams. Such exponential decay is characteristic of interfacial waves $\exp(-jr_cx)$. The discussed figures must thus present leaky interface waves existing outside the area of incidence.

In the context of this theory, a guided mode in the system is represented by a pole of the integrand of Eq. (19) at $r = r_c$, and the excited amplitude of the mode can be evaluated as a residuum of this integral evaluated on the complex plane $r$.

Here we propose the following approximation to $\overline{\mathbf{Y}}(r)$ at $r \approx r_c \approx 0$ in the case of close to normal incidence:

$$\overline{\mathbf{Y}}(r) = \text{const} + \left\{ \frac{1}{r - r_c} + \frac{1}{(K-r) - r_c} \right\} \mathbf{a} - \left\{ \frac{1}{r + r_c} + \frac{1}{(K-r) + r_c} \right\} \mathbf{a}. \tag{20}$$

The particular form of the above approximation results from the system periodicity, the symmetry with respect to the propagation direction, and the fact that $r$ is the reduced spectral variable with values in one Brillouin zone only, $(0, K)$. The approximation coefficients can be easily found numerically. For instance, $r_c$ is a zero of $1/\overline{Y}_{nn}$ (the matrix diagonal element).

The integration path (19) of the approximated terms is first extended to infinity, then closed in the lower or upper complex halfspaces where the integrands satisfy the Jordan lemma [6]. The residua yield the interfacial components of the scattered wavefield, while the regular parts of integrands contribute only to the localized wavefield within or near the domain of incidence. Example results are plotted in Fig. 4. Here, directly evaluated wavefields from Eq. (19) are presented on the left half of the figure for comparison with the approximated wavefields from Eq. (20) plotted in the right half, for two different

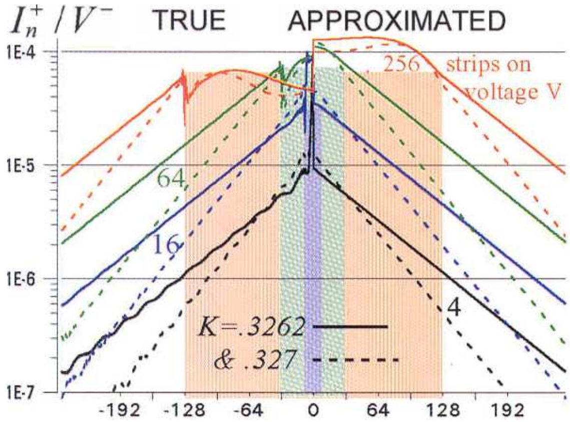


Fig. 4. Comparison of an approximated diffraction pattern form Eq. (20) (right) to that evaluated directly from Eq. (19) (left), for various values of $K$. The transverse incident wave ($e_{26} \neq 0$) and crack width are like those in Fig. 2. The area of incidence is denoted by the shadowed region. The most important wavefield amplitude is that at the edge of incidence, which corresponds to the edge of comb. The field of this amplitude is eventually converted into the surface wave outside the comb. A large range of incident wavebeam aperture widths is presented to show that this edge amplitude value can be obtained with a relatively small incident beamwidth. The fact that the amplitude cannot be made larger by applying a wider wavebeam is reasonable: the excited interface wave displacement amplitude cannot exceed the corresponding amplitude of the incident wave. The most important result presented in this figure is an excellent agreement between the approximated and numerically-evaluated scattering patterns, confirming 1) the validity of the approximation, which makes calculations much easier, and 2) the resonant phenomenon of the analyzed scattering. Indeed, the approximation is based on a singular function in spatial frequency like the singular function of time frequency that describes a typical resonant circuits.

crack wavenumbers $K$ and different aperture widths of the incident wavebeams. Note the quality of the approximation outside the incidence domain. The approximation does not include any directly transmitted or reflected bulk waves and thus is inappropriate for the domain of incidence.

This allows us to make a final interpretation of the examples presented in Figs. 2 and 4. Interface crack waves are excited in the incidence area of a finite wavebeam onto the cracks and propagate at the interface along the crack systems, leaking energy into bulk waves. This wave is detected by strips much farther away from the incident wavebeam. The leakage is caused by the 0-th order Bloch component that is a propagating mode of wavenumber $-r_c = k_c - K$, close to zero. It represents an almost normal outgoing bulk wave that takes away energy from the crack wave, making it leaky and weakly decaying on its propagation path. The further away, the weaker the reradiated bulk wave and the current induced in strips. This exponential decaying yields a linear slope of the scattering pattern plotted in a log scale in the figures.

Two features of Fig. 4 are worth mentioning here. First, the amplitude of the excited interface waves is never greater than a certain limit, even for wider incident wavebeams (corresponding to larger number of teeth in a comb). Second, this maximum amplitude takes place at the edge of the domain of incidence (that is, at the comb edge). In a real, finite comb, the excited interfacial waves will transform into surface waves at the edge of comb (at the boundary between the edge of the transducer and the free undisturbed surface of a sample). Thus from an application point of view, a comb with only the minimum number of teeth to yield the maximum crack wave amplitude at the edge of incident wavebeam is needed.

## 8. The interface wave-field

Equations (19) also suggests the possibility of analyzing interface waves in the system by applying $\dot{\mathbf{u}}_l$ instead of $\mathbf{v}_l$. It follows from Eq. (14) that this may be an indirect way of accounting for the incident wavebeam generated by the strips. Here, we discuss its physical significance.

In the analysis that follows, a close to normal incidence is assumed: $r \approx 0$ and $K > k_t$, which in particular means that only the 0-th order Bloch component represents propagating modes in the system. There are no other propagating modes, nor is there longitudinal-transverse mode conversion during scattering.

Let us start with Eq. (14) taken at $n = 0$ that involves the 0-th order Bloch components of incident, transmitted and reflected waves. Note that both $\overline{\mathbf{g}}(r)$ and $\tilde{\mathbf{U}}$ are proportional to $r$, Eqs. (5) and (9). Thus for small $r$ and accounting for the physically correct condition that $\overline{\mathbf{U}} = 0$, we may rewrite Eqs. (14) for $n = 0$ and the first of Eqs. (15) in form

$$\begin{gathered}
\sum_m S_{-m}\mathbf{U}^{(m)}P_{-m}(\Delta) = \sum_m \overline{\mathbf{g}}(r)\mathbf{T}^{(m)}P_{-m}(\Delta) + \tilde{\mathbf{U}}, \\
\frac{1}{r}\sum_m \left[S_{-m}\mathbf{U}^{(m)}P_{-m}(\Delta) - \frac{r}{K}(-1)^m p_{-m}(-\Delta)\overline{\mathbf{g}}_\infty \mathbf{T}^{(m)}\right] = \overline{\mathbf{U}} = 0,
\end{gathered} \tag{21}$$

where $p_k(\cdot) = \partial_\nu P_{k+\nu}(\cdot)|_{\nu=0}$ and $P_n(-\Delta) = S_n(-1)^n P_n(\Delta)$. Accounting for the finite terms only at $r \to 0$, we obtain

$$\begin{aligned} \sum_m S_{-m}\mathbf{U}^{(m)}P_{-m}(\Delta) \;&=\; 0,\\ \sum_m \left[\{\overline{\mathbf{g}}(r)/r\}_{r\to 0}P_{-m}(\Delta) - (-1)^m \frac{p_{-m}(-\Delta)}{K}\overline{\mathbf{g}}_\infty\right]\mathbf{T}^{(m)} \;&=\; -\{\tilde{\mathbf{U}}/r\}_{r\to 0}. \end{aligned} \tag{22}$$

It results from the last equation that $\overline{\mathbf{U}} = -\{\tilde{\mathbf{U}}/r\}_{r\to 0}$ is an equivalent quantity that can be applied in Eq. (15) to describe the incident wave at the interface.

In summary, for close to normal shear ($t$) or longitudinal ($l$) incident waves, we can evaluate $\dot{\mathbf{U}} = j\omega\overline{\mathbf{U}}$ which appears in Eq. (17) to describe the incident wavebeam in equivalent manner. For example, for a uniform incident wavebeam, $\dot{\mathbf{u}}_l$ involved in Eq. (19) is constant within a limited range of $l$ depending on the wavebeam aperture width. This greatly simplifies the model of comb transducers, because we no longer need to include in the model the piezoelectric plate transducer on the top of comb. We need use only a quarter of Eqs. (19), only that for $\overline{\mathbf{T}}_k$ and $\dot{\mathbf{u}}_l$ in which $\dot{\mathbf{u}}_l$ describes the incident wave at a given comb tooth of number $l$ (assumed uniform over an entire tooth, Fig. 3). $\overline{\mathbf{T}}_k$ is the resulting force exerted by the comb tooth of number $k$ on the sample surface. In the applied notation, $-\mathrm{Re}\{\sum_l \overline{\mathbf{T}}_l\dot{\mathbf{u}}_l^*\}/2$ is the delivered power by the incident wavebeam.

## 9. Conclusions

In this paper, we have analyzed a somewhat elaborate system to show that resonant generation of interface waves takes place when a bulk wave at close to normal incidence is scattered by periodic cracks with certain parameters. The phenomenon was shown to be governed by a transfer function $\mathbf{Y}$ whose spectral form has a pole in a wavenumber domain (also called the spatial frequency domain). This is analogous to a pole in the frequency domain of an ordinary resonant electric circuit. The phenomenon it describes is the resonance in the spatial domain, with a periodic force caused by periodic contact between the comb and the sample halfspaces.

The spatial transfer function $\mathbf{Y}(m)$, Eq. (19), yields a powerful tool for analysis of variety of comb transducers. It can be directly applied, for instance, in analysis of a "special comb" proposed recently [11], where each comb teeth are excited with different phases, like in the case of obligue incidence of bulk wave onto the comb-sample interface. This encourages us to develop the introduced and presented here approach into a full comb transducer model.

Numerical examples have been presented for cracks embedded in otherwise homogeneous media. However, similar results can be obtained within the presented general theory for cracks at the interface of two different solid halfspaces, with solid or sliding contact between cracks. These results fully confirm the main thesis of this and a previous paper [3] about the resonant scattering of close to normal incident waves by cracks. Yet another generalization of the presented theory can be made by applying it to a multiperiodic system of cracks: they will look like periodic combs separated by some distance, each one with several teeth [8]. Another generalization is for oblique incidence, which is a 3-dimensional problem [9].

Future plans include applying this theory to the detailed investigation of comb transducers, for instance the frequency and time responses of the comb, the optimization of comb material for a given sample material, the number of teeth, and so forth.

## Acknowledgements

Financial support was provided by the Polish-US Maria Skłodowska Curie Joint Fund II under Grant No. PAN/NIST-97-300. The author gratefully acknowledges helpful discussion with Dr. Donna C. Hurley at the National Institute of Standards and Technology and kind assistance in the preparation of this manuscript during her visit in the Institute of Fundamental Technological Problems earlier this year. This paper was originally submitted to The Journal of the Acoustical Society of America in April 1999 (and withdrawn in May 2000 because of unbearable slow peer-review process giving no chance of publication before the end on the above mentioned Grant). There are special thanks to its Associate Editor Prof. Dale Chimenti and to anonymous reviewers for comments concerning relevant literature that improved the text: the second paragraphs of Introduction and of Conclusions, and corresponding references result from these comments. (The last reference appeared after the paper submission; the peer-review delay made it possible to include this reference.)

## References

[1] D.C. Hurley, *Nonlinear propagation of narrowband Rayleigh waves excited by a comb transducer*, J. Acoust. Soc. Am. (in press).

[2] E.J. Danicki and D.C. Hurley, *Resonant scattering phenomenon by in-plane periodic cracks*, J. Acoust. Soc. Am., **105**, 1225 (1999), CD-ROM: Collected Papers "Berlin 99", ISBN 3-9804568-5-4.

[3] E.J. Danicki *Resonant phenomena in bulk-wave scattering by in-plane periodic cracks*, J. Acoust. Soc. Am., **105**, 84–92 (1999).

[4] E.J. Danicki, *An approximation to the planar harmonic Green's function at branch points in wave-number domain*, J. Acoust. Soc. Am., **104**, 651–663 (1998).

[5] K. Bløtekjær, K.A. Ingebrigtsen and H. Skeie, *A method for analyzing waves in structures consisting of metal strips on dispersive media*, IEEE Trans. Electron Devices, **20**, 1133–1138 (1973).

[6] E. Danicki, *Excitation, waveguiding and scattering of EM and elastic waves by a system of in-plane strips or cracks*, Arch. Mech., **46**, 123–149 (1994).

[7] E.I. Jury, *Theory and application of the $\mathcal{Z}$-transform method*, Wiley, New York 1964.

[8] E. Danicki, *Spatial spectrum of electric charge on planar array of metal strips*, Electr. Lett., **31**, 2220–2221 (1995).

[9] E. Danicki, *Bending of a layered isotropic plate with periodic disbondings*, ASME J. Appl. Mech., **61**, 612–617 (1994).

[10] J.L. Rose, S.P. Pelts and M.J. Quarry, *A comb transducer model for guided wave NDE*, Ultrasonics, **36**, 163–169 (1998).

[11] J.L. Rose and S.P. Pelts, *A comb transducer model for guided wave mode control*, Review of Progress in Quantitative Nondestructive Evaluation, **18**, 1029–1037 (1999).

ARCHIVES OF ACOUSTICS
**25**, 2, 229–233 (2000)

# ACOUSTO-OPTIC PROPERTIES OF PIEZOELECTRIC INTERFACIAL WAVES

W. LAPRUS

Polish Academy of Sciences
Institute of Fundamental Technological Research
(00-049 Warszawa, Świętokrzyska 21, Poland)
e-mail: wlaprus@ippt.gov.p

An analysis is given of acousto-optic coupling associated with piezoelectric interfacial waves for a great number of crystal cuts. Results of numerical calculations are presented of appropriate coupling coefficients in relation to wave parameters for lithium niobate and quartz. It is found that, for some cuts, the coefficients are quite large (over 4% for lithium niobate). It is also found that high acousto-optic coupling is usually accompanied by high piezoelectric coupling.

## 1. Introduction

The acousto-optic effect is used in many electronic devices with surface acoustic wave, e.g. in deflectors or travelling diffraction gratings. Replacing the surface acoustic wave (SAW) by the piezoelectric interfacial wave (PIW) in such devices is attractive for two reasons. First, piezoelectric coupling of PIW is roughly two times greater than that of SAW. So, generation of PIW is easier and strain of the medium is higher, which should translate into higer acousto-optic coupling. Second, since PIW propagates inside the medium, it is less affected by the environment.

In the paper, we investigate the acousto-optic coupling of PIW for two piezoelectric media which differ much in acousto-optic properties: lithium niobate and quartz. A numerical survey of the two media is made for a great number of crystal cuts. PIW parameters and acousto-optic coupling coefficients are calculated for each cut. Then crystal cuts of high coupling (piezoelectic and/or acousto-optic) are selected.

## 2. Wave properties

PIW is a surface wave which propagates along a perfectly conducting plane embedded in a homogeneous piezoelectric medium. In the system of coordinates $(x, y, z)$, let the plane be given by the equation $z = 0$. We assume that the electro-mechanical field depends on time as $\exp(j\omega t)$, that it is independent of $y$ (the wave propagates in the $x$ direction), and that the dependence on $x$ is given by the factor $\exp(-j\omega r x)$ where $r$

is the slowness of the wave. In this case, the electro-mechanical field equations can be reduced to a system of eight first-order ordinary differential equations, as described in Ref. [1].

Let $i, j = 1, 2, 3$ and $(x_i) = (x, y, z)$. The following field variables will be used: particle displacement $u_i$, electric potential $\phi$, surface force $T_i = T_{3i}$ (where $T_{ij}$ is the stress tensor), and normal (to the conducting plane) component $D_3$ of the electric displacement $D_i$. We have

$$\frac{d}{dz} F_K = -j\omega r H_{KL}(r) F_L, \tag{1}$$

where $K, L = 1, \ldots, 8$ and $(F_K) = (j\omega r u_i, j\omega r \phi, T_i, D_3)$. We adopt notations and conventions of Ref. [1], in particular, the convention of summing over repeated indices. For real $r$, which we assume, the matrix $H_{KL}$ is real and non-symmetric. It depends on material constants: elastic tensor $c_{ijkl}$, piezoelectric tensor $e_{kij}$, dielectric tensor $\varepsilon_{ki}$, and mass density $\rho$.

The solution to Eq. (1), which satisfies appropriate boundary conditions at the conducting plane, can be obtained by assuming that it depends on $z$ as $\exp(-j\omega s z)$ where $s$ is the slowness of the wave in the $z$ direction. This leads to the system of eight linear algebraic equations

$$H_{KL}(r) F_L = q F_K \,, \tag{2}$$

where $q = s/r$. After solving the eigenvalue problem defined by Eq. (2) we find the solution, separately in the upper and lower half-space, as a linear combination of four eigenwaves with coefficients determined by the boundary conditions [1]. At the conducting plane, the amplitude of the solution $F_K$ is a linear combination of four eigenvectors.

## 3. Acousto-optic coupling

Let us introduce the tensor $\eta_{ij} = \varepsilon_0 \varepsilon_{ij}^{-1}$, where $\varepsilon_{ij}^{-1}$ denotes the inverse of the matrix $\varepsilon_{ij}$ and $\varepsilon_0$ is the dielectric permittivity of the vacuum. The relation between the electric field and the electric displacement is

$$E_i = \varepsilon_0^{-1} \eta_{ij} D_j \,. \tag{3}$$

The acousto-optic effect consists in changing the tensor $\eta_{ij}$ due to strain of the medium. This is usually denoted by

$$\Delta\eta_{ij} = \eta_{ij}(1) - \eta_{ij}(0). \tag{4}$$

The argument 0 or 1 means that the strain is equal to zero or is different from zero. The tensor $\zeta_{ij} = \Delta\eta_{ij}$ is proportional to the strain tensor [2, 3], i.e.

$$\zeta_{ij} = p_{ijkl} S_{kl} \,, \tag{5}$$

for $k, l = 1, 2, 3$, where $S_{kl}$ is the strain tensor and $p_{ijkl}$ is the acousto-optic tensor.

Mutiplying Eq. (4) by $\varepsilon_0^{-1} D_j$ we get

$$E_i(1) - E_i(0) = \varepsilon_0^{-1} \zeta_{ij} D_j \,. \tag{6}$$

Denote by $|E_i|$ the length of the vector $E_i$. The ratio

$$\frac{|E_i(1) - E_i(0)|}{|E_i(0)|} = \frac{|\zeta_{ij} D_j|}{|\eta_{ij}(0) D_j|} \tag{7}$$

is the relative change of the length of $E_i$ due to strain for a particular electric displacement $D_j$. It is obvious that this ratio is independent of the the length of $D_j$. If the vector $D_j$ is parallel to the $x$ axis then we may put $(D_j) = (1, 0, 0)$ in Eq. (7). This gives

$$\alpha_1 = |\zeta_{i1}|/|\eta_{i1}(0)|, \tag{8}$$

which will be called acousto-optic coupling coefficient in the $x$ direction. In general,

$$\alpha_j = |\zeta_{i(j)}|/|\eta_{i(j)}(0)| \tag{9}$$

will be called acousto-optic coupling coeficients in the $x$, $y$, and $z$ direction (for $j = 1, 2, 3$). The coefficient $\alpha = \alpha_1 + \alpha_2 + \alpha_3$ is an overall measure of acousto-optic coupling.

We assume that the acousto-optic coupling does not affect essentially the propagation of the surface wave. So, in the above formulae, by $E_i$ and $D_i$ we mean the fields other than those of the surface wave.

In order to calculate the tensor $\zeta_{ij}$ and then the acousto-optic coupling coefficients, we need the value of the strain tensor $S_{ij} = \dfrac{1}{2}(u_{i,j} + u_{j,i})$ at the conducting plane. It is seen that

$$u_{i,1} = -j\omega r_{\mathrm{p}} \tilde{u}_i \,, \tag{10}$$

and that $u_{i,2} = 0$. The remaining derivative can be found from Eq. (1). We have

$$u_{i,3} = H_{iL}(r_{\mathrm{p}}) \tilde{F}_L \,. \tag{11}$$

In Eqs. (10), (11), $\tilde{u}_i$ and $\tilde{F}_L$ are the complex amplitudes of $u_i$ and $F_L$ at the conducting plane, $r_{\mathrm{p}}$ is the slowness of PIW.

## 4. Numerical calculations

The complex amplitudes and other parameters of PIW are calculated for various orientations of the conducting plane with respect to the crystallographic axes of the medium and for different directions of propagation. This is done by solving the eigenvalue problem related to Eq. (2) with the use of EISPACK routines [4] for different crystal cuts or triplets of Euler angles. The three-dimensional space of Euler angles is scanned in steps of 2° in each of the three Euler angles (for details see Ref. [1]). Next, for each scanned crystal cut, acousto-optic coupling coefficients of PIW (if it exists) are calculated using Eq. (9).

Two piezoelectrics are investigated in this way: lithium niobate (trigonal *3m* symmetry class) and quartz (trigonal *32* symmetry class). They differ considerably in acousto-optic properties. For both piezoelectrics, the scanning is performed in the ranges of $0° - 30°$, $0° - 180°$, and $0° - 180°$ (first, second, and third Euler angle). In the calculations, $\omega = 10^6 \mathrm{s}^{-1}$. The material constants are taken from Ref. [5], and the acousto-optic tensors are taken from Ref. [3].

**Table 1.** PIW parameters and acousto-optic coupling coefficients for lithium niobate (physical units: A=$10^{-12}$m/$P^{1/2}$ and B=$Nm^{-2}/P^{1/2}$, where P=$10^{-3}$$Wm^{-1}$). Notes. Row 1: $\kappa > 3$. Rows 2–4: $\alpha > 6$. Row 5: $\alpha_1 > 3$. Row 6: $\alpha_2 > 3$. Row 7: $\alpha_3 > 3$.

| Euler angles deg | | | $v_p$ m/s | $\psi$ deg | $\kappa$ % | $\tilde{u}_1$ A | $\tilde{u}_2$ A | $\tilde{u}_3$ A | $\tilde{T}_1$ B | $\tilde{T}_2$ B | $\tilde{T}_3$ B | $\alpha_1$ % | $\alpha_2$ % | $\alpha_3$ % |
|---|---|---|---|---|---|---|---|---|---|---|---|---|---|---|
| 30 | 92 | 164 | 4075 | −2.7 | 3.50 | −2.07 | −69.9 | −0.11 | $-j11.0$ | $j0.52$ | $-j128.$ | 0.33 | 2.99 | 1.77 |
| 10 | 106 | 128 | 3917 | −8.6 | 0.65 | −15.3 | 25.0 | 29.8 | $-j542.$ | $j10.6$ | $-j286.$ | 4.28 | 1.24 | 1.69 |
| 20 | 96 | 132 | 3952 | −8.2 | 0.65 | −12.1 | 34.6 | 20.7 | $-j379.$ | $j14.0$ | $-j244.$ | 2.07 | 2.27 | 2.14 |
| 30 | 46 | 62 | 3982 | −3.0 | 0.45 | −14.8 | 2.88 | −39.0 | $j739.$ | $-j13.5$ | $-j281.$ | 0.41 | 0.62 | 4.99 |
| 20 | 100 | 132 | 3971 | −5.9 | 0.60 | −11.0 | 38.2 | 14.8 | $-j291.$ | $j5.49$ | $-j231.$ | 3.36 | 2.03 | 1.93 |
| 30 | 90 | 164 | 4074 | −2.7 | 3.45 | −2.11 | −70.2 | 0.00 | $-j0.01$ | $j0.00$ | $-j129.$ | 0.34 | 3.02 | 1.79 |
| 20 | 44 | 70 | 3980 | −3.8 | 0.45 | −14.3 | 7.75 | −38.9 | $j740.$ | $-j14.0$ | $-j274.$ | 0.42 | 0.71 | 3.98 |

**Table 2.** PIW parameters and acousto-optic coupling coefficients for quartz (physical units: A=$10^{-12}$ m/$P^{1/2}$ and B=$Nm^{-2}/P^{1/2}$, where P=$10^{-3}$ $Wm^{-1}$). Notes. Rows 1–2: $\kappa > 0.04$. Rows 3–4: $\alpha > 0.03$.

| Euler angles deg | | | $v_p$ m/s | $\psi$ deg | $\kappa$ % | $\tilde{u}_1$ A | $\tilde{u}_2$ A | $\tilde{u}_3$ A | $\tilde{T}_1$ B | $\tilde{T}_2$ B | $\tilde{T}_3$ B | $\alpha_1$ % | $\alpha_2$ % | $\alpha_3$ % |
|---|---|---|---|---|---|---|---|---|---|---|---|---|---|---|
| 20 | 134 | 154 | 3388 | −10 | 0.04 | −0.95 | −44.0 | 21.5 | $-j193.$ | $j40.8$ | $j75.1$ | 0.00 | 0.01 | 0.00 |
| 30 | 90 | 160 | 3410 | −10 | 0.05 | 0.00 | 0.00 | 47.3 | $-j421.$ | $j83.4$ | $j0.00$ | 0.00 | 0.01 | 0.00 |
| 30 | 84 | 156 | 3362 | −10 | 0.02 | 0.59 | 5.28 | 29.5 | $-j263.$ | $j47.9$ | $-j3.29$ | 0.00 | 0.05 | 0.00 |
| 30 | 90 | 154 | 3341 | −8.4 | 0.01 | 0.00 | 0.00 | 23.2 | $-j205.$ | $j28.9$ | $j0.00$ | 0.00 | 0.05 | 0.00 |

The results are presented in Tables 1 and 2. The tables give PIW parameters and acousto-optic coupling coefficients for several crystal cuts selected from tens of thousands of cuts where PIW exists. Each cut is representative of a group of cuts (see the notes to the tables).

The following parameters are given: phase velocity $v_{\rm p} = 1/r_{\rm p}$, beam steering angle $\psi$, piezoelectric coupling coefficient $\kappa$, normalized complex amplitudes of $u_i$ and $T_i$ at the conducting plane, acousto-optic coupling coefficients.

## 5. Conclusion

In the angle space, domains of high acousto-optic coupling are different from domains of high piezoelectric coupling, as can be seen from Table 2. Nevertheless, the two kinds of domains overlap partially so that there are domains where both the couplings are relatively high. (Domains of high piezoelectric coupling for quartz can be seen in Refs. [6] and [7] in the form of maps.)

Acousto-optic coupling coefficients for lithium niobate, which can be as large as 5%, are greater that those for quartz by two orders of magnitude. It is interesting to note that, for lithium niobate, cuts of high piezoelectric coupling (rows 1 and 6 of Table 1) are characteristic of large $\alpha_2$ which is the greatest of the three coefficients $\alpha_i$. This is even more conspicuous in the case of quartz: $\alpha_1$ and $\alpha_3$ are less than 0.01% for every crystal cut (Table 2 gives just four examples).

In the case of lithium niobate, there is a great freedom of choosing such a crystal cut that one of the coefficients $\alpha_i$ is greater than the other two (Table 1: row 2 for $\alpha_1$, rows 1 and 6 for $\alpha_2$, rows 4 and 7 for $\alpha_3$). It is seen no correlation between the coefficients $\alpha_i$ and the amplitudes $\tilde{u}_i$ and $\tilde{T}_i$.

## Acknowledgment

This work was supported by Committee of Scientific Research (Poland) under Grant No. 2 P03B 171 12.

## References

[1] W. Laprus and E. Danicki, *Piezoelectric interfacial waves in lithium niobate and other crystals*, J. Appl. Phys., **81**, 855–861 (1997).

[2] J. Sapriel, *Acousto-optics*, Wiley, New York 1976.

[3] A. Yariv and P. Yeh, *Optical waves in crystals*, Wiley, New York 1984.

[4] B.T. Smith, J.M. Boyle, B.S. Garbow, Y. Ikebe, V.C. Klema and C.B. Moler, *Matrix eigensystem routines — EISPACK Guide*, Lecture Notes in Computer Science, **6**, 149–258 (1974).

[5] J.G. Gualtieri, J.K. Kosinski and A. Ballato, *Piezoelectric materials for SAW applications*, IEEE Trans. Ultrason. Ferroel. Freq. Control, **41**, 53–59 (1994).

[6] E. Danicki and W. Laprus, *Piezoelectric interfacial waves in langasite and dilithium tetraborate*, Archives of Acoustics, **21**, 99–107 (1996).

[7] www.ippt.gov.pl/˜wlaprus.

ARCHIVES OF ACOUSTICS
**25**, 2, 235–249 (2000)

# RELATIONS BETWEEN LOSSES IN PIEZOELECTRIC CERAMIC AND THE MAGNITUDE OF ITS VIBRATION LEVEL

M. SZALEWSKI

Polish Academy of Sciences
Institute of Fundamental Technological Research
(00-049 Warszawa, Świętokrzyska 21, Poland)
e-mail: mszalew@ippt.gov.pl

In the paper the method of the mechanical and electrical loss measurements using a piezoelectric transformer has been applied to determine the relations between the losses and the magnitude of the vibration velocity, strain and stress. The measurements and calculations have been realized for the soft and hard PZT-type ceramics. Good accordance of the obtained results with the results obtained by the other authors, applying different measurement methods, proves the usability of the method of loss measurements proposed by the author.

## 1. Introduction

Modified with various additives piezoelectric ceramic with the basic composition $\mathrm{Pb(Zr_xTi_{1-x})O_3}$ is widely used in the piezoelectronics [5]. Recently the quantity of its applications in high power devices (ultrasonic transducers, piezoelectric transformers, piezoelectric motors, translators, actuators) has increased considerably. The ceramic in these devices is excited by high electric fields to mechanical vibrations with high amplitude. As yet there is no complete and exact description of the domain phenomena that cause the large increase of losses and changes of material constants of ceramics in high fields. The kinetics and the physical mechanism of processes that occur in polycrystalline ferroelectrics in high external fields are very complicated and they have not been completely investigated [9, 13, 16, 23]. Recently good results have been obtained by the authors applying the Rayleigh law (originally discovered for ferromagnetic materials) to the description of the domain phenomena in a piezoelectric ceramic [4, 6, 17, 29]. In the high fields range the nonlinear effects [8, 26, 28] make impossible to apply standard methods of loss measurements. The threshold electric field for the occurence of nonlinearity depends on the conditions of the operation of the piezoelectric ceramic. Stresses induced in the piezoceramic resonator under resonant mode conditions cause that the threshold electric field is much lower than under off resonant conditions [26].

In the previous paper [24] we have proposed the method of the determination of electrical and mechanical losses applying the measurements of voltage ratios in a piezoelectric transformer instead of the measurements of resonator quality factors. The results of the measurements of losses as a function of input electric field have been presented. The magnitude of the output mechanical signal is very important for designers and users of piezoelectric elements. Therefore results of investigations of ceramic properties and measurements of losses are presented most often as a function of vibration velocity [22, 25, 30, 31] or induced stresses [26]. The method of loss measurements applied by the author is shortly recalled in Sec. 2. In Sec. 3 the results of the measurements of the changes of ceramic material constants with the increasing electric field are presented. They are necessary for subsequent calculations. Ceramic material constants were measured using standard methods [1, 3, 7]. The results of the calculations of the magnitude of the vibration velocity, mechanical stress and strain induced in the transformer are presented in Sec. 4 as a function of driving electric field. The relations between the magnitude of electrical and mechanical losses in the piezoelectric ceramic and above mentioned mechanical quantities are presented in Sec. 5. The losses have been measured and calculated using the method described in [24] and recalled in Sec. 2.

## 2. Application of a piezoelectric transformer to loss measurements

Various designs of piezoelectric transformers are known, with various polarizations of individual parts and with various shapes, e.g. [12, 21, 32]. For the loss measurements we applied a ring-shaped piezoceramic transformer with the electrodes divided with the ratio 1:1 [24]. The thickness and width of a ring were small in comparison with its radius. Such a shape has an important advantage — the stress and strain distribution is uniform in the whole ring. The piezoelectric ceramic was poled along the thickness direction. One pair of vacuum evaporated silver electrodes constituted the input of the transformer, the second pair — its output. Piezoelectric transformers have been already applied for the measurements of various properties of piezoelectrics, e.g. [11, 19, 20].

Analytical description of the physical processes (direct and converse piezoelectric effect, secondary effects, higher order effects) and their interactions in piezoelectric transformers is very difficult. Therefore equivalent circuits are applied to analyse transformer operation. However a large number of simplificating assumptions is necessary [12, 24].

We have used KLM equivalent circuit to obtain the following equations describing mechanical and electrical losses [24]:

$$\tan\delta_m = \frac{\phi^2 R_L(1-A_0)}{\pi Z_0 A_0}, \tag{2.1}$$

$$\tan\delta_e = (1-k_{31}^2)\frac{\phi^2 X_e(\tan\delta_m)^{-1} - \pi A_\infty Z_0}{\phi^2 X_e A_\infty(\tan\delta_m)^{-1}}, \tag{2.2}$$

$$\phi = \frac{\pi w d_{31}}{s_{11}^E}, \tag{2.3}$$

$$Z_0 = \pi w t \sqrt{\frac{\rho}{s_{11}^E}}\,, \tag{2.4}$$

$$X_e = \frac{1}{\omega C_0}\,, \tag{2.5}$$

$$C_0 = \frac{\pi a w \varepsilon_{33}^T}{t}\left(1 - k_{31}^2\right), \tag{2.6}$$

where $R_L$ — transformer load resistance, $A_0 = U_{\mathrm{OUT}}/U_{\mathrm{IN}}$ for $R_L \to 0$ (in this case $U_{\mathrm{OUT}} < U_{\mathrm{IN}}$), $A_\infty = U_{\mathrm{OUT}}/U_{\mathrm{IN}}$ for $R_L \to \infty$, $U_{\mathrm{IN}}$ — input voltage, $U_{\mathrm{OUT}}$ — output voltage, $k_{31}$ — electromechanical coupling coefficient, $w = (D_{\mathrm{EXT}} - D_{\mathrm{INT}})/2$, $a = (D_{\mathrm{EXT}} + D_{\mathrm{INT}})/4$, $D_{\mathrm{INT}}$ — internal diameter of the ceramic ring, $D_{\mathrm{EXT}}$ — external diameter of the ceramic ring, $t$ — thickness of the ceramic ring, $d_{31}$ — piezoelectric constant, $s_{11}^E$ — elastic compliance, $\rho$ — density, $\varepsilon_{33}^T$ — permittivity.

For the determination of loss it is not sufficient to measure only the voltage ratios for two limits of the loading of the piezoelectric transformer. In the high fields range the material constants of the piezoelectric ceramic change with the increase of the driving electric field [2, 27]. This is due to the domain structure of the ceramics [4, 6, 17, 33]. Very high electric fields and mechanical stresses can cause durable changes in the domain structure and ceramic parameters [10, 13]. In most cases the degradation of the polarization state occurs in high electric fields especially when the frequencies are near the resonance frequency of the piezoelectric element [23]. The changes of the resonance frequency of the piezoceramic element due to the changes of its material constants should be considered in the design of piezoelectric devices, e.g. piezoelectric motors [14].

## 3. Changes of the material coefficients of the piezoelectric ceramic due to the increase of the driving electric field

As we have mentioned in Sec. 2, the knowledge of the magnitude of ceramic material constants for the definite magnitude of the driving electric field is necessary to the calculations of losses using Eqs. (2.1) – (2.6). It is also necessary to the calculations of the magnitude of the mechanical signal (Sec. 4). In [26] the authors have published the following empirical formula describing the changes of the material coefficients of the piezoelectric ceramic as a function of the driving electric field:

$$\frac{\Delta x}{x_0} = \frac{x - x_0}{x_0} = \alpha E_{\mathrm{IN}}, \tag{3.1}$$

where $x = d_{31}$, $Y^E$, ..., $x_0$ — $x$ measured at the low field level, $\alpha$ — proportionality coefficient.

In Figs. 1 – 4 the results of the measurements of $\dfrac{\Delta\varepsilon_{33}^T}{(\varepsilon_{33}^T)_0}$, $\dfrac{\Delta s_{11}^E}{(s_{11}^E)_0}$, $\dfrac{\Delta k_{31}}{(k_{31})_0}$, $\dfrac{\Delta d_{31}}{(d_{31})_0}$ are presented for two kinds of ceramic used to make the piezoelectric ring transformers [24]: a — soft PZT-type ceramic, b — hard PZT-type ceramic. The continuous lines correspond to the formula (3.1). The experimentally obtained values of $\alpha$ for the material constants of the used ceramics are tabulated in Table 1. The values of $\alpha$ for the soft ceramic

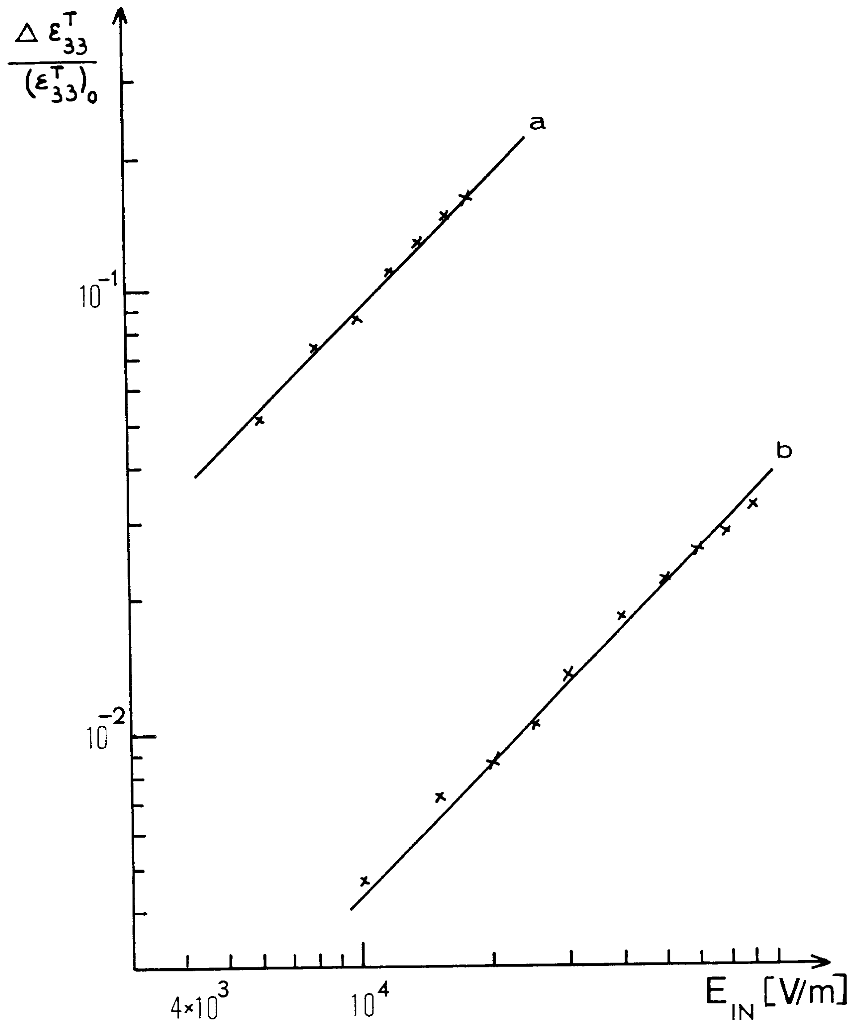


Fig. 1. Dependence of the changes of the permittivity on the input electric field, a — soft PZT-type ceramic, b — hard PZT-type ceramic, × — measured values, continuous line — calculated using (3.1).

**Table 1.** Values of $\alpha$ coefficient.

| Material constant | Soft PZT-type ceramic | Hard PZT-type ceramic |
|---|---|---|
| $d_{31}$ | $4 \cdot 10^{-5}$ | $1.9 \cdot 10^{-5}$ |
| $s_{11}^E$ | $9 \cdot 10^{-6}$ | $2.1 \cdot 10^{-6}$ |
| $k_{31}$ | $2.8 \cdot 10^{-5}$ | $1.6 \cdot 10^{-5}$ |
| $\varepsilon_{33}^T$ | $9 \cdot 10^{-6}$ | $4.3 \cdot 10^{-7}$ |

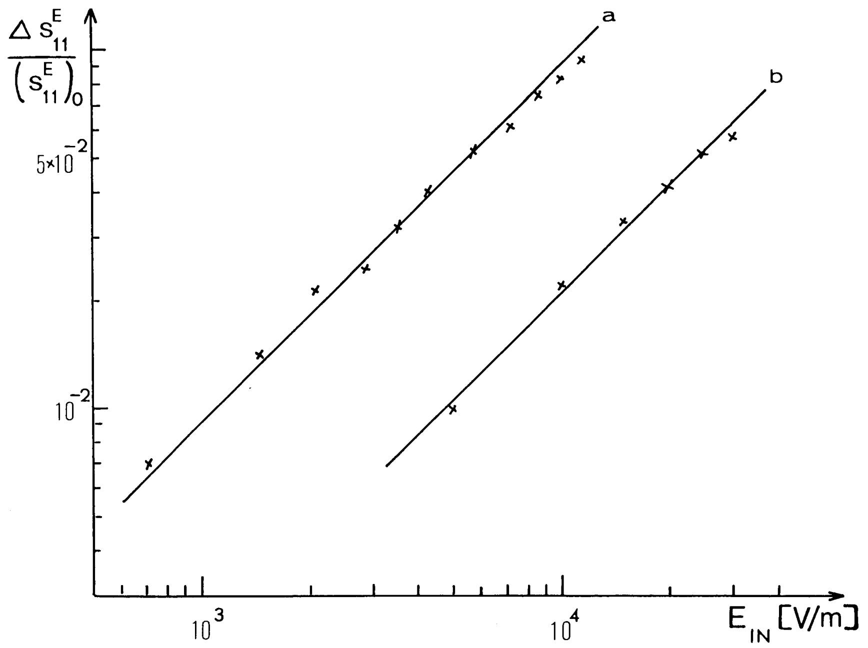


Fig. 2. Dependence of the changes of the elastic compliance on the input electric field, a — soft ceramic, b — hard ceramic, × — measured values, continuous line — calculated using (3.1).

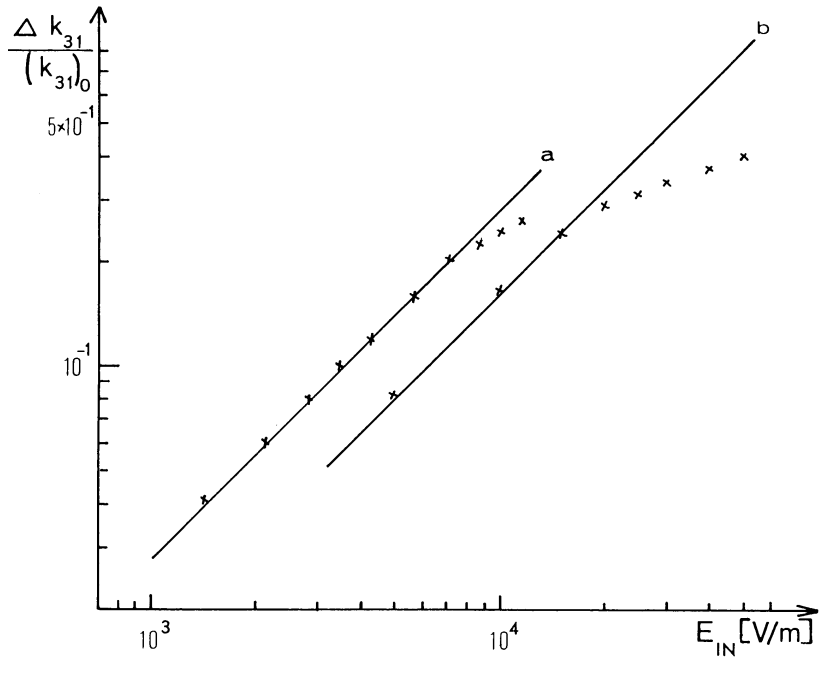


Fig. 3. Dependence of the changes of the electromechanical coupling coefficient on the input electric field, a — soft ceramic, b — hard ceramic, × — measured values, continuous line — calculated using (3.1).

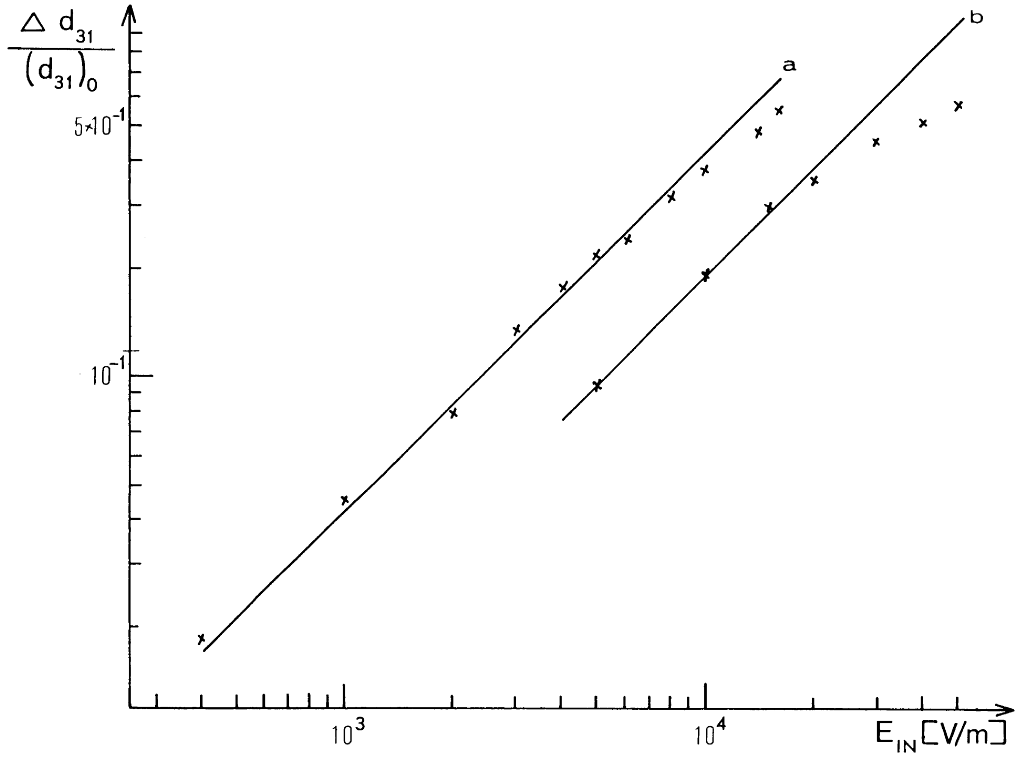


Fig. 4. Dependence of the changes of the piezoelectric constant on the input electric field, a — soft ceramic, b — hard ceramic, × — measured values, continuous line — calculated using (3.1).

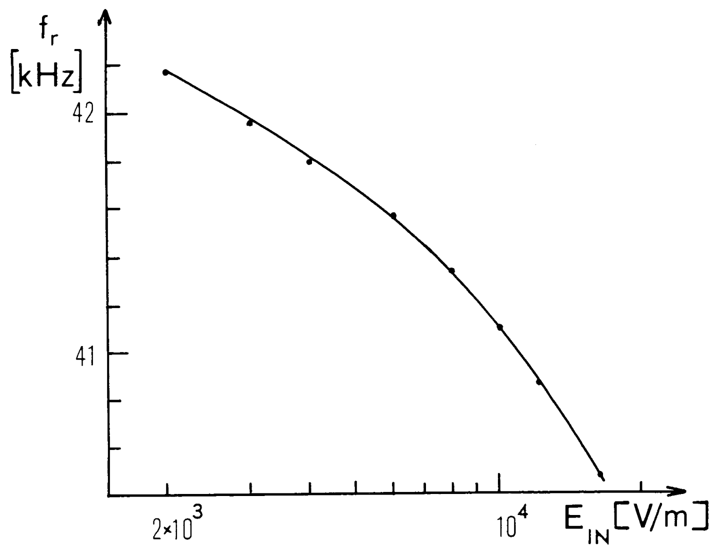


Fig. 5. Dependence of the resonance frequency on the input electric field for the ring made of the soft PZT-type ceramic.

are higher than for the hard one because the mobility of 90° domain walls is higher in the soft ceramic [33]. The manner of changes of the material constants and the range of electric fields are in accordance with earlier published results, e.g. [10, 17, 26]. For the electromechanical coupling coefficient $k_{31}$ (Fig. 3) and the piezoelectric constant $d_{31}$ (Fig. 4) one can see the distinct deflection of the measured values from the relation (3.1) in the range $E_{\mathrm{IN}} \geq 10^4$ V/m.

The changes of the material constants of the ceramic as a function of $E_{\mathrm{IN}}$ cause that the resonance frequency $f_r$ of the piezoelectric element changes also. Figure 5 presents an example of the dependence of $f_r$ on the magnitude of the driving electric field for a ring with full electrodes, the soft PZT-type ceramic.

## 4. Vibration velocity, strain and stress in a ring transformer

One can measure the displacement amplitude or vibration velocity of piezoelectric elements using a laser interferometer or a fibre optic vibrometer. In the case of a piezoceramic element the measurement circuit must have high sensitivity because ceramic surfaces have poor reflecting properties, especially for the ceramics with coarse grains and high porosity. The measurement circuit with very high sensitivity and very narrow light beam would be necessary for the measurement of the radial displacement of thin ceramic ring. Strains can be measured using a tensometer bridge. Unfortunately the ceramic driven by the high electric field warms up. This effect causes important measurements errors and impedes to apply tensometers.

One can calculate the strain amplitude $S_{1\ \max}$ applying the theory of ring vibrations [1, 18] and taking into the consideration the used configuration of electrodes [3]:

$$S_{1\ \max} = 1/2\, d_{31} E_{\mathrm{IN}} Q_m\,, \tag{4.1}$$

similarly for the amplitude of radial displacement $u_{\max}$:

$$u_{\max} = S_{1\ \max} a, \tag{4.2}$$

the amplitude of vibration velocity $v_{\max}$:

$$v_{\max} = \frac{1}{2} d_{31} E_{\mathrm{IN}} Q_m \frac{1}{\sqrt{\rho s_{11}^E}}\,. \tag{4.3}$$

the root-mean-square value of vibration velocity $v$:

$$v = \frac{1}{\sqrt{2}} v_{\max} = \sqrt{2}\,\pi f_r u_{\max} = \frac{1}{2\sqrt{2}} d_{31} E_{\mathrm{IN}} Q_m \frac{1}{\sqrt{\rho s_{11}^E}}\,, \tag{4.4}$$

and the amplitude of induced stress $T_{1\ \max}$:

$$T_{1\ \max} = \frac{S_{1\ \max}}{s_{11}^E} = \omega^2 a^2 \rho S_{1\ \max} = \sqrt{\frac{\rho}{s_{11}^E}}\, v_{\max} = \sqrt{\frac{2\rho}{s_{11}^E}}\, v = \frac{1}{2}\,\frac{d_{31}}{s_{11}^E} E_{\mathrm{IN}} Q_m\,. \tag{4.5}$$

In the calculations one should use the measured values of the ceramic material constants as a function of input electric field, presented in Sec. 3.

The quality factor measured using standard methods should be inserted as $Q_m$ into equations (4.1)–(4.5) when the ceramic is driven by low electric field and the electric losses can be neglected. In the range of high electric fields the electric losses cannot be neglected and one should insert into the above equations [25]:

$$Q_m = \frac{1 - k_{31}^2}{\tan\delta_m + k_{31}^2 \tan\delta_e} . \tag{4.6}$$

The magnitude of $Q_m$ $(E_{\mathrm{IN}})$ can be calculated using the results of the measurements of $\tan\delta_e(E_{\mathrm{IN}})$ and $\tan\delta_m(E_{\mathrm{IN}})$ obtained by means of the method described in Sec. 2 and the results of the measurements of $k_{31}$ $(E_{\mathrm{IN}})$ (Sec. 3).

Figures 6–8 present the strain $S_{1\,\max}$, the vibration velocity $v$ and the stress $T_{1\,\max}$ as a function of the input electric field for the ring piezoelectric transformers for a soft PZT-type piezoelectric ceramic with low quality factor and for a hard PZT-type piezoelectric ceramic with high quality factor. One can see that the vibration velocity, strain and stress do not increase proportionally to the increase of $E_{\mathrm{IN}}$, even in the range of relatively low electric fields. The dependence of the output voltage of the piezoelectric transformer on the magnitude of its input voltage is similar [24]. Similar results have been also obtained in [27]. The authors of that paper measured the vibration velocity of rectangular plates (L–E mode) made of various ceramics. They used an optical sensor. The curves $v$ $(E_{\mathrm{IN}})$

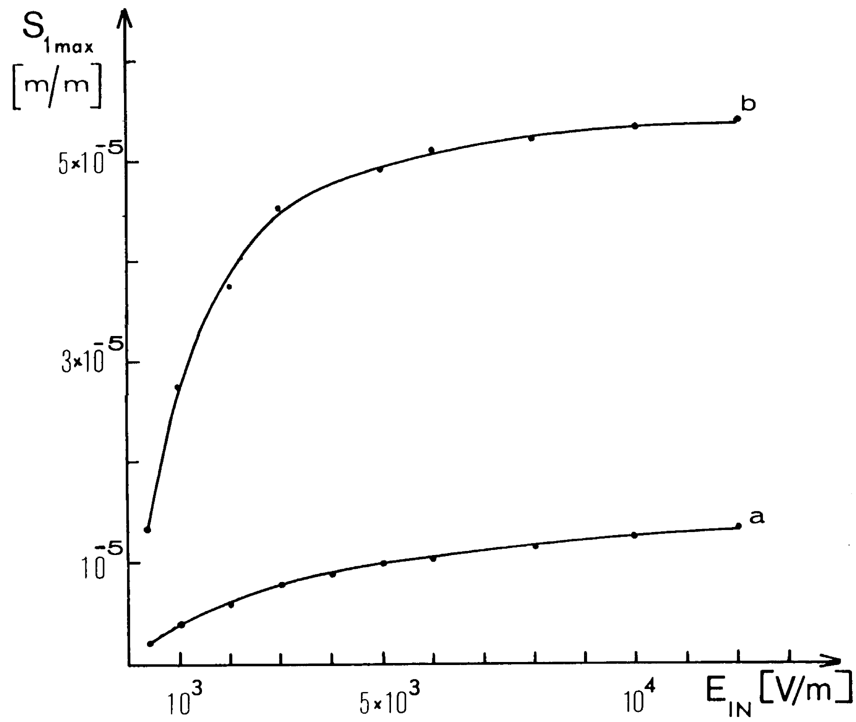


Fig. 6. Maximal strain as a function of the input electric field for the ring piezoelectric transformer, a) soft ceramic, $D_{\mathrm{EXT}} = 30\,\mathrm{mm}$, $D_{\mathrm{INT}} = 16\,\mathrm{mm}$, $t = 5\,\mathrm{mm}$; b) hard ceramic, $D_{\mathrm{EXT}} = 38\,\mathrm{mm}$, $D_{\mathrm{INT}} = 28\,\mathrm{mm}$, $t = 5\,\mathrm{mm}$.

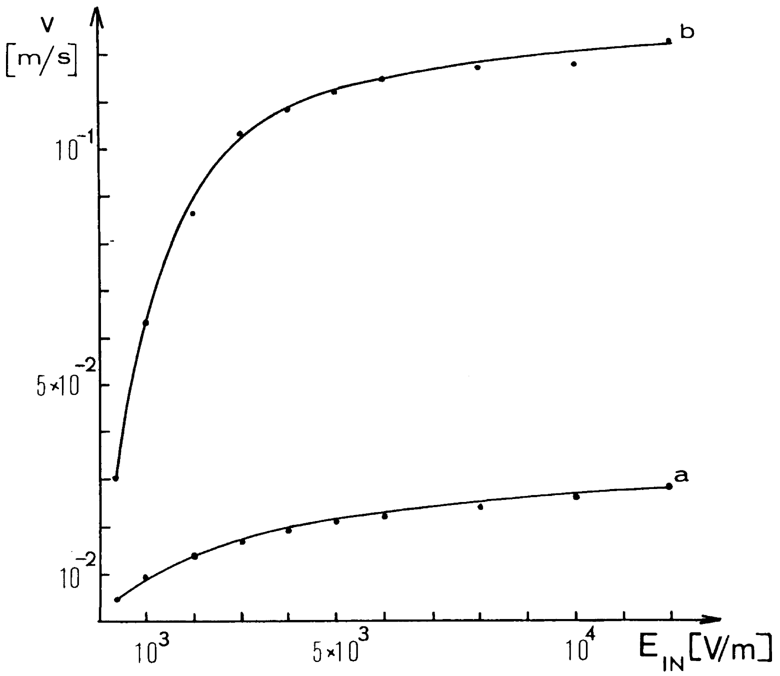


Fig. 7. Vibration velocity (rms) as a function of the input electric field. a, b — as in Fig. 6.

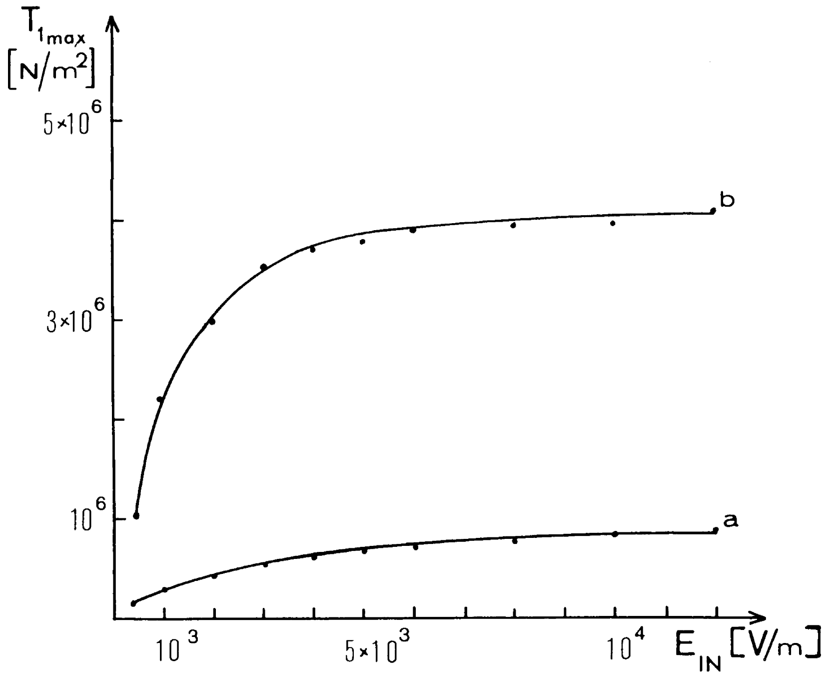


Fig. 8. Maximal stress as a function of the input electric field. a, b — as in Fig. 6.

obtained in this way tended to the saturation value for $E_{\mathrm{IN}} \geq 10^3$ V/m, similarly as in Fig. 7.

The authors of the theoretical analysis given in [15] have proved that the vibrational amplitude of a piezoelectric plate in the range of high fields is proportional to the cube root of the amplitude of the driving voltage. Therefore the vibrational amplitude (or vibrational velocity) has the tendency to saturate as the driving voltage increases. The authors of [15] confirmed this cubic relationship experimentally for plates of $LiNbO_3$ monocrystal ($Z$-cut, thickness-longitudinal vibration) using an interferometric heterodyne laser probe. Figure 9 presents the dependence $v$ ($E_{\mathrm{IN}}$) for a soft and for a hard PZT-type ceramic. The continuous line presents the relation $v = A\sqrt[3]{E_{\mathrm{IN}}}$ and $x$ denotes the values calculated using Eqs. (4.4) and (4.6). The proportionality coefficient for presented curves is equal: $A = 1.2 \cdot 10^{-3}$ for the soft ceramic and $A = 6.3 \cdot 10^{-3}$ for the hard ceramic. The proportionality coefficient depends on magnitudes of the second, third and fourth order elastic constants and the second and third order piezoelectric constants [15]. The obtained results indicate that the cubic relationship between the vibrational amplitude (velocity) and the driving voltage (electric field), foreseen by the theory given in [15], is also valid for polycrystalline piezoceramics.

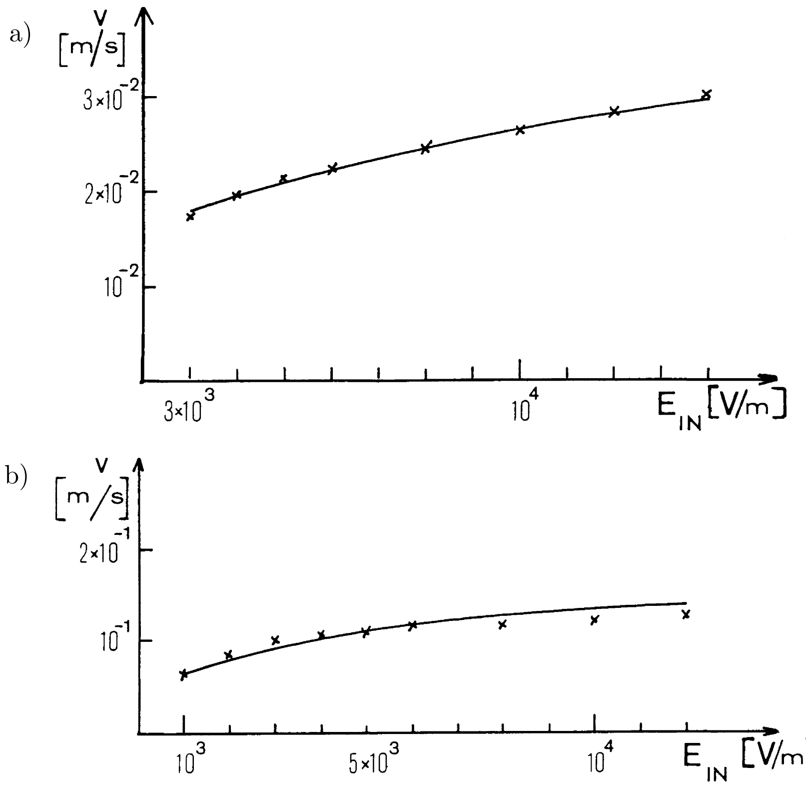


Fig. 9. Dependence of the vibration velocity on the input electric field, a) soft ceramic (as in Fig. 6a), b) hard ceramic (as in Fig. 6b). Continuous line — calculated according to the cubic relationship between the vibration velocity and the driving electric field, $\times$ — calculated using Eqs. (4.4) and (4.6).

## 5. Relations between losses in the piezoelectric ceramic and the magnitude of its vibration level

The dependence of the electrical and mechanical losses on the vibration velocity of the piezoelectric ceramic has been obtained using the formula given in Sec. 2,

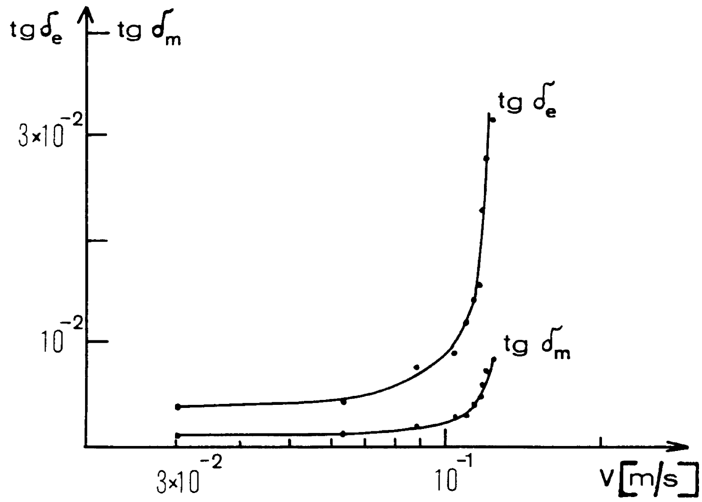


Fig. 10. Electrical and mechanical losses in the hard PZT-type ceramic as a function of the vibration velocity. Ring transformer with the dimensions as in Fig. 6b.

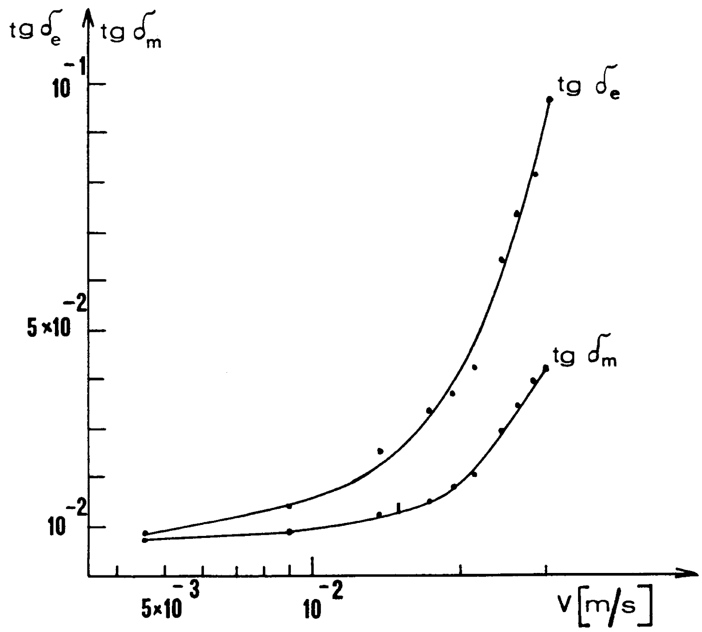


Fig. 11. Electrical and mechanical losses in the soft PZT-type ceramic as a function of the vibration velocity. Ring transformer with the dimensions as in Fig. 6a.

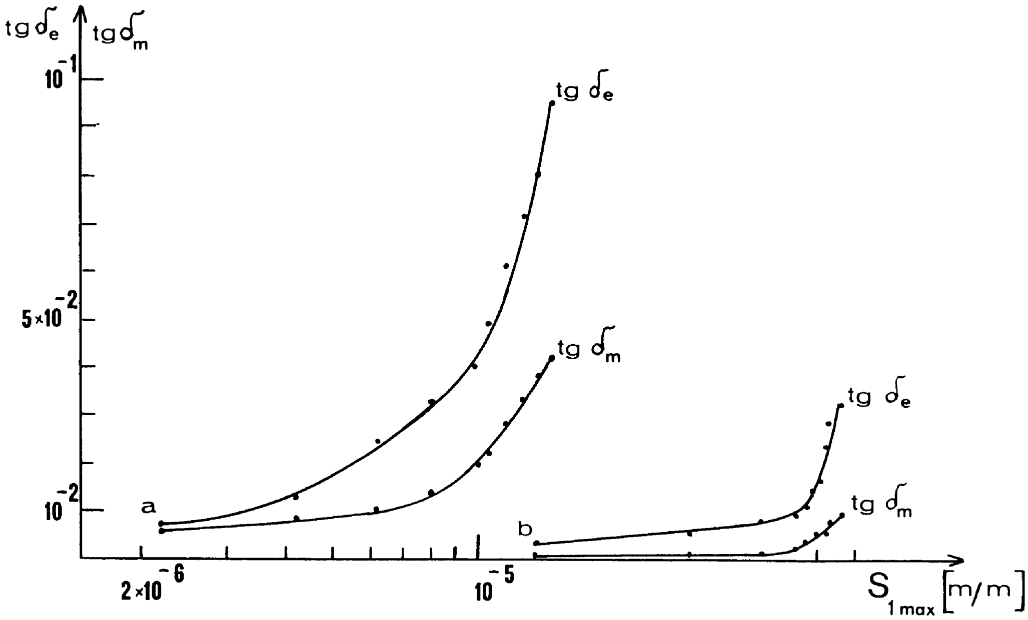


Fig. 12. Electrical and mechanical losses as a function of the maximal strain of the ring transformer, a — soft ceramic, b — hard ceramic. The dimensions of the transformers as in Fig. 6.

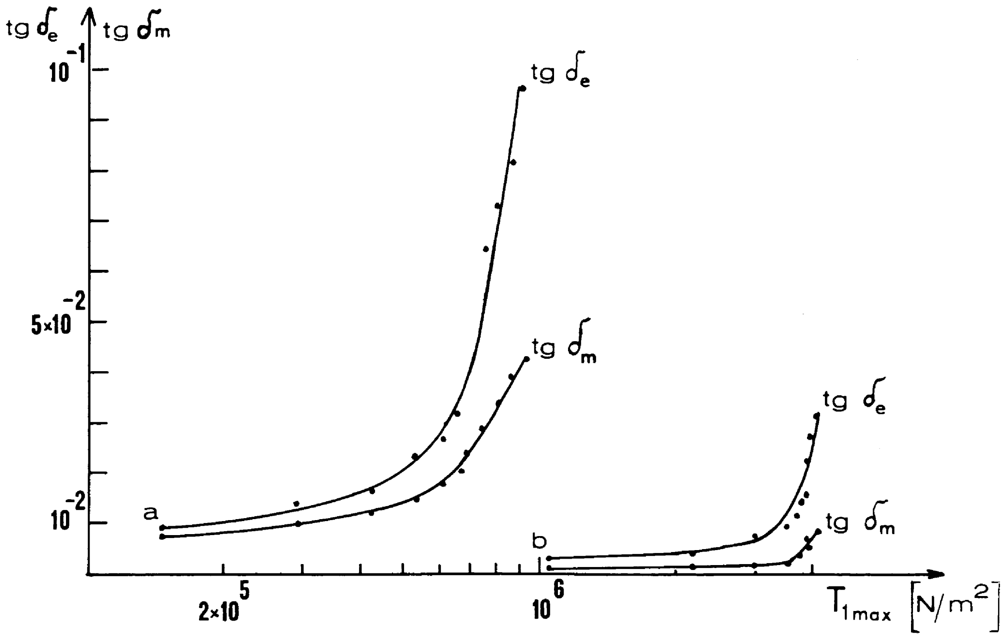


Fig. 13. Electrical and mechanical losses as a function of the maximal stress induced in the ring transformer, a — soft ceramic, b — hard ceramic. The dimensions of the transformers as in Fig. 6.

the measurements of $U_{\mathrm{OUT}}$ ($U_{\mathrm{IN}}$) for the piezoelectric transformers, the results of the measurements of the material constants presented in Sec. 3 and the calculation results given in Sec. 4. Figure 10 presents such a relationship for the transformer made of the hard ceramic, Fig. 11 — for the transformer made of the soft ceramic with higher losses. The dependences of the losses on $S_{1\,\mathrm{max}}$ (Fig. 12) and $T_{1\,\mathrm{max}}$ (Fig. 13) have been calculated in similar way.

In Figs. 10 and 11 one can see that the large increase of the mechanical as well as electrical losses occurs for the vibration velocity $v > 10^{-1}$ m/s for the hard ceramic and $v > 10^{-2}$ m/s for the soft one. This is in accordance with the results obtained by the other authors applying different methods of loss measurements, e.g. [22, 25, 30, 31].

## 6. Conclusion

The realized measurements and calculations prove that the proposed earlier [24] method of the loss measurements can be also applied to determine the relations between the vibration velocity, stress, strain and the electrical and mechanical losses in the piezoelectric ceramic. The obtained results are in accordance with the results obtained by the other authors applying different measurement methods.

The analysis of the generation of harmonics of an output voltage will be necessary to apply the presented method in the range of still higher electric fields. The occurence of the second and third harmonics causes the distortion of the output voltage [8]. Output voltages of the transformers made of the ceramic with low quality factor were not distorted in the whole range of input voltages applied in the measurements described in the paper. Output voltages of the transformers made of the ceramic with high quality factor were distorted in the upper range of applied input voltages but only at the frequencies of the jump phenomenon [24] and only for $R_L \to \infty$. Similar effect has been observed in piezoceramic resonators (length extensional vibration mode) [28].

## References

[1] D.A. Berlincourt, D.R. Curran and H. Jaffe, *Piezoelectric and piezomagnetic materials*, Physical Acoustics, Vol. IA, W.P. Mason [Ed.], Academic Press, New York 1964, Ch. 3.

[2] C.W. Bert and V. Birman, *Effects of stress and electric field on the coefficients of piezoelectric materials: one-dimensional formulation*, Mechanics Res. Commun., **25**, 2, 165–169 (1998).

[3] W.G. Cady, *Piezoelectricity*, Mc Graw Hill, New York 1946, Ch. V, XIII and XV.

[4] D. Damjanovic and D.V. Taylor, *Contributions to the nonlinear dielectric and piezoelectric response of ferroelectric thin films and ceramics*, Ferroelectrics, **221**, 137–146 (1999).

[5] G.H. Haertling, *Ferroelectric ceramics*, J. Am. Ceram. Soc., **82**, 4, 797–818 (1999).

[6] D.A. Hall, *Rayleigh behaviour and the threshold field in ferroelectric ceramics*, Ferroelectrics, **223**, 319-328 (1999).

[7] *IRE Standards on piezoelectric crystals: Measurement of piezoelectric ceramics*, Proc. IRE, **49**, 7, 1161–1169 (1961).

[8] K. Ishii, N. Akimoto, S. Tashiro and H. Igarashi, *Analysis of nonlinear phenomena in piezoelectric ceramics under high-power vibration*, J. Ceram. Soc. Jpn., **106**, 6, 555–558 (1998).

[9] M. Kamlah and C. Tsakmakis, *Phenomenological modeling of the non-linear electromechanical coupling in ferroelectrics*, Int. J. Solids Struct., **36**, 669–695 (1999).

[10] W.Ł. Karłasz, *Influence of an electric driving field on energy dissipation in piezoceramic resonators* [in Russian], Rassiejanie energii pri kolebaniach mechaniczeskich sistem, G.S. Pisarenko [Ed.], Naukova Dumka, Kiev 1980, 344–348.

[11] W.Ł. Karłasz, *Determination of piezoceramic parameters using piezotransformer sensor* [in Russian], Tiepłowyje napria§enia w elementach konstrukcij, **20**, Naukova Dumka, Kiev 1980, 110–112.

[12] B.A. Kudriawcew, W.Z. Parton and N.A. Senik, *Mechanical models of piezoelectrics* [in Russian], Itogi Nauki i Techniki, Ser.: Mechanika deformirujemogo tieła, **17**, WINITI, Moskwa 1984, 3–63.

[13] V.D. Kugel and L.E. Cross, *Behavior of soft piezoelectric ceramics under high sinusoidal electric fields*, J. Appl. Phys., **84**, 5, 2815–2830 (1998).

[14] M. Kummel, S. Goldschmidt and J. Wallaschek, *Theoretical and experimental studies of a piezoelectric ultrasonic linear motor with respect to damping and nonlinear material behaviour*, Ultrasonics, **36**, 1-5, 103–109 (1998).

[15] X. Li, W. Jiang and Y. Shui, *Coupled mode theory for nonlinear piezoelectric plate vibrations*, IEEE Trans. Ultrason. Ferroel. Freq. Contr., **45**, 3, 800–805 (1998).

[16] T. Michelitsch and W.S. Kreher, *A simple model for the nonlinear material behavior of ferroelectrics*, Acta Mater., **46**, 14, 5085–5094 (1998).

[17] V. Mueller and Q.M. Zhang, *Threshold of irreversible domain wall motion in soft PZT̄piezoceramic*, Ferroelectrics, **206-207**, 113–122 (1998).

[18] G.G. Pisarenko, *Strength of piezoceramic* [in Russian], Naukova Dumka, Kiev 1987, Ch. III.2.

[19] D.L. Rastorguyev and N.N. Andreyev, *Piezoelectric transformer technique for testing of flexible piezoelectric materials*, Acustica, **82**, suppl. 1, 179 (1996).

[20] Ł.G. Rozin, S.O. Kramarow and W.P. Sawin, *On the destruction of piezoceramic under high frequency loading* [in Russian], Procznost materiałow i elementow konstrukcij pri zwukowych i ultrazwukowych czastotach nagruženia, Naukova Dumka, Kiev 1986, 180–184.

[21] K. Sakurai, T. Nakazawa, S. Shindou, K. Ohnishi and Y. Tomikawa, *Experimental investigation of a piezoelectric ceramic transformer using radial vibration of disks combined with a coupling element*, Jpn. J. Appl. Phys., Part 1, **37**, 5B, 2896–2900 (1998).

[22] Y. Sasaki, S. Takahashi and S. Hirose, *Relationship between mechanical loss and phases of physical constants in lead-zirconate-titanate ceramics*, Jpn. J. Appl. Phys., Part 1, **36**, 9B, 6058–6061 (1997).

[23] Z. Surowiak, *Physical foundations of the poling process of electroacoustic piezoceramic transducers* [in Polish], Akustyka, Akustooptyka, Optoelektronika, Politechnika Śląska, Gliwice 1998, 75–101.

[24] M. Szalewski, *Losses in a piezoelectric ceramic in high fields*, Archives of Acoustics, **24**, 1, 57–74 (1999).

[25] S. Takahashi, S. Hirose, K. Uchino and K.Y. Oh, *Electromechanical characteristics of lead-zirconate-titanate ceramics under vibration level change*, Proc. 9th IEEE Int. Symp. Appl. Ferroelectrics, 377–382 (1994).

[26] S. Takahashi, M. Yamamoto and Y. Sasaki, *Nonlinear piezoelectric effect in ferroelectric ceramics*, Jpn. J. Appl. Phys., Part 1, **37**, 9B, 5292–5296 (1998).

[27] S. Takahashi, Y. Sasaki and S. Hirose, *Driving electric field effects on piezoelectric transducers*, Jpn. J. Appl. Phys., Part 1, **36**, 5B, 3010–3015 (1997).

[28] S. Tashiro, M. Ikehiro and H. Igarashi, *Influence of temperature rise and vibration level on the electromechanical properties of high-power piezoelectric ceramics*, Jpn. J. Appl. Phys., Part 1, **36**, 5B, 3004–3009 (1997).

[29] D.V. Taylor and D. Damjanovic, *Domain wall pinning contribution to the nonlinear dielectric permittivity in* Pb(Zr,Ti)$O_3$ *thin films*, Appl. Phys. Lett., **73**, 14, 2045–2047 (1998).

[30] K. Uchino, *Material issues in design and performance of piezoelectric actuators: an overview*, Acta Mater., **41**, 11, 3745–3753 (1998).

[31] M. Umeda, K. Nakamura and S. Ueha, *The measurements of high-power characteristics for a piezoelectric transducer based on the electrical transient response*, Jpn. J. Appl. Phys., Part 1, **37**, 9B, 5322–5325 (1998).

[32] J.S. Yang and W. Zhang, *A thickness shear high voltage piezoelectric transformer*, Int. J. Appl. Electromagn. Mech., **10**, 2, 105–121 (1999).

[33] Q.M. Zhang, W.Y. Pan, S.J. Jang and L.E. Cross, *Domain wall excitations and their contributions to the weak-signal response of doped lead zirconate titanate ceramics*, J. Appl. Phys., **64**, 11, 6445–6451 (1988).

ARCHIVES OF ACOUSTICS
**25**, 2, 251–269 (2000)

# THE INFLUENCE OF PB VACANCIES ON THE PROPERTIES OF PZT-TYPE CERAMIC TRANSDUCERS

Z. SUROWIAK, L. KOZIELSKI, B. WODECKA-DUŚ

Silesian University,
Department of Materials Sciences
(41–200 Sosnowiec, 2 Śnieżna St., Poland)
e-mail:surowiak@us.edu.pl

E.G. FESENKO, O.N. RAZUMOVSKAYA, L.A. REZNICHENKO,
I.N. ZAKHARCHENKO

Rostov State University,
Faculty of Physics
(344-104 Rostov-on-Don, 5 Zorge Str., Russia)

*This article is dedicated to prof. J. Ranachowski*

The result of investigations of the influence of lead vacancies on the crystalline structure of PZT-type ceramic piezoelectric materials is presented. The solid solution of $PbTiO_3$ – $PbZrO_3 - \sum\limits_{n=1}^{3} Pb(B'_{1-\alpha}B''_{\alpha})O_3$, characterized by the perovskite-type structure ($ABO_3$), is the basis of those materials. The lead vacancies ($V^{\mathrm{Pb}}$) was originated by a thermal treatment. Investigations of the influence of the lead deficiency on the crystalline structure of PZT-type ceramics have been performed for solid solutions characterized by compositions corresponding to the tetragonal or rhombohedral boundary of the morphotropic region (PCR-1, PCR-8: *Piezoelectric Ceramics of Rostov*) and to tetragonal phase region compositions (ceramics of $Pb_{1-x}$ $(Zr_{0.39}Ti_{0.59}W_{0.01}Cd_{0.01})O_3$). It has been found that the deficiency in lead causes a reconstruction of the perovskite phase crystalline structure or a change of the elementary cell parameters of that phase. The solid solutions on the basis of $Pb(Zr,Ti)O_3$ resolve themselves into $PbTiO_3$, $ZrO_2$ and PbO when the lead deficiency caused by thermal treatment increases.

**Keywords:** piezoelectrics ceramic, PZT-type solid solution, lead vacancies, structure, electroācoustic properties, transducers.

## 1. Introduction

The PZT-type ceramic material is a solid solution of $PbTiO_3$ and $PbZrO_3$, the general molecular formula of which is $Pb(Zr_{1-x}Ti_x)O_3$. The phase diagram of the non-modified

PZT ceramic material (Fig. 1) indicates that when $Ti^{4+}$ ions are substituted by the $Zr^{4+}$ ions the tetragonal deformation of $PbTiO_3$ decreases. Next (for Zr : Ti = 55 : 45), the so-called morphotropic boundary (MB) appears at room temperature. A further increase in the $Zr^{4+}$ concentration involves the creation of a new rhombohedral ferroelectric phase (R3m). The boundary between the tetragonal and rhombohedral phase (morphotropic boundary) depends on the temperature. If the concentration of $Zr^{4+}$ is greater than 95 mol.%, there is an antiferroelectric orthorhombic phase (typical for $PbZrO_3$) in the PZT solid solution. A narrow region of the stable antiferroelectric tetragonal phase occurs close to the Curie point in this case.

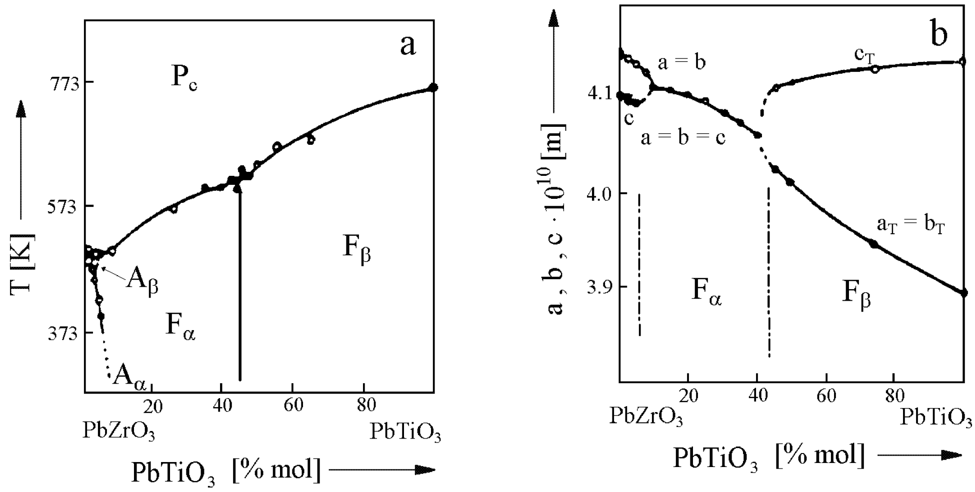


Fig. 1. The phase diagram of the $Pb(Zr_{1-x}Ti_x)O_3$ solid solution [1–2]. $F_\beta$ — ferroelectric tetragonal phase; $F_\alpha$ — ferroelectric rhombohedral phase; $A_\alpha$, $A_\beta$ — antiferroelectric phases; $P_c$ — cubic phase; $F_\alpha/F_\beta$ — morphotropic boundary.

PZT materials characterized by constitutions, which are close to the morphotropic phase boundary show distinct piezoelectric properties. One can optimize these properties according to the requirements of the applications by modifying the basic constitution or by doping, e.g. in accordance to the following molecular formula:

$$PbTiO_3 - PbZrO_3 - \sum_{n} Pb(B'_{1-\alpha}B''_{\alpha})O_3\,, \tag{1}$$

where $\alpha = 1/2$; 1/3; 1/4 (depending on valence number of the B′ and B″ cations); $B' = Nb^{5+}$, $Sb^{5+}$, $Ta^{5+}$, $W^{6+}$; $B'' = Li^{1+}$, $Mg^{2+}$, $Ni^{2+}$, $Zn^{2+}$, $Co^{2+}$, $Mn^{2+}$, $Cd^{2+}$, $Fe^{2+}$, $Bi^{3+}$, $Sb^{3+}$.

The addition of some modifiers amounting to (1 − 3) mol.%, causes, among other things, a broadening of the range of coexistence of the rhombohedral and tetragonal phases. In this case, the morphotropic region (MR) appears in the phase diagram in the range of (40 − 43.5) mol.% of $Ti^{4+}$ (Fig. 2) instead of the morphotropic boundary MB (line). Materials prepared on the basis of the $Pb(Zr,Ti)O_3$ solid solution are called PZT-type materials for short. Depending on the chemical constitution, different patent symbols have been given to them (e.g. Polish: PP-4, PP6-CM, PP-N; Russian: CTS-836, PCR-1, PCR-8; Brush-Clevite firm: PZT-4; Mullard firm: PXE5).

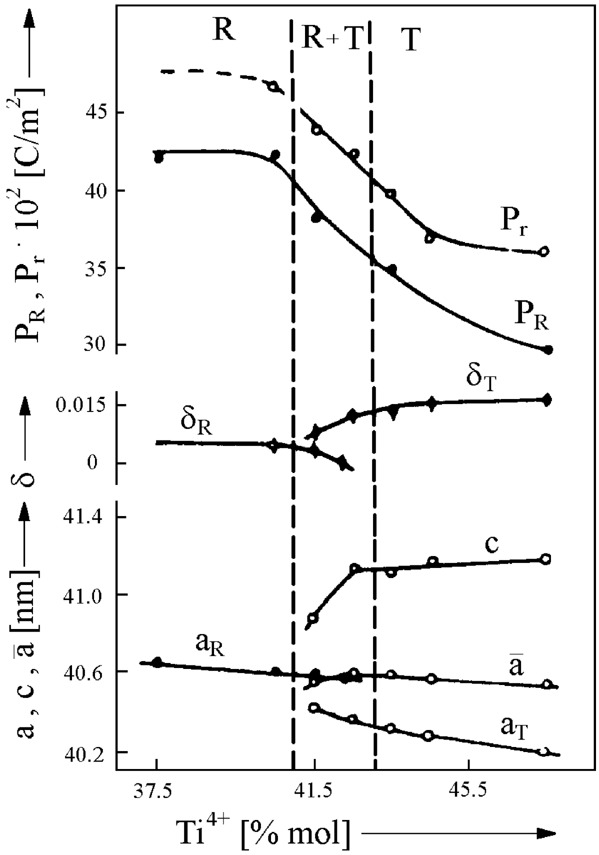


Fig. 2. Changes of the parameters ($a_R$, $a_T$, $c_T$, $\bar{a}$), the spontaneous deformation ($\delta_R$, $\delta_T$) of the elementary cell, orientational polarization ($P_r$) and residual polarization ($P_R$) during the transition from the rhombohedral (R) phase through the morphotropic region (R+T) to the tetragonal (T) phase for PZT-type ceramics at 293 K.

PZT-type materials are commonly used in engineering (among other things as electromechanical transducers). The increasing application possibilities of these materials are connected with both the selection of the chemical constitution and the improvement of the structure and microstructure (decreasing porosity, increasing density, decreasing grain dimensions) by means of a choice of suitable technological conditions. The PZT-type ceramic materials are obtained by both the classical method, which is worldwide used on an industrial scale [3, 4], and the sintering under pressure one (so-called hot-pressing method) (e.g. [5]). So far, the latter becomes more widespread in the technology of special purpose ceramics, however only in a laboratory or semiindustrial scale. By means of sintering under pressure as well as the fine-grained ((1 − 4) μm in diameter), the medium sized ((5 − 9) μm in diameter) and coarse-grained ((9 − 12) μm in diameter) ceramic materials are obtained. After a mechanical treatment (cutting, grinding, polishing) one can obtain thin ceramic plates of $d_f > 8\,\mu\mathrm{m}$ thickness and a perfectly smooth surface ($\nabla 14$). This is impossible in the case of the same PZT materials obtained by the classical method (small density, large porosity and small mechanical strength).

A very important question in the technology of ceramic ferroelectric materials is to provide consistence in the stoichiometry between the product obtained and the chemical constitution described by a molecular formula of the compound or the solid solution. It is of great importance in the case of ceramic ferroelectrics containing lead. The temperature of sintering (synthesis) of those compounds is higher than the lead sublimation temperature. This is why the real ceramic ferroelectrics of that type are characterized by a disturbance in the stoichiometry. This disturbance is connected with the creation of lead vacancies ($V^{\mathrm{Pb}}$) in the PZT crystalline structure. It influences strongly the electrical properties (first of all the electrical transport phenomena) and the structure parameters of those materials in the ferroelectric state.

Three methods of controlled creation of lead vacancies in the PZT-type solid solutions are generally applied, namely:

1) the roasting at $T_s = (1073 - 1323)\,\mathrm{K}$ within $t_s = (1 - 3)$ hours under oxygen [1];

2) the obtaining of the PZT-type solid solution from a mixture of suitable powdered oxides deficient in PbO [6];

3) modification of the PZT-type ceramics by soft doping [7].

One can sometimes use a combination of those three methods to form lead vacancies $V^{\mathrm{Pb}}$ [8].

There are few published works on the influence of the vacancies on the crystalline structure of the solid solutions of the PZT basis. However, there are experimental data about the influence of $V^{\mathrm{Pb}}$ on the physical properties (mechanical, dielectric, semiconductive, piezoelectric) of such solid solutions [7, 8]. It is relevant to PZT modified by soft admixtures [9].

In the present paper, the results of investigations on the influence of lead vacancies ($V^{\mathrm{Pb}}$) on the crystalline structure of the PZT-type piezoceramics are described.

## 2. Results and discussion

### *2.1. Basic dielectric, piezoelectric and mechanical properties of the electro-acoustic transducers obtained*

On the phase diagram of every of the PZT-type solid solutions, there are some regions of the chemical constitutions which provide an optimal set of values of the electromechanical parameters of the materials obtained on the basis of these solutions. This is shown in Fig. 3 and Table 1. High effective piezoceramic materials have been obtained by choosing a proper chemical constitution and technological conditions. The materials are characterized by parameters, which are optimal for the application, e.g. in acousto-electronics. All the new piezoelectric materials obtained can be divided into the seven following groups:

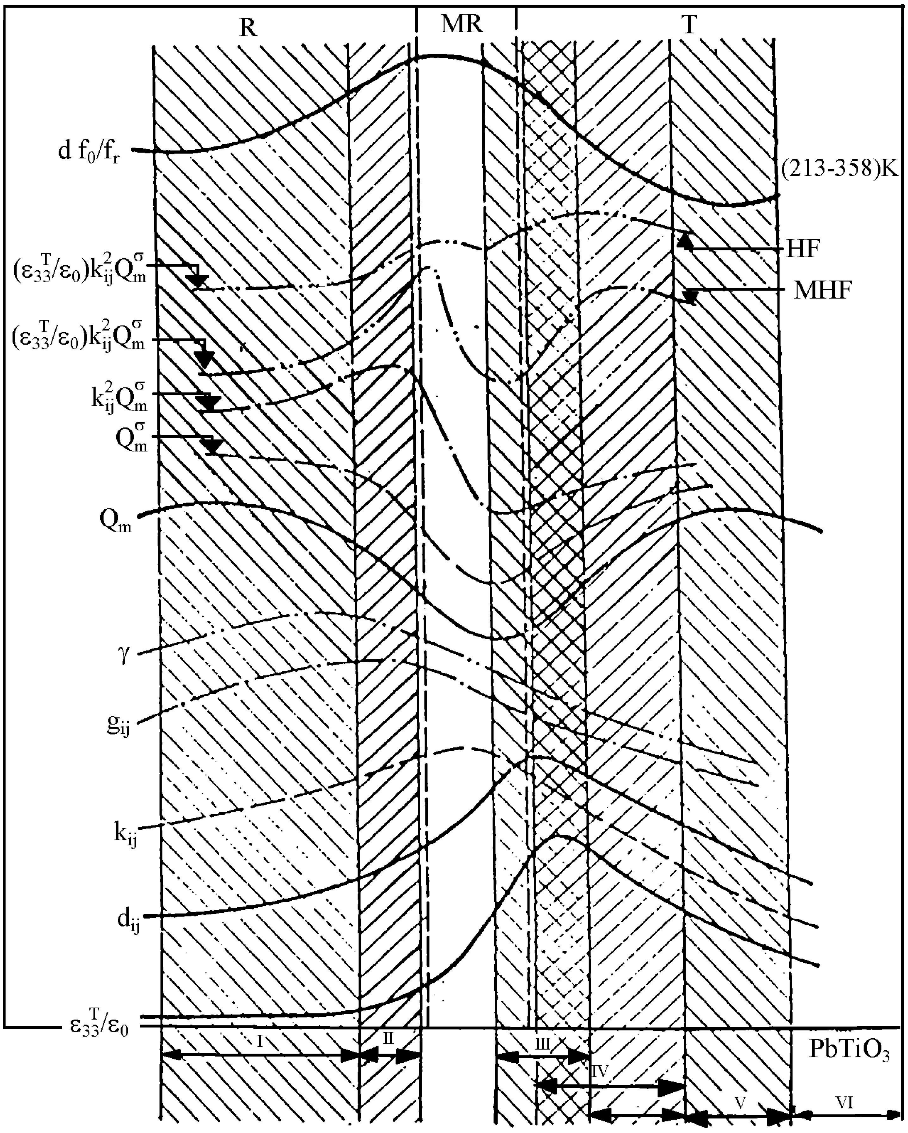


Fig. 3. Influence of the concentration of $PbTiO_3$ on the values of the electrophysical parameters of the multicomponent solid solutions on the basis of PZT in the vicinity of the morphotropic region.

**Group I:** piezoceramics characterized by small values of the permittivity ($\varepsilon_{33}^{\sigma}/\varepsilon_0$).

Possible applications:

1. High frequency electroacoustic transducers:

a) volume waves: — large $k_{15} = 0.75$,

— small $\varepsilon_{33}^{\sigma}/\varepsilon_0 < 500$,

— not required large $Q_m = 200 - 1000$;

**Table 1.** Chemical constitution-structure-physical properties-application of the multicomponent solid solutions: $PbTiO_3 - PbZrO_3 - \sum_n Pb(B'_{1-\alpha}B''_{\alpha})O_3$.

| Region, phase | Ferroelectric (HF, MHF, SF) | M [mol% $PbTiO_3$] | External parameters-large | External parameters-small | Application (examples) |
|---|---|---|---|---|---|
| I(R) | MHF, SF | $-(3-25)$ | $\gamma$ | $\varepsilon_{33}^T/\varepsilon_0$<br>$Q_m, k_{ij}$ | High frequency piezoelectric transducers. Pyroelectric detectors. |
| II(R) | HF, MHF | $-(1-3)$ | $g_{ij}$,<br>$k_{ij}^2 \cdot Q_m^\sigma$ | $Q_m$ | Defectoscopes, accelerometers, high voltage piezoelectric transformers. |
| III (MR, T) | SF | $+(0.5-2)$ | $k_{ij}$, $d_{ij}$<br>$\varepsilon_{33}^\sigma/\varepsilon_0$,<br>$d_{ij}/(\varepsilon_{33}^\sigma/\varepsilon_0)$ | $Q_m$ | Low frequency transducers, microphones, hydrophones. |
| IV (T) | HF<br>MHF, SF | $+(1-4)$<br>$+(2-4)$ | $k_{ij}^2 \cdot Q_m^\sigma \cdot (\varepsilon_{33}^T/\varepsilon_0)$<br>$(d_{ij}Y_{ij}^E)^2$<br>$k_{ij}^2/\tan\delta$ | $\tan\delta$ | Low voltage piezoelectric transformers; piezoelectric engines. Ultrasonic piezoelectric transducers. |
| V (T) | HF, MHF | $+(4-10)$ | $Q_m$ | $\delta f_\Theta/f_r$ | Filters. |
| VI (T) | HF, MHF, SF | $+(5-25)$ | $T_c$ | – | High temperature transducers. |

b) surface waves: — very small $\varepsilon_{33}^\sigma/\varepsilon_0 < 290$,
— large $Q_m = 4000$,
— large $k_p > 0.50$;

2. High stability ultrasonic delay lines:
— very small $\varepsilon_{33}^\sigma/\varepsilon_0 < 290$,
— large $k_p > 0.50$,
— large $Q_m = 2000 - 4000$;

3. Pyroelectric sensors:
— large $\gamma > 5 \times 10^{-4}\,\mathrm{C \cdot m^{-2} \cdot K^{-1}}$,
— small $\varepsilon_{33}^\sigma/\varepsilon_0 < 500$.

**Group II:** piezosensitive ceramics characterized by large $g_{ij}$, $k_p$, $k_t$, $k_{15}$, $k_{ij}^2 Q_m^\sigma$ and small $Q_m$ (high piezoelectric sensitivity to mechanical influences).

Possible applications:
1) accelerometers,
2) defectoscopes,
3) devices for medical diagnostic,
4) ferroelectric memory elements,
5) high voltage step-up piezoelectric transformers.

**Group III:** piezoceramics characterized by large $k_{ij}$, $d_{ij}$, $\varepsilon_{33}^{\sigma}/\varepsilon_0$ and small $Q_m$ (low frequency transducers).

Possible applications:
1. Direct piezoelectric effect: microphones, hydrophones, sound reproducers.
2. Converse piezoelectric effect: devices for robotics, deflectors in optical system.

**Group IV (a):** ferroelectrically hard (HF) piezoceramics characterized by large values of $k_{ij}^2 \cdot Q_m^{\sigma} \cdot \varepsilon_{33}^{\sigma}/\varepsilon_0$, $(d_{ij}Y_{ij})^2$, $k_{ij}^2/\tan\delta$ and a small $\tan\delta$ (piezoelectric materials which are slightly tractable to external influences).

Possible applications:
1. Piezoelectric step-down transformers (large $k_{ij}^2 \cdot Q_m^{\sigma} \cdot \varepsilon_{33}^{\sigma}/\varepsilon_0$).
2. Piezoelectric servo-motors (large $d_{31}^2 \cdot Q_m \cdot Y_{11}^E$).

**Group IV (b):** ferroelectrically soft (SF) piezoceramics highly tractable to external influence.

Possible applications:
1. High power ultrasonic generators (large $k_{33}^2/\tan\delta$ and $(d_{31}Y_{11}^E)^2$).

**Group V:** piezoceramics with high temperature and time stability of the resonance frequency (small $\Delta f_r/f_r$; large $k_p$ provides a wide pass band of the filters; sharpness of the amplitude-frequency characteristics within the pass band of the filters depend on $Q_m$).

Possible applications:
1. Filters with high temperature and time stability.

**Group VI:** high temperature piezoelectric ceramics (materials with large $T_c > 700\,\mathrm{K}$, small $\varepsilon_{33}^{\sigma}/\varepsilon_0$ and relatively good piezoelectric parameters).

Possible application:
1. Electroacoustic devices operating at high temperatures and high frequencies (nuclear engineering, space technology, metallurgy).

In this work the following piezoceramic materials were investigated: PCR-1 (Group II), PCR-8 (Group IV) and $Pb_{1-x}(Zr_{0.39}Ti_{0.59}W_{0.01}Cd_{0.01})O_3$ (Group V).

The basic physical parameters of this piezoceramics are shown in Table 2, where:

| | |
|---|---|
| $\varepsilon_{33}^{\sigma}/\varepsilon_0$ | free dielectric constant ($\sigma = 0$ or $\sigma = \text{const.}$); |
| $\varepsilon_{33}^{\sigma}$ | permittivity ($\sigma = 0$ or $\sigma = \text{const.}$); |
| $\varepsilon_0$ | permittivity of free space ($\varepsilon_0 = 8.85 \cdot 10^{-12}\,\mathrm{F/m}$); |
| $k_p, k_{31}, k_{33}$ | electromechanical coupling factors; |
| $d_{31}, g_{33}$ | piezoelectric constants ($g_{nj} = \sum\limits_{-1} \beta_{nm}^{\sigma} d_{mj}$, $g_{nj} = \sum \dfrac{d_{nj}}{\varepsilon_{nm}^{\sigma}}$); |
| $\beta_{nm}^{\sigma}$ | dielectric impermeabilities ($\varepsilon_{nm}^{-1}$); |

**Table 2.** Basic physical parameters of the piezoceramics obtained.

| Materials / Parameters | | PCR-1 | PCR-8 | $Pb(Zr_{0.39}Ti_{0.59}W_{0.01}Cd_{0.01})O_3$ |
|---|---|---|---|---|
| Phase | | rhombohedral (near the MR) | tetragonal (near the MR) | tetragonal (far the MR) |
| $\varepsilon_{33}^{\sigma}/\varepsilon_0$ | | 650 | 1400 | 1300 |
| $k_p$ | | 0.62 | 0.58 | 0.47 |
| $k_{31}$ | | 0.70 | 0.34 | 0.32 |
| $k_{33}$ | | 0.73 | 0.66 | 0.42 |
| $d_{31} \cdot 10^{12}$ [C/N] | | 95 | 130 | 105 |
| $g_{33} \cdot 10^3$ [V·m/N] | | 38 | 23.5 | 16 |
| $\tan\delta \cdot 10^2$ | $E_{\sim}^0 = 5\,\text{kV/m}$ | 2 | 0.35 | 0.35 |
| | $E_{\sim}^0 = 100\,\text{kV/m}$ | 3.5 | 0.70 | 0.90 |
| $Q_m$ | | 90 | 2000 | 1750 |
| $Q_m^{\sigma}$ ($\sigma = 12\,\text{MPa}$) | | 70 | 700 | 750 |
| $k_{31}^2 \cdot Q_m^{\sigma}$ | | 34 | 81 | 74.5 |
| $\dfrac{\varepsilon_{33}^{\sigma}}{\varepsilon_0} k_{31}^2 Q_m^{\sigma} \cdot 10^{-3}$ | | 22 | 114 | 96 |
| $k_{33}^2/\tan\delta$; ($E_{\sim}^0 = 100\,\text{kV/m}$) | | 26.65 | 62 | 19.6 |
| $\sigma_{\text{dyn}}$ [MPa] | | 90 | 40 | 70 |
| $T_c$ [K] | | 628 | 598 | 513 |
| $Y_{11}^E \cdot 10^{-11}$ [N/m$^2$] | | 0.85 | 0.80 | 0.73 |
| $(d_{31} \cdot Y_{11}^E)$ [C/m$^2$]$^2$ | | 65 | 109 | 59 |

$\tan\delta$ dielectric loss angle tangent;
$Q_m$ mechanical quality factor;
$Q_m^{\sigma}$ mechanical quality factor (in this work $\sigma = 12\,\text{MPa}$);
$\sigma$ mechanical stress;
$\sigma_{\text{dyn}}$ dynamic strength;
$Y_{11}^E$ Young's modulus ($E = 0$);
$E$ electric field intensity;
$T_c$ Curie-temperature (Curie point);
$k_{31}^2 Q_m^{\sigma}$ piezoelectric quality factor which determines of the piezotransformer voltage ratio:

$$K_{U_0} = \frac{4k_{31}^2 Q_m^{\sigma}}{\pi^2(1 - k_{31}^2)}\,, \tag{2}$$

and the efficiency of the piezotransformer:

$$\eta_{\text{pt}} = \frac{1}{1 + \dfrac{\pi^2}{2Q_m^{\sigma} \cdot k_{33}^2}}\,; \tag{3}$$

$\dfrac{\varepsilon_{33}^{\sigma}}{\varepsilon_0} k_{31}^2 Q_m^{\sigma}$ product which determines the unit power of the piezotransformer:

$$N = \frac{2b}{\pi a} U^2 v_s \cdot \frac{\varepsilon_{33}^{\sigma}}{\varepsilon_0} k_{31}^2 Q_m^{\sigma}\,, \tag{4}$$

where $U$ — supply voltage; $v_s$ — speed of sound in the piezoelectric transducers; $a$, $b$ — thickness and width of the piezoelectric ceramics;

$(d_{31} \cdot Y_{11}^{E})^2$ product which determines of the unit shaft power of the piezoelectric engine:

$$N = \frac{2b}{\pi a} U^2 v_s \cdot Q_m^{\sigma} (d_{31} Y_{11}^{E})^2; \tag{5}$$

| | |
|---|---|
| $\Delta f_r / f_r$ | relative change of the resonance frequency $f_r$; |
| $\gamma$ | pyroelectric coefficient; |
| HF | hard ferroelectrics; |
| MHF | moderately hard ferroelectrics; |
| SF | soft ferroelectrics. |

### *2.2. The PZT-type ceramics with chemical constitutions corresponding to the R- or T-boundary of the morphotropic region*

As been mentioned, there are only few data on the influence of the lead vacancies on the structure of the solid solutions prepared on the basis of PZT. PZT-type solid solutions with chemical constitutions within the morphotropic region (MR) was most often chosen as objects for the investigation. It is known (e.g. [2, 6]) that solid solutions with chemical constitutions which correspond to the diphase system: (rhombohedral phase (RP) + tetragonal phase (TP)) are characterized by a high sensitivity to external effects and internal changes. Therefore, one could expected considerable changes of the structure with changing stoichiometry.

Investigations of the influence of $V^{\mathrm{Pb}}$ vacancies on the structure of PZT-type solid solutions have been performed either on the PCR-1 ceramics [10], the chemical constitution of which corresponded to the rhombohedral boundary of the morphotropic region (R-boundary of MR) or on the PCR-8 ceramics [11, 12] the chemical constitution of which corresponded to the tetragonal boundary of the morphotropic region (T-boundary of MR). The samples for the investigations have been prepared first by the classical ceramic technology and then they were roasted under oxygen (to avoid the creation of oxygen vacancies $V^0$). X-ray investigations were performed by the X-ray diffractometer DRON-3M (CuK$_\alpha$). To separate the partially overlapped X-ray reflections, the method of approximation of the diffraction maxima was applied [13, 14]. Results of the investigations are shown in Figs. 4, 5 and 6.

It results from the analysis of Fig. 4 that a thermal treatment of the PCR-1 samples at temperatures $T < 1123$ K does not involve any considerable change of the X-ray reflection profiles registered at room temperature. After treatment at $T_s = 1123$ K, beside the 200 reflection of the R-phase, there appear in the X-ray patterns weak reflections typical of the tetragonal cell of the perovskite-type structure. After roasting at that temperature the weak reflections relevant to $ZrO_2$ and PbO also appear.

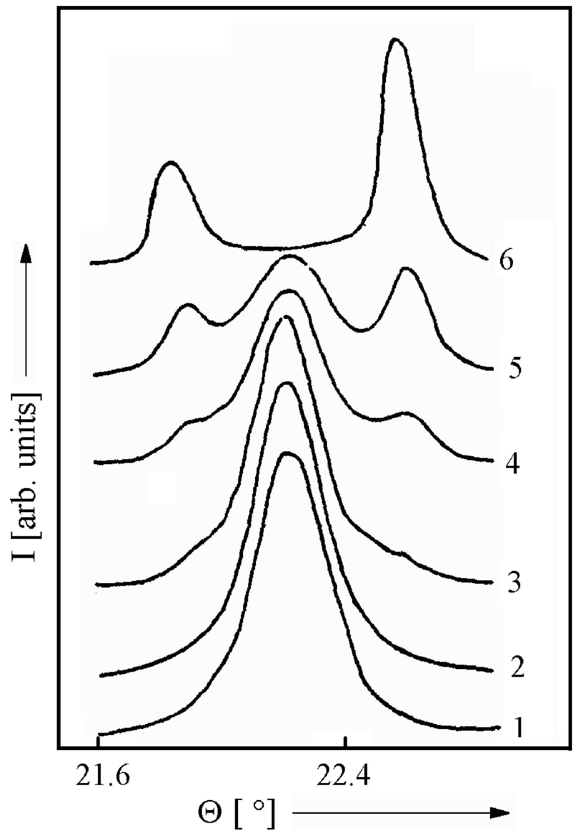


Fig. 4. Profiles of the X-ray reflections of the 200-type obtained at room temperature for the PCR-1 ceramics after roasting at different temperatures: 1 — 873 K; 2 — 1073 K; 3 — 1123 K; 4 — 1173 K; 5 — 1223 K; 6 — 1273 K.

With increasing temperature of the thermal treatment the intensity of reflections typical of the T-phase increases, whereas the R-phase reflections are gradually broadened and weakened. After roasting at $T_s = 1273$ K one can observe strong reflections which are typical of the T-phase and weak reflections due to $ZrO_2$ and PbO. The presence of those free oxides in the samples makes one suppose that the main reason of observed reconstruction of the crystalline structure in the ferroelectric phases of the PZT-type ceramics is a partial decay of the solid solution caused by the thermal treatment.

As a result of the decay of the solid solution, the T-phase is characterized by smaller, volume of the elementary cell in comparison with the R-phase and a greater spontaneous deformation $\delta_{\mathrm{T}}$ in comparison with $\delta_{\mathrm{R}}$ (where: $\delta_{\mathrm{T}} = \dfrac{2}{3}\left(\dfrac{c_{\mathrm{T}}}{c_a} - 1\right)$; $\delta_{\mathrm{R}} \approx \cos\alpha_{\mathrm{R}}$, [15]). The transition of the R-phase into the T-phase is accompanied by a decrease of the $a_{\mathrm{R}}$ parameter (R-phase) and increase of the spontaneous deformation $\delta_{\mathrm{T}}$ (see Fig. 5).

Similar results were obtained from the investigations of the influence of a high temperature thermal treatment on the structural characteristics of PCR-8 ceramic ferroelectrics

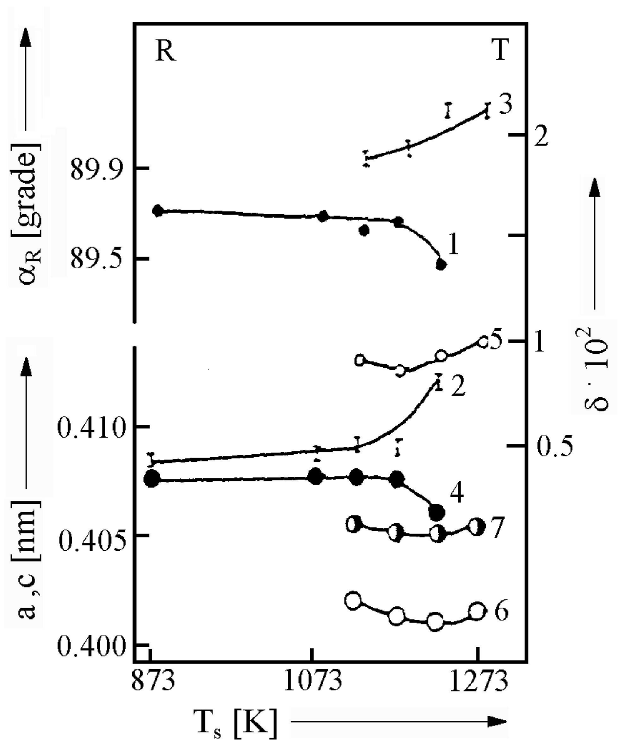


Fig. 5. Dependence of the elementary cell parameters of the rhombohedral (R) and tetragonal (T) phases determined for the PCR-1 ceramics after roasting at different temperatures (873 – 1273 K): 1 — $\alpha_R$; 2 — $\delta_R$; 3 — $\delta_T$; 4 — $a_R$; 5 — $c_T$; 6 — $a_T$; 7 — $\bar{a}_T = \sqrt{a_T^2 c_T}$ .

(Fig. 6). With a roasting temperature increasing from $T_s = 1123$ K one can observe additional diffraction reflections on the X-ray patterns recorded at room temperature. Some of those reflections came from the oxides: $ZrO_2$ and PbO. Moreover, a change of the diffraction profiles of the perovskite-type multiplets took place. The character of that change proves that the second T-phase appears and that the concentration of the new phase increases as well as the primary T-phase. That additional T-phase is characterized by a smaller $a_T$ parameter, a smaller volume of the elementary cell ($a_T^2 c_T$) and a greater spontaneous deformation ($\delta_T$) in comparison to the primary T-phase.

The most probable reason of the observed changes of the crystalline structure of the piezoceramics during the thermal treatment is the evaporation of lead from some crystallites. The results of the structure investigations, carried out on PCR-8 samples obtained by a synthesis of the parent substance with a 15% deficiency in lead, seem to prove that. In the case of stoichiometric samples, which were roasted as well as in the case mentioned above a decrease in $a_T$ parameter and increase in $\delta_T$ at the room temperature have been ascertained.

The appearance of the reflections connected with $ZrO_2$ and PbO on the X-ray pattern and the lack of reflections related to $TiO_2$ show that the disturbance of stoichiometry

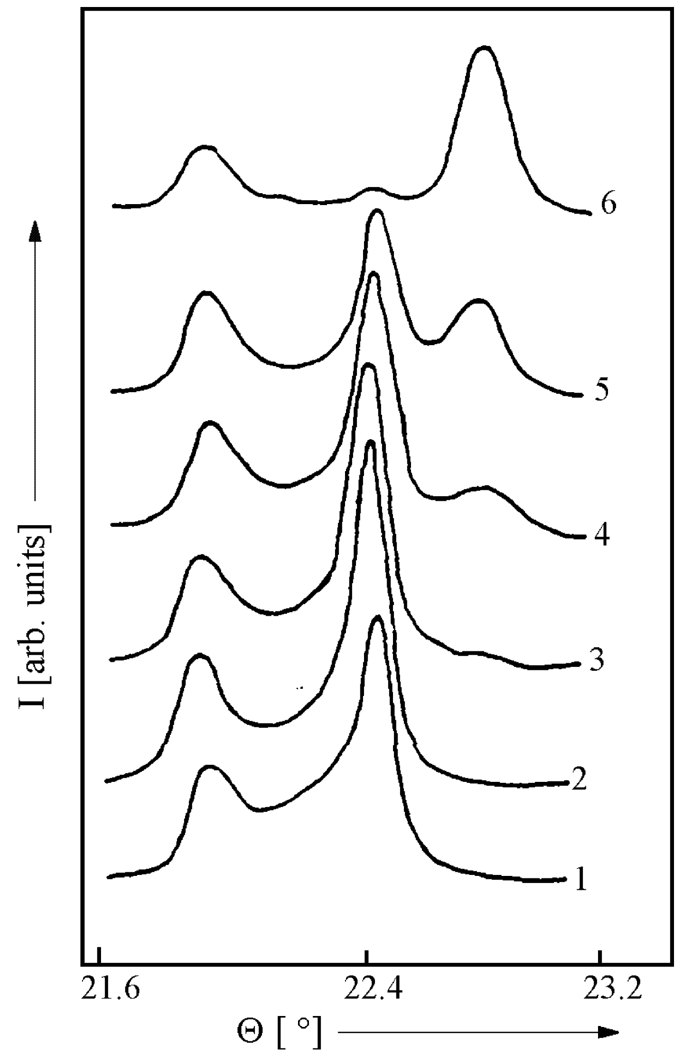


Fig. 6. Profiles of the X-ray reflections of the 200-type obtained at room temperature for the PCR-8 ceramics after roasting at different temperatures: 1 — 873 K; 2 — 1073 K; 3 — 1123 K; 4 — 1173 K; 5 — 1223 K; 6 — 1323 K.

by Pb evaporation takes place first of all as the result of breaking the Zr – Pb bonds in the crystalline lattice. Therefore, the concentration of Ti increases in the sublattice B of the $ABO_3$ perovskite structure (where: A – Pb; B – Zr,Ti) of the crystallites with Pb vacancies. This leads to a gradual decay of the solid solution into the new perovskite phase and the oxides $ZrO_2$, PbO. At a temperature $T < T_c$, the new perovskite phase is characterized by smaller $a_{\mathrm{T}}$ and greater $\delta_{\mathrm{T}}$ values in comparison with the primary T-phase because its chemical constitution becomes closer to $PbTiO_3$ for which $a_{\mathrm{T}} = 0.3904$ nm, $c_{\mathrm{T}} = 0.4150$ nm and $\delta_{\mathrm{T}} = 0.0420$ [16].

*2.3. PZT-type piezoceramics with chemical constitution of the T-phase region*

The solid solution of $PbTiO_3 - PbZrO_3 - Pb(W_{1/2}Cd_{1/2})O_3$ with a little amount of the third component was chosen to find how the lead deficiency influences the PZT-type piezoceramic materials with the constitutions from the T-phase region. The samples $Pb_{1-x}(Zr_{0.39}Ti_{0.59}W_{0.01}Cd_{0.01})O_3$ have been synthesized with $x$ varying stepwise by 0.025 in the from 0 to 0.1 and next by 0.1 from 0.1 to 0.5. The synthesis took place by a solid state reaction in the mixture of lead oxide, titanium oxide, zirconium oxide, cadmium oxide and tungsten oxide (all the oxides were analytically pure). Cadmium and tungsten oxides were introduced into the $PbTiO_3 - PbZrO_3$ system to accelerate the synthesis during the sintering process.

The ceramic material was obtained by the classical technology [3, 4]. The mixture of the oxides was obtained in the water medium by a vibration mixer. The disk compacts of 20 mm in diameter and 1 mm thickness (pressing pressure 5 MPa) were prepared from that mixture.

To determine each stage of the phase formation, the compacts were sintered four times in the temperature range 1173 – 1473 K. Each time the temperature was increased by 100 K. After the particular sintering, the samples were powdered and the compacts made again. The time of sintering was 10 hours (excluding the time of heating and cooling).

The investigations of the crystalline structure have been performed by the X-ray diffraction method (DRON-3; $CuK_\alpha$, $\beta$-filtr).

There are fragments of the X-ray patterns of the samples characterized by $x = 0$, $x = 0.075$ and $x = 0.400$ in Figs. 7 – 9, respectively.

From analysis of those X-ray patterns it result that after roasting at 1173 K the perovskite-type structure was formed in all the cases. The reflections 001, 100, 011, 110 etc. confirm it. The reflections from $ZrO_2$ were also registered in the case of $x = 0$ (Fig. 7).

In the case of low $x$ values ($x < 0.2$) the perovskite type structure was not a "monotetragonal" one. This is indicated by the profiles of the 011 and 110 reflections and their location in relation to $2\theta$ seen in Figs. 7 and 8, when the roasting temperature increases both the profiles of the above mentioned reflections and their location versus $2\theta$ changed.

For samples which are characterized by large $x$ values ($x > 0.3$), the "monotetragonal" structure appears just after the first sintering at $T_s = 1173$ K and the elementary cell parameters are: $a_T = 0.3920$ nm and $c_T = 0.4145$ nm. These parameters are close to those of pure $PbTiO_3$ ($a_T = 0.3904$ nm; $c_T = 0.4150$ nm [16]). The similarity of the structure of pure $PbTiO_3$ to that of the PZT-type piezoceramic having $x = 0.4$, is shown most clearly by a comparison of the suitable X-ray patterns (see Figs. 9 and 10). One can see that not only the locations of the suitable reflections are close to each other but also the ratios of their total intersites are nearly the same.

When the roasting temperature increases, the degree of the structural perfection of the obtained piezoceramics increases (see Figs. 7, 8 and 9).

The parameters of the perovskite-type structure tetragonal cells of piezoceramics with different $x$, determined after sintering at 1473 K for 10 hours, are shown in Table 3. It results from the analysis of the data given in that table and after a comparison

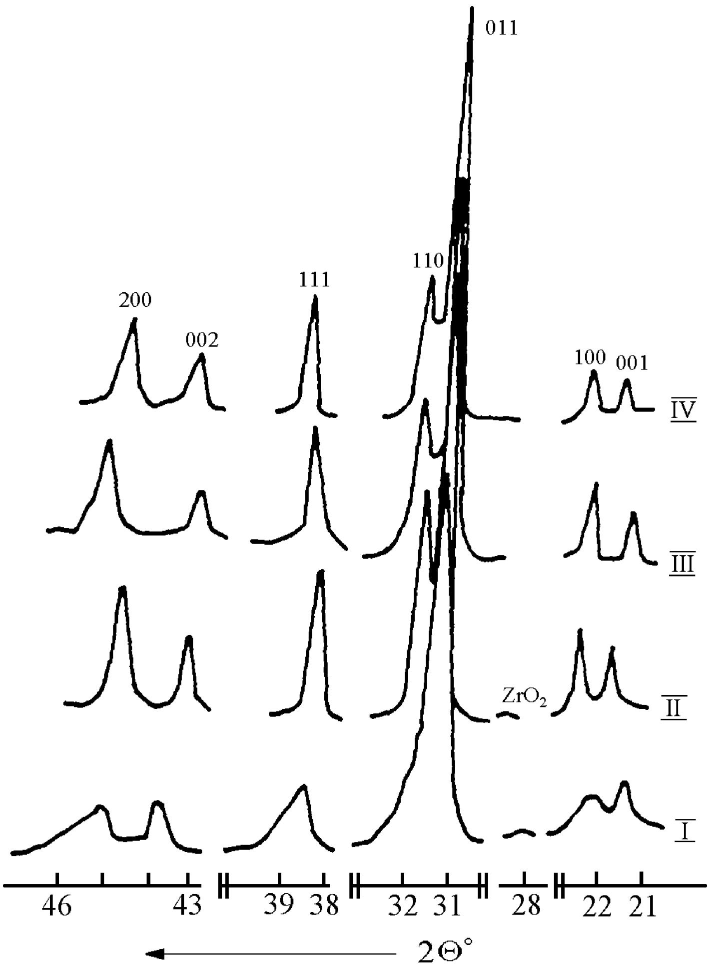


Fig. 7. Fragments of the X-ray patterns obtained at room temperature for the $Pb_{1-x}(Zr_{0.39}Ti_{0.59}W_{0.01}Cd_{0.01})O_3$ piezoceramics in the case of $x = 0$ after sintering at the following temperatures: I — 1173 K; II — 1273 K; III — 1373 K; IV — 1473 K (sintering time $t_s = 10$ h).

with the $PbTiO_3$ elementary cell parameters ($a_T = 0.3904$ nm; $c_T = 0.4150$ nm) and with those of the $PbZrO_3$ elementary cell ($a_T = 0.4159$ nm; $c_T = 0.4109$ nm; pseudotetragonal system) and with the $PbTiO_3$ – $PbZrO_3$ solid solution elementary cell parameters [1], that when the lead deficiency increases, the perovskite-type phase of $Pb_{1-x}(Zr_{0.39}Ti_{0.59}W_{0.01}Cd_{0.01})O_3$ becomes similar to $PbTiO_3$ as regards the chemical constitution and the parameters of the elementary cell. That result is consistent with the kinetic data of the synthesis in the $PbO - TiO_2 - ZrO_2$ system. According to ref. [1], the synthesis at low temperatures ($T_s < 973$ K) begins from the creation of $PbTiO_3$. The latter reacts with $ZrO_2$ only at higher temperatures ($T_s > 973$ K) and forms Pb(Zr,Ti)$O_3$ with the oxides PbO and $TiO_2$ remaining free.

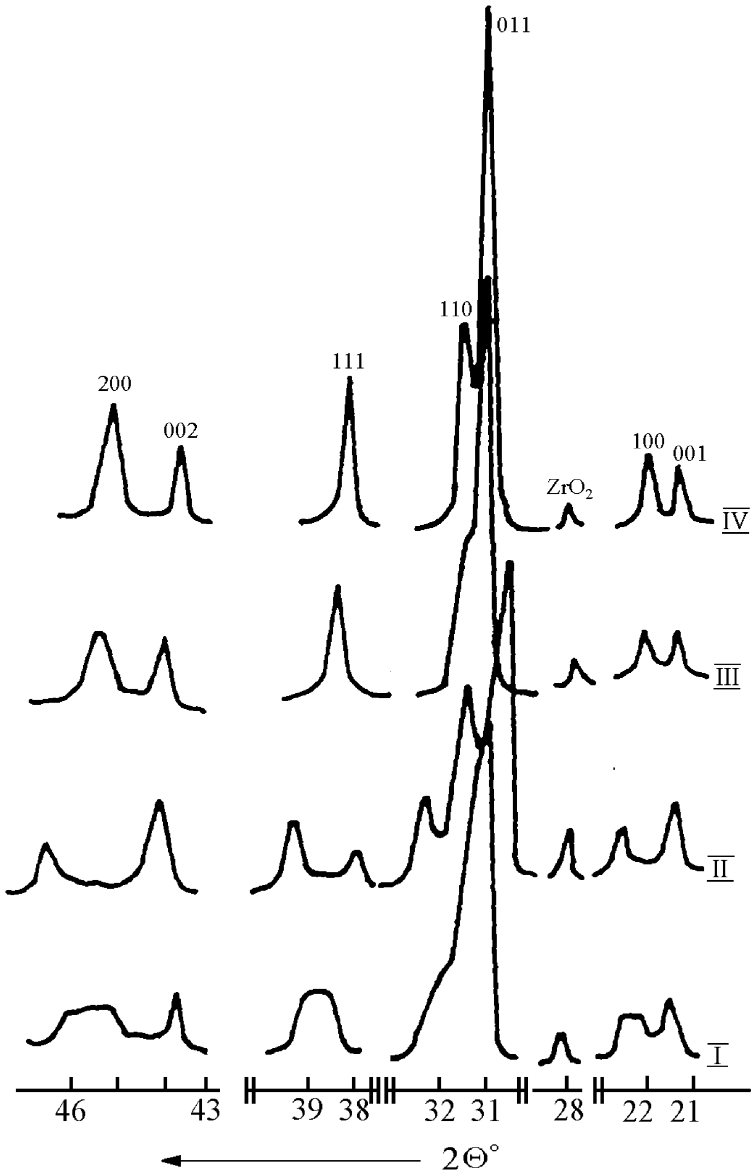


Fig. 8. Fragments of the X-ray patterns obtained at room temperature for the $Pb_{1-x}(Zr_{0.39}Ti_{0.59}W_{0.01}Cd_{0.01})O_3$ piezoceramics in the case of $x = 0.075$ after sintering at the following temperatures: I — 1173 K; II — 1273 K; III — 1373 K; IV — 1473 K (sintering time $t_s = 10$ h).

The chemical constitution of the perovskite-type phase is shown in the column 5 of Table 3. The constitution has been calculated with the assumption that the valency balance can be satisfied even if there is no excess of $ZrO_2$ in the reaction.

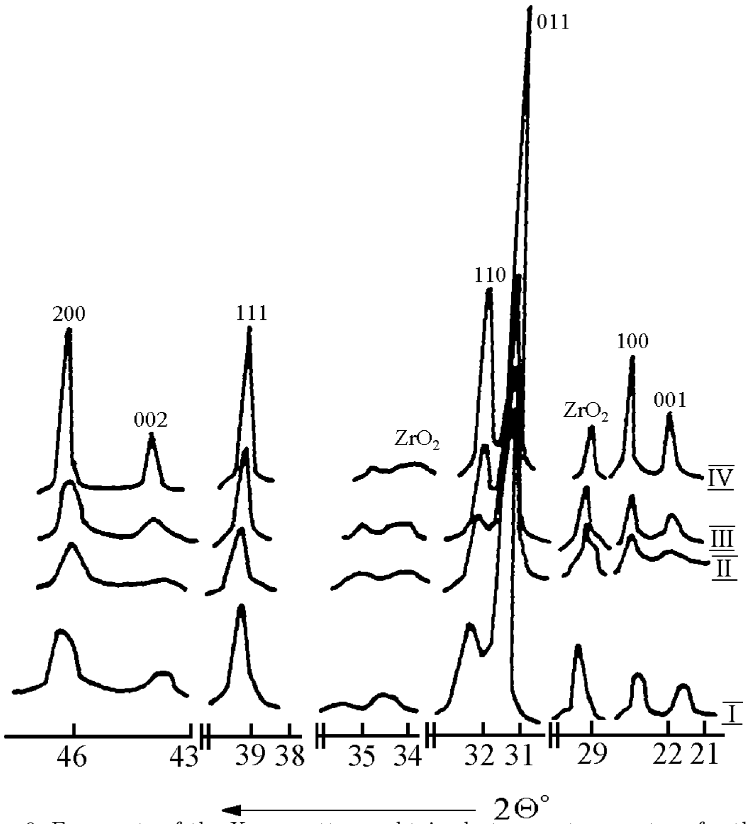


Fig. 9. Fragments of the X-ray patterns obtained at room temperature for the $Pb_{1-x}(Zr_{0.39}Ti_{0.59}W_{0.01}Cd_{0.01})O_3$ piezoceramics in the case of $x = 0.4$ after sintering at the following temperatures: I — 1173 K; II — 1273 K; III — 1373 K; IV — 1473 K (sintering time $t_s = 10$ h).

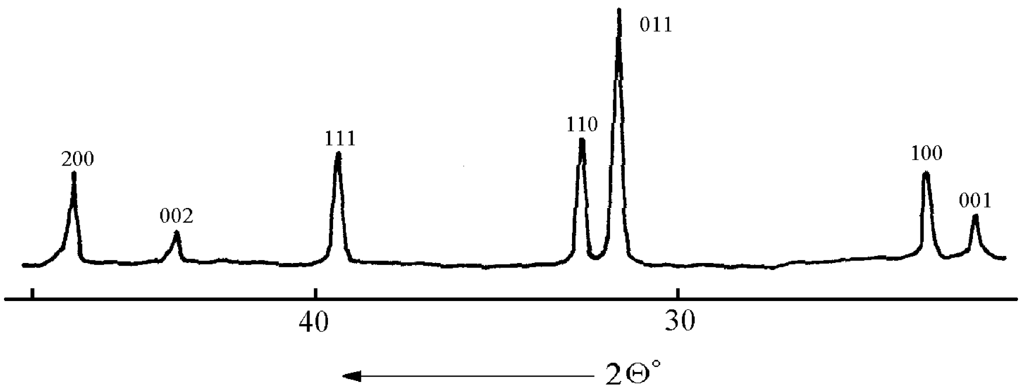


Fig. 10. X-ray pattern of the $PbTiO_3$ powder obtained under the same conditions as the X-ray patterns presented in Figs. 7, 8, and 9.

**Table 3.** Parameters of the elementary cells of the PZT-type solid solution of the chemical constitution $Pb_{1-x}(Zr_{0.39}Ti_{0.59}W_{0.01}Cd_{0.01})O_3$.

| No | $x$ | $a_T$ [nm] | $c_T$ [nm] | Chemical constitution taking into account deficiency in lead |
|---|---|---|---|---|
| 1 | 2 | 3 | 4 | 5 |
| 1 | 0.000 | 0.3978 | 0.4131 | $Pb(Zr_{0.39}Ti_{0.59}W_{0.01}Cd_{0.01})O_3$ |
| 2 | 0.025 | 0.3989 | 0.4143 | $Pb(Zr_{0.3744}Ti_{0.6050}W_{0.0103}Cd_{0.0103})O_3$ |
| 3 | 0.050 | 0.3985 | 0.4139 | $Pb(Zr_{0.3579}Ti_{0.6211}W_{0.0105}Cd_{0.0105})O_3$ |
| 4 | 0.075 | 0.3992 | 0.4149 | $Pb(Zr_{0.3406}Ti_{0.6378}W_{0.0108}Cd_{0.0108})O_3$ |
| 5 | 0.100 | 0.3965 | 0.4132 | $Pb(Zr_{0.3222}Ti_{0.6556}W_{0.0111}Cd_{0.0111})O_3$ |
| 6 | 0.200 | 0.3955 | 0.4141 | $Pb(Zr_{0.2375}Ti_{0.7375}W_{0.0125}Cd_{0.0125})O_3$ |
| 7 | 0.300 | 0.3951 | 0.4131 | $Pb(Zr_{0.1285}Ti_{0.8429}W_{0.0143}Cd_{0.0143})O_3$ |
| 8 | 0.400 | 0.3920 | 0.4145 | $Pb(Ti_{0.9666}W_{0.0167}Cd_{0.0167})O_3$ |
| 9 | 0.500 | 0.3921 | 0.4146 | $Pb(Ti_{0.9600}W_{0.0200}Cd_{0.0200})O_3$ |

## 3. Conclusions

1. Creation of the lead vacancies ($V^{Pb}$) in the solid solutions prepared on the basis of $Pb(Zr,Ti)O_3$ causes the following changes in the physical properties:

- increase in the permittivity ($\varepsilon$);
- large dielectric loss ($\tan\delta$);
- increase of the elastic compliance ($S_{ijkl}$);
- decrease in mechanical quality factor ($Q_m$);
- increase of the electromechanical coupling coefficient ($k_p$);
- decrease of the coercive field ($E_c$);
- increase of the squareness ratio of the dielectric hysteresis loop;
- strong increase of the specific resistance ($\rho_v$);
- typical weak aging process;
- non-elastic mechanical deformation compliance (deformability);
- yellow colour;
- translucency of the sample;
- darkening of the sample under the influence of light.

2. The obtaining of PZT-type piezoceramics under the conditions, which are conducive to the creation of the lead vacancies leads to the formation of structures that differ from the stoichiometric solid solution structure. The sort of those structural changes depends on the chemical constitution of the PZT-type ceramics, strictly speaking on the place the compound occupies on the solid solution phase diagram and on the concentration of the lead vacancies. Namely:

a) if the chemical constitution of the material corresponds to the rhombohedral boundary of the morphotropic region so, as the roasting temperature increases (as the deficiency in lead increases), the strong diffraction maxima corresponding to the R-phase gradually decay but the T-phase diffraction maxima increase in the X-ray patterns. Diffraction maxima corresponding to $ZrO_2$ and PbO appear and become distinct. Therefore the partial decay of the solid solution takes place as the result of the disturbance stoichiometry caused by the thermal treatment. It causes the reconstruction of the perovskite-type crystalline structure from the (R+T)-phase to the T-phase;

b) if the chemical constitution of the material corresponds to the tetragonal boundary of the morphotropic region therefore, the weak diffraction maxima corresponding to the R-phase and strong maxima corresponding to the primary T-phase gradually decay, as the roasting temperature increases (i.e. as the deficiency in lead increases), whereas new T-phase maxima appear and become more distinct in the X-ray patterns. The new T-phase of the perovskite structure is characterized by a smaller $a_T$ parameter and a larger deformation $\delta_T$ in comparison with those of the primary T-phase. The reflections corresponding to $ZrO_2$ and PbO also appear. Thus, in that case the partial decay of the solid solution into the perovskite-type structure phase and of the free $ZrO_2$ and PbO takes place as a result of the disturbance of the stoichiometry caused by the thermal treatment. The primary phase of the perovskite structure (R+T (I)) converts into the new T (II)-phase;

c) if the chemical constitution of the material corresponds to the tetragonal phase, the roasting temperature of the samples with a small deficiency in lead increases the new T-phase appearing beside the primary tetragonal phase. The new T-phase is characterized by a smaller $a_T$ parameter and greater $\delta_T$ deformation. In case of a large deficiency in lead, only the new perovskite-type T-phase appears after roasting at 1173 K as well as free PbO and $ZrO_2$. The chemical constitution and the elementary cell parameters of the perovskite-type T (II)-phase become closer to $PbTiO_3$.

3. The possibility of a disturbance in the stoichiometry resulting from the creation of lead vacancies is a serious problem of the PZT-type piezoceramic materials technology. The loss in lead takes place both during the synthesis and during the thermal treatment of this material. The knowledge of the crystalline structure changes caused by the increasing in lead deficiency makes it possible to develop methods of checking the loss of Pb atoms from the A sublattice of the perovskite-type structure ($ABO_3$).

4. The creation of lead vacancies in the PZT-type piezoceramic materials by introducing soft doping ions into the A sublattice makes it possible to obtain a soft ferroelectric material which is likely to be widely applied in engineering. However, the deficiency in lead in the PZT caused by the thermal treatment leads to a partial decay of the solid solution and a stepwise conversion of $Pb(Zr,Ti)O_3$ into $PbTiO_3 + ZrO_2 + PbO$. In that case the deficiency in lead is unfavorable from the point of view of the application possibilities of the obtained materials.

## References

[1] B. Jaffe, W.R. Cook and H. Jaffe, *Piezoelectric ceramics*, Academic Press, London 1971.

[2] J. Kwapuliński, Z. Surowiak, M.F. Kupriyanov and S.M. Zaycev, *Investigation of the poling processes in ferroelectric ceramics* [in Russian], Zhurnal Tekhn. Fiziki, **5**, 1049–1052 (1979).

[3] Z. Surowiak, J. Dudek and M. Łoposzko, *The influence of the pressing of the powder on the structure and physical properties of the PZT-type ceramics* [in Polish], Inżynieria Materiałowa (Poland), **6**, 123–129 (1992).

[4] E.G. Fesenko *et al.*, *Highly effective piezoelectric materials for various fields of application*, Ferroelectrics, **167**, 197–204 (1995).

[5] J. Dudek, Z. Surowiak and M. Łoposzko, *The influence of hot-pressing conditions on the properties of* $YBa_2Cu_3O_{7-\delta}$ *ceramics* [in Polish], Akustyka Molekularna i Kwantowa (Poland), **15**, 59–68 (1994).

[6] G.M. Konstantinov, A.G. Gorbunov, M.F. Kupriyanov and S.B. Rastoropov, *Piezoelectric materials* [in Russian], A.E. Panich [Ed.] RGU, Rostov-on-Don 1992, p. 19.

[7] Y. Xu, *Ferroelectric materials and their applications*, North-Holland, New York 1991.

[8] Z. Surowiak, D. Krawczyk and E.G. Fesenko, *The perovskite-type ceramic ferro-electrics characterized by semiconductive and metallic electric conduction* [in Polish], Kwartalnik Elektr. i Telek. (Poland), **40**, 2, 223–247 (1994).

[9] J. Dudek, Z. Surowiak *et al.*, *Physical properties and structure of lead deficient PZT-type piezoceramics*, Polish J. Appl. Chem., **41**, 4, 295–316 (1997).

[10] Z. Surowiak, J. Dudek, E.G. Fesenko and A.E. Panich, *Technology of multicomponent ceramic materials on the basis of PZT* [in Polish], Ceramics (Poland), **45**, 145–155 (1994).

[11] A.E. Panich and M.F. Kupriyanov, *Physics and technology of ferroelectric ceramics* [in Russian], RGU, Rostov-on-Don, Russia 1989, p. 180.

[12] E.G. Fesenko, A.Ya. Danciger and O.N. Razumovskaya, *New piezoceramic materials* [in Russian], RGU, Rostov-on-Don 1983.

[13] Z. Surowiak, A.E. Panich and V.P. Dudkevich, *Thin ferroelectric films* [in Russian], RPI, Rostov-on-Don 1994, p. 58.

[14] M.F. Kupriyanov, G.M. Konstantinov and A.E. Panich, *Morphotropic phase transitions in ferroelectrics* [in Russian], RGU, Rostov-on-Don 1992.

[15] Z. Surowiak and V.P. Dudkevich, *Thin ferroelectric films* [in Polish], University of Silesia, Katowice (Poland), 1996, p. 159.

[16] E.G. Fesenko, V.G. Gavrilachenko, Z. Surowiak and P. Wawrzała, *Domain structure and switching processes in thin plate-like* $PbTiO_3$ *monocrystals* [in Polish], Archiwum Nauki o Materiałach (Poland), **17**, 1, 43–71 (1996).

ARCHIVES OF ACOUSTICS
**25**, 2, 271–272 (2000)

**C H R O N I C L E**

## 108th AES Convention, Paris
## 19 – 22 February, 2000

Polish participation in the AES Conventions has already become a well founded tradition. So it was this year also, at an exceptional place and date — Paris 2000. The 108th Convention was the first in the French capital for five years. It was held at the newly refurbished Palais des Congrès (see photo of a group of Polish participants before the Palais front), which played host to over three hundred exhibitors' booths from all over the world; among them all leading enterprises in the field of sound and vision techniques.

Opening ceremonies held on Saturday, noon, February 17, were devoted in particular to stressing the role of AES Conventions on the brink of a new century. "For over 50 years the AES and its Conventions have been the link within the international audio community: a forum for exchange of new ideas. At the dawn of the new millenium and the age of globalization, the role of the AES is more important than ever before" — said the Convention Chairman, Daniel Zalay rightly in his Welcoming Address.

The most interesting for the Polish representatives was the second part of the ceremonies devoted to the announcement of Awards to distinguished members of the Society. First of all, the significant accomplishments were honoured by AES citation awards, namely: Irina Aldoshina — for her significant contribution to the Russian AES Sections, Vytautas Stauskis — for his contribution to architectural acoustics and foundation of the Lithuanian AES Section, Marina Bosi and Karlheinz Brandenburg — for cochairmanship of the 17th AES International Conference. Next, the highest AES award announced in Paris, the Fellowship, was presented to Andrzej Czy§ewski — for his pioneering achievements in applications of computing (see the enclosed copy).

Polish attendees warmly applauded Prof. Czyżewski, as he received the Fellowship testimony on the auditorium stage, being duly proud of his outstanding achievement.

Although no Polish enterprise participated in the huge exhibition, a number of Polish authors contributed to scientific sessions, running parallel to the exhibition and to other Convention events. Among 100 papers read during 19 thematical sessions, 5 were presented by Polish authors and coauthors, coming mainly from the Technical Universities of Gdańsk and Wrocław (see Appendix). It may be added here that Prof. George Papanikolaou from the Aristotle University of Thessaloniki, Greece, the member of the

Polish Acoustical Society, cooperating for many years with the Sound Engineering Department of Gdańsk Technical University, presented 3 papers in Paris, together with a group of his coauthors.

A characteristic feature of the Paris Convention was the growing participation of students, organized within the AES Student Sections all over the world. Several special events were organized in Paris for students, such as Student Delegate Assembly, Student Section Report, Education Fair, Poster Session, Job Forum, Recording Awards etc. Polish AES Student Section was represented by 44 participants. They organized their own information desk (see photograph), disseminating information concerning studies on sound engineering in Poland.

The most valuable, hovever, for the Polish students was their participation in the Convention workshops. During the 15 workshop sessions leading scientists and professionals demonstrated practical solutions of selected problems, connected with the techniques of sound and vision. This was a true laboratory for students, familiarizing them with the most modern equipment and systems recently developed by world-renowned producers.

The 108th Convention was as successful as the previous one in Munich as regards to the general number of attendees, number of exhibitors and visitors in particular. Let us hope that the next two Conventions scheduled to be held in Amsterdam in 2001, and Munich in 2002, will also be successful, and that the Polish participation and contribution remains, at least, on the level characterized in brief in this report.

*Marianna Sankiewicz*

**Appendix**

Papers presented by Polish authors during the 108th AES Convention in Paris

1. Grzegorz Szwoch, Bożena Kostek, Andrzej Czyżewski, TU Gdańsk, *Simulating Acoustics of Hearing Aids Employing Nonlinear Signal Filtering and Waveguide Modelling* — Session C4, Preprint 5087.
2. Andrzej Czyżewski, Bożena Kostek, Piotr Suchomski, TU Gdańsk, *Expert System for Hearing Aids Fitting* — Session D5, Preprint 5094.
3. Andrzej Dobrucki, Grzegorz Matusiak, TU Wrocław, *Symmetrical Loudspeaker Band-Pass Systems of Eighth Order with Passive Filter* — Session G2, Preprint 5107.
4. Piotr Pruchnicki, TU Wrocław, *The Influence of Measuring Accuracy on the NARMAX Model of Dynamic Loudspeaker* — Session G6, Preprint 5111.
5. Bożena Kostek, Andrzej Czyżewski, TU Gdańsk, *Automatic Classification of Musical Sounds* — Session H2, Preprint 5115.


Fig. 1. Fellowship Award certificate presented in Paris to Prof. Andrzej Czyżewski.

Fig. 1. Modernized front of the Palais des Congrès; a group of Polish participants before entrance.


Fig. 2. Polish Student Section information desk — (l. to r.) K. Kąkol, J. Czerniawski — Board members, and P. Odya — Chairman of the Section.